The application of time-domain spectroscopy to the study of optical activity in metamaterials

Zangui, Soumya

Award date:
2013

Awarding institution:
University of Bath

THE APPLICATION OF TIME-DOMAIN SPECTROSCOPY TO THE STUDY OF OPTICAL ACTIVITY IN METAMATERIALS

Soumya Zangui

A thesis submitted for the degree of Doctor of Philosophy

University of Bath

Department of Physics

March 2015

Acknowledgements

First, I would like to offer my sincerest gratitude to my supervisor Dr. Steve Andrews for giving me the opportunity to work in this research project and for providing me support and guidance throughout the completion of this work. Thanks for his patience, knowledge and his assistance in my lab work and my writing up.

Many thanks goes out to Mr. Paul Reddish and Mr. Peter Sykes for their help in the workshop and for the sample holder construction. Dr. Sivapathasundaram Sivaraya for his technical assistance and advices in the clean room and Dr. Alistair Muir for his useful guidance in the use of CST Microwave Studio.

Away from physics and work, I would like to thank my parents for their support through my entire life and a very special thanks to my friend Dr. Laurent Patier for his encouragement and advices.

Finally, I would like to dedicate this thesis to my sisters Sanâa, Ghita and Kenza, and my grandad Thami. Without your love and support I would not be here and this would not have been possible.

Abstract

The terahertz time-domain spectroscopy (TDS) technique which combines broadband and highly sensitive coherent detection with time revolution and strong immunity to background has found application in a wide range of fundamental disciplines. This work presents the development of a polarisation resolved THz-TDS spectrometer that enables sensitive studies of the optical activity of chiral metamaterials in the terahertz frequency range.

The thesis is divided into two principal parts. The first (chapters 2 to 4) describes the principles of the time-domain spectroscopy. This is followed by descriptions of a crossed-bowtie antenna which simultaneously detects both orthogonal field components and devices for measuring the state of polarisation of THz waves. In particular we present experimental and computational studies of four linear polarisers. One is a pile-of-plates which relies on the different reflectivity of *s* and *p*-polarised light incident on a dielectric surface at Brewster's angle and the others are wire-grids of different dimensions and different substrates which rely on the anisotropic conductivity of thin metal wires. The design of the polarisation resolved spectrometer and a formalism for describing optical activity and analysis data are then described in the fourth chapter.

The second part of the thesis describes applications of the polarisation sensitive terahertz TDS system to the study of optical activity exhibited by artificial materials. Four structures have been studied in this work; metal screw hole arrays, quasi-two-dimensional gammadions and Archimedean spiral metamaterials and a quasi-three-dimensional array of spirals. Experimental and computational studies of the polarisation characteristics and the optical properties of these structures are discussed in chapters 5, 6 and 7.

Contents

List of Abbreviations

THz	Terahertz
QCL	Quantum cascade laser
FS-EOS	Free space electro-optic sampling
SNR	Signal-to-noise ratio
UV	Ultraviolet
TDS	Time-domain spectroscopy
FTS	Fourier transform spectroscopy
CD	Circular dichroism
LCP	Left-hand circularly polarised light
RCP	Right-hand circularly polarised light
XRD	X-ray diffraction
NMR	Nuclear magnetic resonance
ECD	Electronic circular dichroism
VCD	Vibrational circular dichroism
CW	Continuous-wave
PC	Photoconductive
LT-GaAs	Low temperature gallium arsenide
ORD	Optical rotatory dispersion
EOT	Extraordinary optical transmission
SSPs	Surface plasmon polaritons
FDTD	Finite-difference time-domain

Chapter 1

INTRODUCTION

1.1 Terahertz Radiation

Terahertz (THz) radiation spans a frequency range that is rich in science and technological potential. It occupies the portion of the electromagnetic spectrum between the mid-infrared and the microwave bands, which corresponds to the frequency range 0.1 THz to 10 THz and a wavelength of 3 mm to 30 μm as illustrated in figure 1.1. This spectral range is often referred to as called terahertz region or the terahertz gap because the terahertz region was until recently largely inaccessible due to a lack of high performance sources, detectors and optical components.

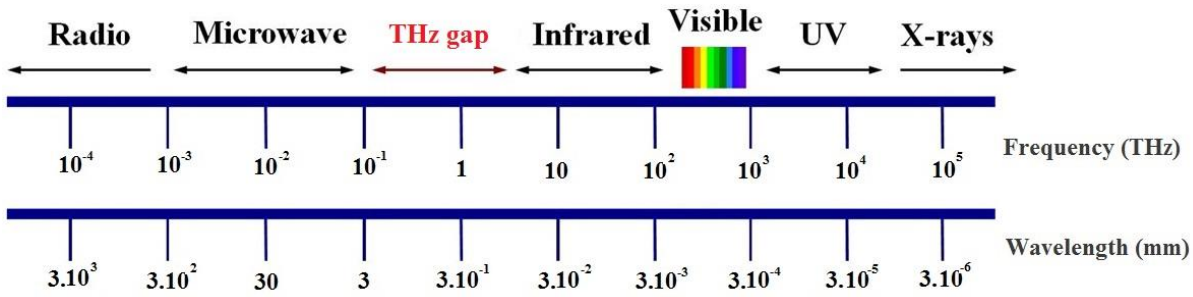

Fig 1.1: Schematic diagram showing the THz region of the electromagnetic spectrum

The terahertz region has been an exciting field of interest for scientists in the last two decades because of the sensitivity of electromagnetic radiation in this region to different phenomena such as energy gaps in nanostructures, free carrier absorption, rotations in small polar molecules and lattice vibrations [1]. In addition terahertz radiation has long been studied by astronomers to give information about the early universe [2]. Much of the recent interest in terahertz real world applications stems from its ability to penetrate deep into many insulating materials and also, because terahertz radiation is readily absorbed by water, it can be used to distinguish between materials with varying water content—for example, fat versus lean meat. These properties plus the existence of some spectral fingerprints lend themselves to applications in biomedical imaging [3] as well as process and quality control such as the inspection of the homogeneity of pharmaceutical tablet coatings [4] and the identification of polymorphic forms of crystals used in pharmaceuticals [5]. The latter show

different chemical properties, such as solubility, melting point and absorption in the body [6]. Another research area using terahertz radiation is in security screening [7], since most clothes are transparent to terahertz radiation. Furthermore common explosives have distinct spectral fingerprints at terahertz frequencies. Of particular relevance to this thesis, the terahertz spectral region has also strong potential for applications such as the identification of chiral molecules and the study of chiral drug structures, DNA and proteins [8, 9]. Terahertz radiation can also be used to probe fundamental physics, such as the nature of electronic excitations in quantum nanostructures and correlated electron systems.

Compared to the well-developed technologies and applications at microwave and optical frequencies, progress in the terahertz band is very limited. Applications have taken a long time to develop, partly due to the difficulty in improving the technology underpinning the generation and detection of terahertz waves and partly because of the lack of high quality optical components e.g. polarisers, waveplates and cameras. As a result, useful applications have been so far restricted to basic science and material research with only a small number of real world applications (e.g. pharmaceutical quality control) so far developed to the point of actual use.

Two categories of terahertz sources and systems are commercially available, narrowband and broadband. Narrowband terahertz sources, include optically pumped gas lasers and backward wave oscillators which are operated in continuous wave mode (<10 mW in the region below 2 THz with limited tunability). Other sources include solid state devices such as Gunn diodes with Schottky-diode multiplier chains [10] and optical techniques based on photomixing or parametric generation [11]. More recently, narrowband sources have been realized with quantum cascade lasers (QCL) [12] which exploit intersubband transitions in quantum well structures. These devices are limited by their inability to operate much below 2 THz and they must be operated at low temperatures. The narrow tuning range of these sources makes it cumbersome to obtain measurements at several different frequencies. This is especially problematic since many interesting properties can only be ascertained from the behaviour of the conductivity absorption or refractive index over a wide spectral range. The development of the multi-terahertz bandwidth femtosecond laser in the 80s emerged as a solution to some of the above problems and led to a renaissance in far-infrared science, since it enabled the construction of broadband optoelectronic THz sources and detectors [13]. A few years later, purely optical sources based on difference frequencies generation in a nonlinear crystal such as ZnTe (Chen et al., 2001) were developed.

The methods of detection of terahertz pulsed radiation can similarly be divided into two classes. The first class is the so-called incoherent detection and it is most applicable to continuous wave sources. By incoherent we mean that only power is measured. Incoherent detection is achieved using broadband detectors such as helium-cooled bolometers and pyroelectric sensors. Coherent detection of terahertz waves involves measurement of the

amplitude and phase of the electric field rather than the intensity of the radiation. Such detection can be performed in the time domain using photoconducting antenna receivers gated by an ultra-short laser pulse or free space electro-optic sampling (FS-EOS). These techniques provide a good signal-to-noise ratio (SNR) and a large bandwidth which enables many applications such as spectroscopy [9][10] and imaging [12] [13] [14]. In spectroscopic applications, Terahertz time-domain spectroscopy (THz-TDS) using photoconductive sources and detectors, is the most widespread technique since it typically has a high detection bandwidth of 3 THz to 5 THz and an excellent dynamic range up to 100 dB.

1.2 Terahertz Time-Domain Spectroscopy

THz waves have made great progress since the invention of methods of generating and detecting THz radiation using ultrashort laser pulses [15, 16]. Most of the applications can be divided into two categories: terahertz wave spectroscopy and terahertz wave imaging. In spectroscopic applications, the most widely used method has been terahertz time domain spectroscopy (THz-TDS). This technique developed originally in the 1980's in the pioneering work of D.H. Auston and coworkers [15, 17] and has become widely used in materials research since the early 90s, i.e. precise gas sensing [4, 5], semiconductors [18] and superconductors [19, 20], photonic crystals [21, 22], liquids [23] and drugs structure [24]. Before terahertz time domain spectroscopies were invented, the continuous wave Fourier transform spectroscopy (FTS) technique was mainly used in the far-infrared [25]. FTS is a general term that describes the analysis of any signal into its constituent Fourier components and is usually based on a Michelson interferometer. This interferometer consists of two mirrors set at right angles and a beam splitter which divides the input light beam into two beams with approximately the same intensity. The two separated beams of light reflected from the mirrors are then recombined at the beam splitter and detected as a function of the position of one of the mirror which can be moved back and forth. The Michelson interferometer has several differences and similitudes compared to the terahertz time domain spectroscopy technique. In FTS the intensity of the signal uses a broadband source such as a mercury arc lamp and the whole spectrum is observed at each mirror position. FTS offers an extremely wide spectral range, but suffers from low signal-to-noise ratio in the terahertz region because of the low source intensity and a poor time resolution because of the very slow detection response.

Unlike the traditional Fourier-transform spectroscopy where only the power transmittance or the power reflectivity is obtained, terahertz time-domain spectroscopy provides simultaneous amplitude and phase information. The spectral distribution $E(\omega)$ of the THz pulse is obtained from the Fourier transform of $E(t)$

$$E(\omega) = \int_{-\infty}^{+\infty} e^{-i\omega t} E(t) dt = A(\omega) e^{i\Phi(\omega)}, \quad (1)$$

where A and Φ are respectively the spectral amplitude and the phase of the signal which contain informations about the absorption coefficient and the refractive index respectively. Phase is not easily accessible with incoherent spectroscopy and is one of the important advantages of the time-domain technique. Another advantage is the high time resolution which in principle allows dynamical studies using pump-probe techniques.

The frequency range of the spectrometer is fundamentally limited by the response of the THz source and detector and the laser pulse width. The spectral resolution of THz-TDS, $\delta\omega$, is determined by the temporal scanning range T and it is given by

$$\delta\omega = \frac{2\pi}{T}. \quad (2)$$

In a typical experiment, to measure the spectral response of a sample, two traces are recorded, one where the pulse propagates through the sample and a reference pulse. The Fourier transform of these two-terahertz waveforms obtained without the sample can be written as $A_s(\omega)e^{i\Phi s(\omega)}$ and $A_r(\omega)e^{i\Phi r(\omega)}$ respectively. By making the comparison between the signal spectrum and the reference spectrum, it is possible to extract the dielectric function of the sample, usually expressed by the absorption coefficient α and the refractive index n [1] where

$$\alpha = \frac{2}{d} \ln \frac{A_R}{A_S}, \quad (3)$$

and

$$n(\omega) = 1 + \frac{[\Phi_S(\omega) - \Phi_R(\omega)]c}{\omega d}, \quad (4)$$

where d is the thickness of the sample and c the speed of the light in vacuum.

Table 1.1 summarises some of the advantages and the disadvantages of the THz time-domain spectroscopy (TDS) technique compared with other types of spectroscopy.

Advantages	Disadvantages
- Direct electric field measurement of the THz pulses (amplitude & phase) ⇨ absorption and refraction index of the sample. - Very high signal-to-noise ratios - Coherent detection insensitive to background radiations - Large spectral bandwidth of THz radiation - Sub-picosecond terahertz pulse duration ⇨ can study dynamics of optically excited samples in pump-probe experiments	- Lower spectral resolution than narrowband THz spectroscopy - Expensive because of use of ultrafast lasers. - Smaller spectral range than FTS

Table 1.1: Overview of some advantages and disadvantages of the THz time-domain spectroscopy technique compared to other spectroscopy techniques.

1.3 Circular Dichroism Spectroscopy

Circular dichroism (CD) is the difference in the absorption of left-handed circularly polarised light (LCP) and right-handed circularly polarised light (RCP) which occurs in the presence of chiral media [26] whether at the molecular level or on a macroscopic scale. Linearly polarised light can be described as a superposition of left and right hand circularly polarised light of equal amplitude and phase as shown in figure 1.2. When this light passes through a chiral material with a different absorbance for the two components, the sum of these components yields an ellipse and the difference in the ellipse axes approximately proportional to the circular dichroism of the material. This ellipticity is accompanied by a rotation angle θ of the polarisation plane when the phases of the two circular components become different due to circular birefringence (i.e different refractive indices for LCP and RCP).

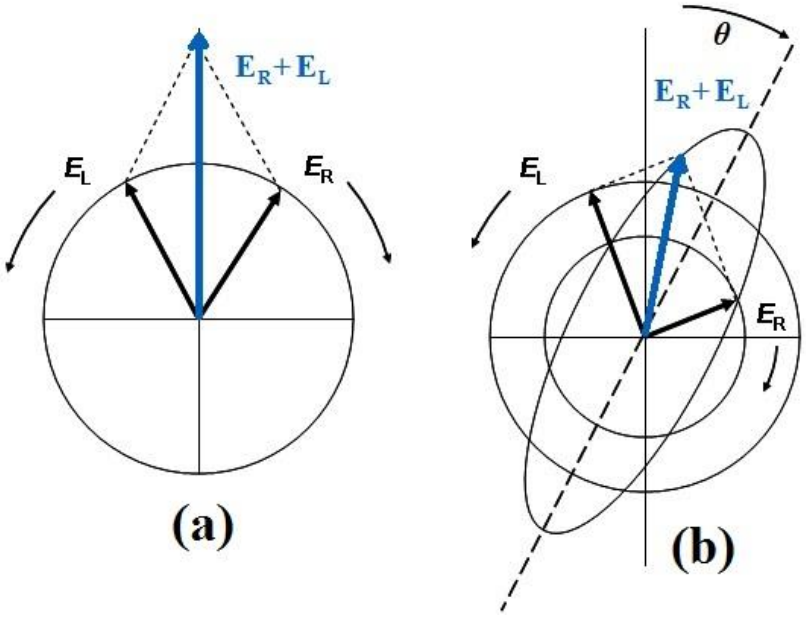

Fig 1.2: Schematic diagram showing: (a) Linear polarised light as a superposition of opposite circular polarised light of equal amplitude and phase, (b) different absorption of left and right hand polarised component leads to Circular Dichroism and rotation of plane polarised light by an angle θ [27]

Chiral media are composed of structures or molecules which are non-superimposable on their mirror image [1], left and right hand version of a chiral molecule are known as enantiomers. They have the same physical properties except for the way they rotate polarised light and interact with enantiomers of other compounds. In general, a molecule which in itself does not have a symmetry element (rotation, mirror) will be chiral. For example, in the case of a tetrahedral site such as a carbon atom with four different attached groups, as shown in figure (1.3). Such sites are called asymmetric or chiral centres; the central carbon represents the chiral centre. More complex molecules such as sugars and steroids may have n chiral centres, giving 2n stereoisomers and 2n-1 different pairs of mirror-image enantiomers [28].

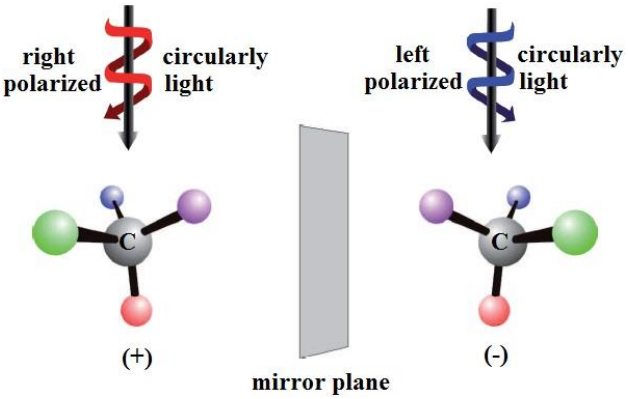

Fig 1.3: Schematic view of a chiral molecule with left and right circularly polarized light [28]

The symbols (+) and (-) shown in figure (3.1) which are sometimes placed before a compound's name, are used to indicate whether the enantiomer causes a clockwise or counter clockwise rotation of plane polarised respectively, and this rotation is called optical activity [29]. Since the first observation of polarization rotation in a quartz crystal by Arago in 1811 [30], optical activity has been a focus of activity in chemistry [31], biology [32], optics [33], and the study of fundamental symmetries in particle physics. When a LCP and RCP electromagnetic radiation traverses a chiral medium, the component matching the handedness of the material will propagate with different degrees of absorption and scattering. Furthermore, these two components will experience different indices of refraction and a nonzero phase difference will accumulate [29].

The electromagnetic behaviour of this chiral material reflects two effects. One is optical rotationary dispersion, which causes a rotation of the polarization plane of a linearly polarized light when it passes through the material and it is characterised by the planar azimuth rotation angle of elliptically polarised light [34]:

$$\theta = \frac{1}{2}\left[\arg(T_{++}) - \arg(T_{--})\right], \tag{5}$$

where T_{++} and T_{--} are the intensity or the electric field for the right and the left circularly polarised waves, respectively. The second effect is circular dichroism (a change in the polarisation from linear to elliptical) due to the difference in absorption of the LCP and RCP light. This circular dichroism is proportional to the ellipticity γ and it is expressed as follow [34]

$$\gamma = \frac{1}{2}\sin^{-1}\left[\frac{|T_{++}|^2 - |T_{--}|^2}{|T_{++}|^2 + |T_{--}|^2}\right]. \quad (6)$$

Circular dichroism spectroscopy is a valuable and an established technique which provides important information about the function and conformation of biomolecules that is not directly available from other conventional spectroscopic techniques such as fluorescence and absorbance [35] because it is extremely sensitive to changes in conformation. The long term interest in the THz circular dichroism is potentially in discriminating between different enantiomer of large molecules in the drug and food industries as the method might be able to detect large scale conformational changes in molecules [36]. Drug and some food products are manufactured in enantio-pure form to enhance their effectiveness or minimise side effects so that the development of rapid spectroscopic methods of establishing enantiomers purity is commercially important. At optical frequencies, this technique has been employed in the detection of conformational changes in proteins [36] and nucleic acids, estimation of secondary structures of proteins and polypeptides in solution [37, 38], determination of the nature of interactions between proteins and other macromolecules [36] and the study of proteins folding form [39]. However visible and UV circular dichroism measurements tend to probe local structure and have limitations when dealing with large molecules.

To determine absolute configurations and the changes in chiral molecules, there is evidently a need for more tools. In last few decades, various techniques have been explored, including a single-crystal X-ray diffraction (XRD) measurements using anomalous scattering [40, 41]. This requires high-quality single crystals and additionally, the crystal should be subject to anomalous scattering which, for standard XRD experiments, can be obtained by introducing heavy atoms. This method has been quite effective in determining chirality, but the requirement that samples be in crystalline form has limited its applicability. Other methods are nuclear magnetic resonance (NMR) [42], optical rotation [43-46] or stereospecific synthesis and electronic circular dichroism (ECD) [47-49]. The latter technique has been widely available for routine measurements since the early 1960s. ECD is a form of UV-Visible spectroscopy that relies on the differential absorption of a chiral molecule towards left and right circularly polarized light. A relatively new technique in this context is vibrational circular dichroism (VCD), which combines the stereochemical sensitivity of circular dichroism with the structural specificity of IR spectroscopy.

The initial aim of the work described in this thesis was to improve the sensitivity of the time domain terahertz circular dichroism spectroscopy to explore whether it could be used to measure optical activity and its coupling to low frequency molecular vibrations, and to perform exploratory studies of artificial chiral structures exhibiting large CD. To try and achieve these objectives, we first developed an optical system and signal processing techniques to achieve the sensitivity necessary to measure the very small changes in

polarisation anticipated at terahertz frequencies. Unfortunately we were not successful in measuring CD in molecules although the large effects produced by chiral materials were easily observed.

The structure of this thesis is organised into two major sections. The first part consists of Chapter 2 through 4 and presents work on the development of a polarisation-resolved time-domain terahertz spectrometer. The second part consists of Chapter 5 through 7, and describes the study of some chiral metamaterials.

In Chapter 2, the principle of time domain THz spectroscopy are outlined and a description of standard terahertz time-domain spectroscopy system is presented and experimental studies of different photoconductive (PC) receivers are discussed.

Chapter 3 provides a description of linear polarisers for polarisation sensitive THz spectroscopy. Experimental and computational studies of a pile-of-plates polarisers and three wire-grids polarisers are performed and a comparison of their performances is presented.

Chapter 4 describes two different polarisation analysis methods used to study the optical properties of artificial chiral materials. A novel polarisation sensitive THz-TDS spectrometer for the measurements of this optical activity is described.

Chapter 5 discusses experimental and computational studies of optical activity of metal screw hole arrays.

In chapter 6, a literature review of optical metamaterials and planar chiral metamaterials is presented. Experiments on a pair of crossed-gammadion planar structures are described and a theoretical equivalent model of this metamaterial is introduced.

Chapter 7 describes design and fabrication process of the quasi 2D and 3D chiral metamaterials investigated in this work. These chiral structures consist of square arrays of metallic spirals with four-fold symmetry. Experimental measurements of the polarisation response in the transmission regime are performed and compared with simulations to investigate the optical activity of both structures.

References

1. Zhang X.C. and Xu J., *Introduction to THz Wave Photonics.* Springer Science and Business Media, 2010.

2. Peter P.H., *THz for Space: The Golden Age.* Microwave Symposium Digest (MTT), 2010: p. 816-819.

3. Chan W.L., Deibel J., and Mittleman M.D., *Imaging with terahertz radiation.* Reports on Progress in Physics, 2007. **70**(8): p. 1325-1379.

4. Mittleman D.M., Jacobsen R.H., Neelamani R., Baraniuk R.G., and Nuss M.C., *Gas sensing using terahertz time-domain spectroscopy.* Apply. Phys. B, 1998. **67**: p. 379-390.

5. Cheville R.A. and Grischkowsky D., *Far-infrared foreign and self-broadened rotational linewidths of high-temperature water vapor.* J. Opt. Soc. Am. B, 1999. **16**: p. 317-322.

6. Ajito K. and Ueno Y., *THz Chemical Imaging for Biological Applications.* IEEE Transactions on Terahertz Science and Technology, 2011. **1**: p. 293-300.

7. Federici J.F., Schulkin B., Huang F., Gary D., Barat R., Oliveira F., and Zimdars D. , *THz imaging and sensing for security applications—explosives, weapons and drugs.* Semiconductor Science and Technology, 2005. **20**(7): p. S266-S280.

8. Yamamoto K., Tominaga K., Sasakawa H., Tamura A., Murakami H., Ohtake H., and Sarukura N., *Terahertz time-domain spectroscopy of amino acids and polypeptides.* Biophys J, 2005. **89**(3): p. L22-4.

9. Woodward R.M, Wallace V.P., Arnone D. D., Linfield E. H., and Pepper M., *Terahertz Pulsed Imaging of Skin Cancer in the Time and Frequency Domain.* Journal of Biological Physics, 2003. **29**: p. 257-261.

10. Daryoosh S., and Safieddin S.N., *Terahertz Photonics: Optoelectronic Techniques for Generation and Detection of Terahertz Waves.* Lightwave Technology, 2008. **26**: p. 2409-2422.

11. Dobroiu A., Otani C., and Kawase K., *Terahertz-wave sources and imaging applications.* Measurement Science and Technology, 2006. **17**(11): p. R161-R174.

12. Sirtori C., Barbieri S., and Colombelli R., *Wave engineering with THz quantum cascade lasers.* Nature Photonics, 2013. **7**(9): p. 691-701.

13. Grischkowsky D., Keiding S., Van Exter M., and Fattinger C., *Far-infrared time-domain spectroscopy with terahertz beams of dielectrics and semiconductors.* J. Opt. Soc. Am. B, 1990. **7**: p. 2006-2015.

14. Sang-Gyu P., Michael R.M., and Andrew M.W., *Analysis of Terahertz Waveforms Measured by Photoconductive and Electrooptic Sampling.* Journal of Quantum Electronics,1999. **35**: p. 810-819.

15. Gerard M., Charles V.S., and Daniel B., *Picosecond microwave pulse generation.* Applied Physics Letters, 1981. **38**: p. 470.

16. Auston D.H., Cheung K.P., and Smith P.R., *Picosecond photoconducting Hertzian dipoles.* Applied Physics Letters, 1984. **45**(3): p. 284.

17. Auston D.H., Nuss M.C., *Electrooptic Generation and Detection of Femtosecond Electrical Transients.* IEEE Journal of Quantum electronics, 1988. **24**: p.1984-1997.

18. Jeon T.I., and Grischkowsky D., *Characterization of optically dense, doped semiconductors by reflection THz time domain spectroscopy.* Applied Physics Letters, 1998. **72**(23): p. 3032.

19. Brorson S.D, Buhleier R., Trofimov I.E., White J.O., Ludwig Ch., and Balakirev F.F., *Electrodynamics of high-temperature superconductors investigated with coherent terahertz pulse spectroscopy.* Opt. Soc. Am. B, 1996. **13**: p. 1979-1993.

20. Wilke I., Khazan M., Rieck C.T., Kuzel P., Kaiser T., Jaekel C., and Kurz H., *Terahertz surface resistance of high temperature superconducting thin films.* Journal of Applied Physics, 2000. **87**(6): p. 2984.

21. Robertson W., Arjavalingam G., Meade R., Brommer K., Rappe A., and Joannopoulos J., *Measurement of photonic band structure in a two-dimensional periodic dielectric array.* Physical Review Letters, 1992. **68**(13): p. 2023-2026.

22. Aoki T., Wada T.M., Haus J., Yuan Z., Tani M., Sakai K., Kawai N., and Inoue K., *Terahertz time-domain study of a pseudo-simple-cubic photonic lattice.* Physical Review B, 2001. **64**: p. 045106.

23. Jepsen P. Uhd., Moller U., and Merbold H., *Investigation of aqueous alcohol and sugar solutions with reflection terahertz time-domain spectroscopy.* OPTICS EXPRESS, 2007. **15**(22): p. 17417.

24. Du S.Q., Li H., Xie L., Chen L., Chen L., Peng Y., Zhu Y.M., Li H., Dong P. and Wang J.T., *Vibrational frequencies of anti-diabetic drug studied by terahertz time-domain spectroscopy.* Applied Physics Letters, 2012. **100**(14): p. 143702.

25. Moller K.D., and Rothschild W.G., *Far-infrared Spectroscopy (Pure & Applied Optics).* John Wiley and Sons Inc, 1971.

26. Xu J., Galan J., Ramian G., Savvidis P., Scopatz A., Birge R.R., Allen S.J., and Plaxco K., *Terahertz circular dichroism spectroscopy of biomolecules.* Proceedings of SPIE, 2004. **5268**: p. 19-26.

27. Dreiling J., and Gay T., *Polarized electron - Chiral Molecule Scattering experiments.* University of Nebraska - Lincoln.

28. M. Urbanova, V.S., K. Volka, B. Jun, D. L. Weaver, C. P. Schultz, M. Boese, H. H. drews, *Fourier transform vibrational circular dichroism (FT-VCD) spectroscopy.*

29. Elezzabi A.Y., and Sederberg S., *Optical activity in artificial chiral media: a terahertz time domain investigation of Karl F. Lindman's 1920 pioneering experiment.* Optics Express, 2009. **17**(8): p. 6600.

30. Chau K.J., Quong M.C., and Elezzabi A.Y., *Terahertz time domain investigation of axial optical activity from a sub-wavelength helix.* Optics Express, 2007. **15**(6): p. 3557.

31. Barron L.D., *Molecular light scattering and optical activity.* Cambridge University Press, 1982.

32. Mason S.F., *Molecular optical activity and the chiral discriminations.* Cambridge University Press, 1982.

33. Born M., and Wolf E., *Principles of Optics 5th Ed.* Pergamon Press, Oxford, 1975.

34. Wang B., Zhou J., Koschny T., Kafesaki M., and Soukoulis C.M., *Chiral metamaterials: simulations and experiments.* Journal of Optics A: Pure and Applied Optics, 2009. **11**: p. 114003.

35. Martin S.R., and Schilstra M.J., *Circular Dichroism and its Applications to the Study of Biomolecules.* Methods in Cells Biology, 2008. **84**: p. 263-293.

36. Wallace B.A., and Janes R.W., *Circular dichroism and synchrotron radiation circular dichroism spectroscopy: tools for dru discovery.* Strucural Biology in Drug Metabolism and Drug Discovery, 2003. **31**: p. 631-633.

37. Gopal R., Park J.S., Seo C.H., and Park Y., *Applications of circular dichroism for structural analysis of gelatin and antimicrobial peptides.* Int J Mol Sci, 2012. **13**(3): p. 3229-44.

38. McPhie P., *Concentration-independent estimation of protein secondary structure by circular dichroism: a comparison of methods.* Anal Biochem, 2008. **375**(2): p. 379-81.

39. Kim S. J., Born .B., Havenith M., and Gruebele M., *Real-time detection of protein-water dynamics upon protein folding by terahertz absorption spectroscopy.* Angew. Chem. Int. Ed., 2008. **47**: p. 6486-6489.

40. Flack H.D., and Bernardinelli G., *Absolute structure and absolute configuration.* Acta Cryst. Section A, 1999: p. 908-915.

41. Flack H.D., and Bernardinelli G., *Reporting and evaluating absolute-structure and absolute-configuration determinations.* Applied Crystallography, 2000. **33**: p. 1143-1148.

42. Hoye T.R., and Kultun D.O., *An NMR strategy for determination of configuration of remote stereogenic centers: 3-Methylcarboxylic Acids.* Am. Chem. Soc., 1998. **120**: p. 4638-4643.

43. Stephens P. J., McCann D.M., Cheeseman J.R., and Frisch M.J., *Determination of absolute configurations of chiral molecules using ab initio time-dependent Density Functional Theory calculations of optical rotation: how reliable are absolute configurations obtained for molecules with small rotations?* Chirality, 2005. **17 Suppl**: p. S52-64.

44. Stephens P.J., Devlin F.J., Cheeseman J.R., and Frisch M.J., *Calculation of optical rotation using density functional theory.* Phys. Chem. A, 2001. **105**: p. 5356-5371.

45. Polavarapu P.L., Petrovic A., and Wang F., *Intrinsic rotation and molecular structure.* Chirality, 2003. **15**: p. S143-S149.

46. Stephens P.J., Devlin F.J., Cheeseman J.R., Frisch M.J., and Rosini C., *Determination of Absolute Configuration Using Optical Rotation Calculated Using Density Functional Theory.* Organic Letters, 2002. **4**: p. 4595-4598.

47. Uray G.G., Verdino P., Belaj F., Kappe C.O., and Fabian W.M., *Absolute configuration in 4-Alkyl- and 4-Aryl-3, 4-dihydro-2 (1H)-pyrimidones: A combined theoretical and experimental investigation.* Org. Chem., 2001. **66**: p. 6685-6694.

48. Pescitelli G., Gabriel S., wang Y., Fleischhauer J., Woody R.W., and Berova N., *Theoretical analysis of the Porphyrin- Porphyrin exciton interaction in circular dichroism spectra of Dimeric Tetraarylporphyrins.* Am. Chem. Soc., 2003. **125**: p. 7613-7628.

49. Vandyck K., Matthys B., and Van der Eycken J., *Synthesis and absolute configuration of (1S,8S)-as-hydrindacene-1,8-diol as determined by the circular dichroism exciton chirality method.* Tetrahedron Letters, 2005. **46**(1): p. 75-78.

Chapter 2

Principles of THz Time-domain Spectroscopy

2.1 Introduction

Terahertz time domain spectroscopy is attracting considerable attention due to the wide range of applications and physical phenomena which can be studied in this until recently inaccessible part of the spectrum. In some applications, for example measurement of the Hall effect [1], it is necessary to perform sensitive detection of the polarisation state of terahertz waves [2]. Several techniques can be used to determine changes in the polarisation of terahertz waves. Most rely on the mechanical rotation of an optical element such as an electrooptic crystal for detecting the terahertz radiation [3] or a wire-grid polariser [4]. Unfortunately mechanical rotation limits the measurement time to about 10 ms (100 Hz) [2] which slow when using the terahertz time-domain spectroscopy technique, since an optical delay line is additionally moved. A detection using two separate detectors by splitting the radiated terahertz beam and using the development of techniques to measure orthogonal fields simultaneously has emerged as a solution to the above problem. For example detection of the terahertz waveform can be performed using a photoconductive antenna device with multiple electrodes [5, 6].

Here, we will describe a standard optoelectronic terahertz time-domain spectroscopy system employed in our experiment which is based on an optical pump and probe setup. We will also describe the transmitter and the receiver devices used for the generation and the detection of terahertz radiations and highlight those features determining the sensitivity and the frequency range of the system. We will then describe results obtained by replay the usual photoconductive dipole antenna (which detects only one polarisation) with a four contact crossed-bowtie antennas which can detect orthogonal field components.

2.2 Basic spectroscopy design

In this present work, the measurement techniques are based on a time-domain THz spectroscopy system which uses a self-mode-locked Ti: Sapphire laser optically pumped by a continuous-wave (cw) argon laser with an average output power of ~ 800 mW. This femtosecond laser produces optical pulses of 70 to 130 fs durations at an 82 MHz repetition

rate and a central optical wavelength tunable over the range of 740 to 820nm. Optical pulses are split into two arms; pump and probe as presented in figure 2.1. The pump beam is used to generate the THz pulse, while the probe beam is used to sample the terahertz field at the receiver.

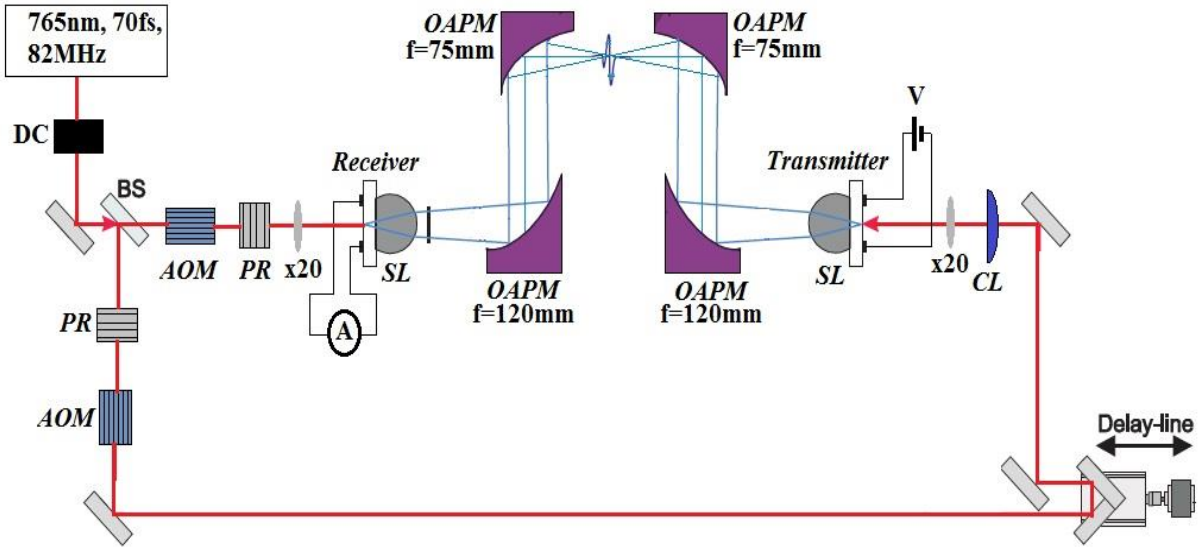

Fig 2.1: Conventional THz time domain spectrometer. BS: beam splitter, PR: polarisation rotator, AOM: acousto optic modulator, CL: cylindrical lens, SL: silicon lens, OAPM: off-axis parabolic mirror, DC: dispersion compensation.

The laser beam traverses a pair of SF18 prisms (not shown) to compensate the material dispersion in the optical system (particularly the modulators) by introducing negative group velocity dispersion. The beam is then divided by a beam splitter into pump and probe pulses. Approximately 11% of the laser power (~90 mW) is sent to the pump arm, and 3% of the laser power (~20 mW) to the probe arm. An acoustic-optic modulator (AOM) is used to chop the pump beam at a frequency of 6.5 kHz to allow signal detection with a lock-in amplifier to improve signal to noise ratio. Narrower bandwidth detection, improve signal-to-noise ratio by limiting the noise bandwidth. A cylindrical lens and a x20 microscope objective are placed before the transmitter to focus the laser beam onto the biased gap of the photoconductive transmitter antenna with an area ($1/e^2$ diameter) of ~ 4 μm × 100 μm [5]. This line focus is important because it allows maximizing the transmitter output without thermal runaway or dielectric breakdown. Two hyper hemispherical silicon lenses are used, the first one on the back of the receiver to improve the collection efficiency of the terahertz radiation [7] and the second one on the back of the transmitter as shown in figure 2.2 to collimate the incident beam and to avoid losses due to total internal reflection of the generated terahertz radiation at the substrate-air interface. The silicon lenses have high resistivity which gives low absorption and low dispersion over the terahertz frequency

range. For a collimated incident beam, the specific design of the hyper hemispherical silicon lens according to geometrical optics is given by,

$$h = R\frac{n}{n-1}, \tag{1}$$

where h is the effective lens height, R is the radius, and n is the Si refractive index of 3.42.

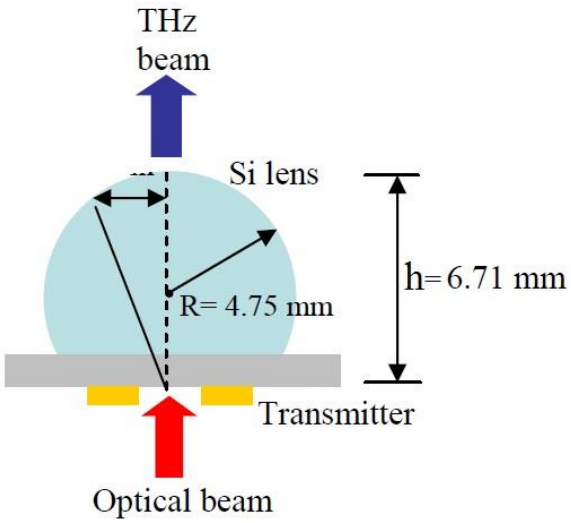

Fig 2.2: Diagram of the transmitter- silicon lens assembly

Because of diffraction, a pair of off-axis parabolic mirrors is also needed after the transmitter and before the receiver measuring the terahertz electric field to respectively collimate and focus the terahertz radiation. The alignment of the laser spot on the transmitter and the receiver chip as well as the alignment of the silicon lenses to a precision of a few μm are necessary to optimise the sensitivity and the bandwidth of the signal. A sample to be studied is positioned in either the collimated beam or at the focus between the two central parabolic mirrors. Since temporal overlap between the THz pulse and the probe pulse is required to measure the THz electric temporal waveform, a fast scanning retro-reflector is used to vary the time delay between the probe pulse and THz pulse. Signals are then acquired on a digital averaging scope.

In our apparatus, which uses room temperature, optically gated photoconductive sources and detectors described in the next two sections, the data are collected in the time domain and are Fourier transformed to extract the frequency-dependent amplitude and phase which allow probing of the real and imaginary parts of the dielectric function of materials.

Extremely high signal-noise ratios of up to 10^6 in electric field make the technique very powerful despite the low average source power of typically 10 µW.

2.3 Optoelectronic generation of THz radiation

For the generation of THz radiations with femtosecond pulses, various emitter concepts have been employed in order to obtain high THz emission efficiency and bandwidth [8], such as difference frequency mixing [9], surface field THz emitters [10], photoconductive antennas [11, 12] and photoconductors with large area interdigitated electrodes [5, 13]. Of these, simple photoconductive antennas are the most widely used nowadays to generate terahertz pulses.

Since applications generally require large bandwidth, we use in this present work a nonresonant antenna for the generation of terahertz pulses as it generally has a broader bandwidth compared to a dipole. The geometry of this antenna is a coplanar waveguide, with Ti/Au electrodes deposited on the surface of a semi-insulating gallium arsenide (SI-GaAs). SI-GaAs is an appropriate substrate because of its high carrier mobility and high breakdown field. The metallization of the three electrodes of the antenna shown in figure 2.3 consists of 20 nm of titanium (Ti) and 200 nm of gold processed by conventional photolithography on the semi-insulating GaAs.

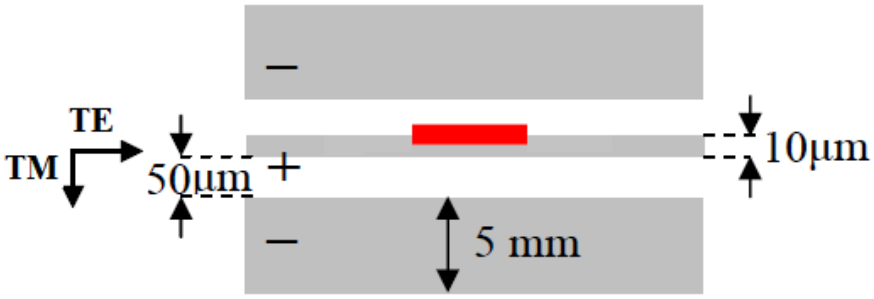

Fig 2.3: Schematic diagram showing the position of the exciting beam (red spot) and the electric and magnetic field direction for TE and TM excitation.

The fabrication process of the antenna is as follows: First a positive photoresist was spun and then baked to harden the resist and improve adhesion. Exposure and development of the chip was then followed by removal of oxide from the sample surface to improve the metal contacts, and by metallisation using a thermal evaporator. To ensure easy metal lift-off in the final step, the sample was washed in chlorobenzene before developing. Figure 2.4 shows complete process used to manufacture both transmitter and receiver, which differ only in the substrate and electrode patterns.

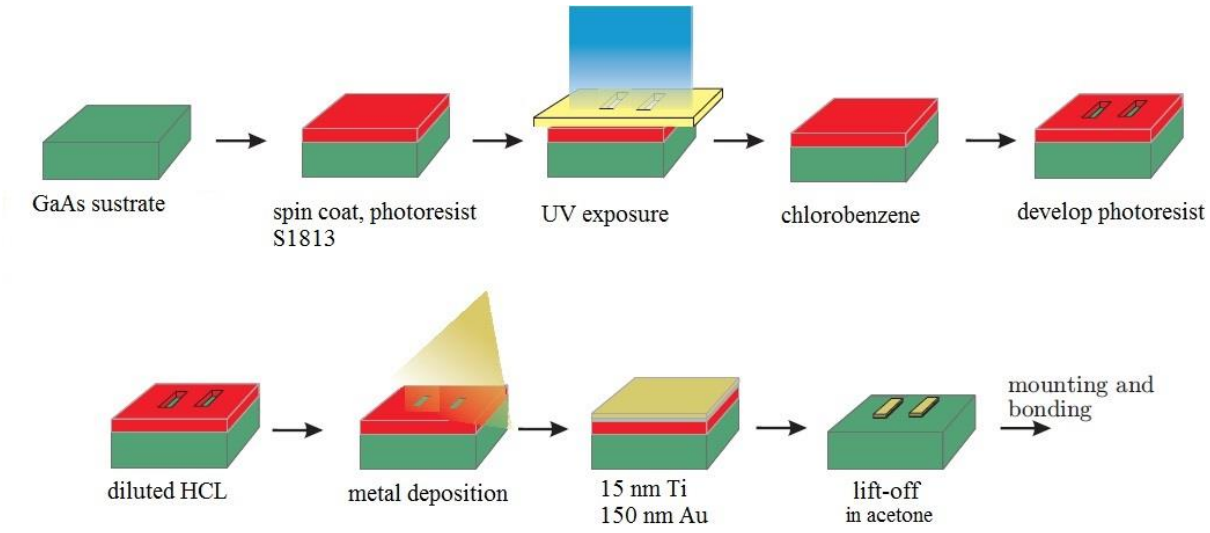

Fig 2.4: Photolithographic process used to manufacture the PC terahertz devices

An external bias of ~ 50V is applied between the transmitter tracks which are separated by a gap of 50μm. Pulses with a centre wavelength of typically 765 nm, a duration of ~ 70 fs and an average power of 36 mW are focussed onto the device so as to slightly overlap the junction between the central positively biased electrode and the semiconductor substrate. In all experiments, the applied bias was restricted to keep the average photocurrent below ~1 mA because above this value the device lifetime was found to be noticeably reduced. The dimensions of the coplanar transmitter, the exciting beam and the direction of polarization for TE and TM optical excitation are shown in figure 2.3. For TE the electric-field vector is parallel to the direction of the tracks and for TM the magnetic-field is perpendicular to this direction. The transmitter efficiency is higher for TM illumination [5].

When an ultrafast laser pulse illuminates the photoconductive gap between electrodes, electron-hole pairs are created and reduce strongly the resistivity of the material and the energy electric release in the form of terahertz pulses as the carriers accelerate to the electrodes. It should be noted that the photon energy of the laser must be sufficient for the excitation of photocarriers over a bandgap. The photon energy our femtosecond laser is ~ 1.56 eV which is enough to generate photocarriers through a direct interband transition in GaAs as at 300K, E_g(GaAs) = 1.43 eV. The acceleration of photocarriers is driven by the electric field, which is externally applied. Under the effect of the voltage V, the electron-hole pairs are accelerated and lead to a rapid change in the current density. The changing dipole produces a THz transient in the antenna that is radiated into free space. The shape of the pulse and hence the frequency distribution depend on the design of the antenna, the excitation pulse width and the carrier dynamics [14]. Figure 2.5 illustrates the principle of the generation of pulsed terahertz radiation.

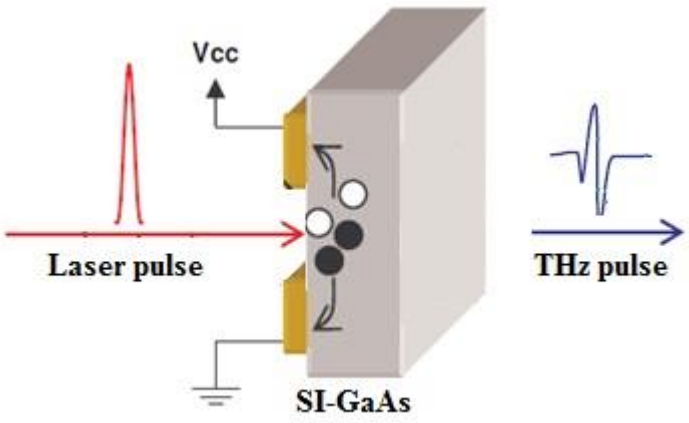

Fig 2.5: Principle of a terahertz pulse generation using a photoconductive antenna

The electrostatic energy E_c of the transmitter antenna stored by the parallel metallic electrodes is expressed as:

$$E_c = \frac{1}{2} CV^2, \tag{2}$$

where C is the capacitance of the antenna gap and V is the bias voltage applied. Some of this energy can be converted into terahertz radiation under the excited laser pulsed of the gap between the electrodes to THz radiations. Since electrons in GaAs have much higher mobility than holes, the contribution of the holes can be ignored. The current density is described by

$$J(t) = N(t)ev(t), \tag{3}$$

where N is the density of photoexcited electrons , e the elementary electron charge and v is the electron velocity. The carrier density N is a function of time and determined by the laser pulse shape and the carrier lifetime. The time dependence of the carrier density $N(t)$ is given by

$$\frac{dN}{dt} = G(t) - \frac{N(t)}{\tau_c}, \tag{4}$$

where $G(t)$ is the generation rate describing the generation of free carriers on the time scale of the laser, and τ_c is the carrier trapping describing the evolution of the carrier density at

longer times, which is ~ 100 ps for SI-GaAs. The equation of the electron motion is given by,

$$\frac{dv}{dt} = -\frac{v}{\tau_s} + \frac{e}{m^*} E(t), \tag{5}$$

where τ_s is the mobility scattering time, m^* is the effective mass and $E(t)$ is the bias field across the antenna gap.

Since the photocurrent varies in time, it radiates an electromagnetic pulse, whose electric field in the far-field point dipole approximation is given by the relation [15]

$$E_{THz} \propto \frac{\partial J}{\partial t} \approx ev(t)\frac{\partial G(t)}{\partial t} + G(t)e\mu\frac{\partial E(t)}{\partial t}, \tag{6}$$

where J is the photocurrent density and μ is the carrier mobility which is independent of time if $\omega\tau_s << 1$. The far-field electric field amplitude expected from equation (6) as well as the normalised temporal profiles of the optical pulse intensity and the transmitter photocurrent are shown in figure 2.6. Equation (6) does not take into the account the effects of field screening [16] which tends to give a sharper negative going field transient. In this model calculation, the optical pulse profile is a Gaussian with width of 100 fs, the mobility scattering time is 30 fs and a carrier recombination time is 300 fs (appropriate for low temperature GaAs). The free carrier density is assumed to follow a single exponential decay and the bias field is assumed to be constant over the illuminated area [17].

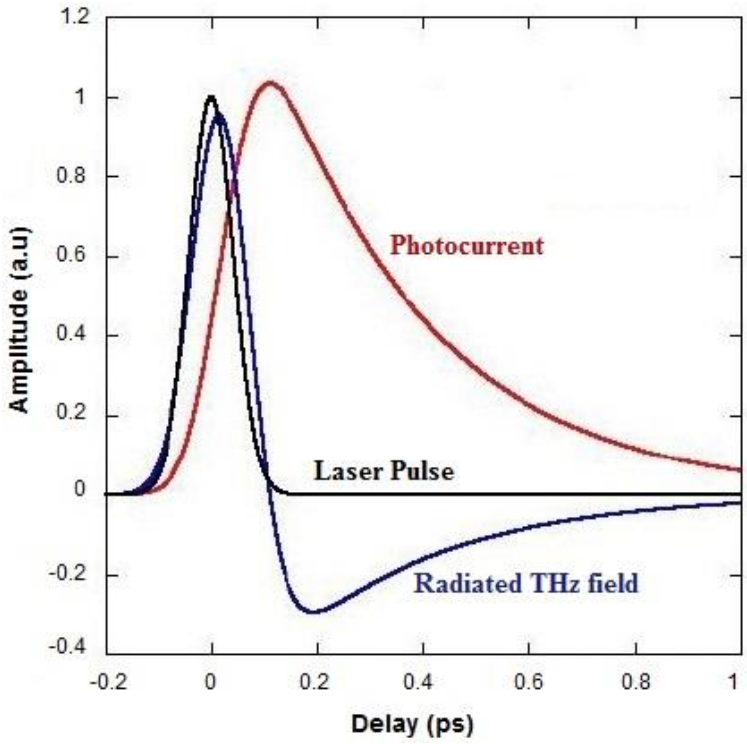

Fig 2.6: Time variation of the transient photocurrent (red), the laser pulse (black) and the radiated electric far-field (blue).

Figure 2.6 suggests that the terahertz pulse bandwidth is mainly determined by the fast rise-time of the photocurrent and that the terahertz pulse shape is not strongly affected by the photocarrier lifetime. The efficiency of the transmitter is proportional to the dc carrier mobility and the bias field when the illumination level is low. We can increase the energy of the terahertz pulse by increasing the bias field and pump power but this is limited by dielectric breakdown of the transmitter. This breakdown can be grouped into two categories: field induced breakdown and thermal induced breakdown. The breakdown caused by the field usually happens when the bias field is higher than the breakdown field of the semiconductor material. And the heating of the substrate causes the thermal breakdown by photocurrent flow in the substrate. Most breakdowns of photoconductive antennas in terahertz wave generation are thermally induced except for those having a very small gap or high bias.

The terahertz signal bandwidth can also be affected by the position of the irradiating laser beam on the transmitter antenna gap as reported in reference [18]. The amplitude of the signal increases on approaching the electrodes reflecting the highly non uniform electric field distribution due to the presence of traps in the GaAs and that the emission of the terahertz radiation near the cathode is weaker than the emission near the anode due to the high mobility of electrons compared with holes and the direction of the acceleration. This explains why only the edge of the central track is illuminated in figure 2.3.

2.1 Photoconductive detection

Photoconductive antennas are extensively used in terahertz imaging systems [28] and THz spectroscopy systems [22, 29, 30]. The first photoconductive terahertz receivers described in the literature were fabricated on radiation damaged silicon-on-sapphire (SOS) by Auston et al [29]. Since then, there have been various advances in the field of photoconductive (PC) terahertz detection. In particular, new antenna geometries have been developed for polarization sensitive detection [31, 32] such as the four-contact photoconductive antenna [19, 33] and the three-contact photoconductive antenna [34]. In this present work we used two types of photoconductive receiver; conventional dipole PC antenna and a crossed-bowtie PC antenna to detect the generated terahertz pulses. This photoconductive antenna is based on a ~1μm thick epitaxial layer of low temperature substrate GaAs (LT-GaAs) of 200 ^{o}C to 350 ^{o}C compared to a conventional GaAs which is grown at 550 ^{o}C to 650 ^{o}C, on a semi-insulating (SI) substrate with an intervening 100 nm layer of AlAs. The interlayer of AlAs is larger because it reduces noise from carriers created in the SI substrate. A carrier life time in a range of 0.3 to 1 ps and a mobility of ~ 3000 cm^2/Vs were measured in optical pump-probe terahertz experiments [5]. Such properties make LT-GaAs receivers attractive and ideal for the detection of femtosecond terahertz pulses.

The principle of the detection of THz pulses is as follows: The photoconductive gap of a receiver antenna is normally of low resistance when is excited with a femtosecond laser pulse, which is separated from the pump beam used for THz generation using a beam splitter as shown in figure 2.1. The conductivity of the gap increase the electric field of the terahertz pulse focused on the PC receiver induces a transient current in the photoconductor when it is incident on the detector antenna synchronously with the gating pulse. Since the photocurrent is usually very weak (on the order of pA to nA), it is amplified by a current amplifier and detected with a lock-in amplifier implemented at 6.5 kHz. To sample the time-domain waveform, the relative delay between the pump and gating pulses is varied using a translation stage equipped with an optical reflector. Figure 2.7 illustrates the principle of the THz pulse detection using a dipole photoconductive receiver.

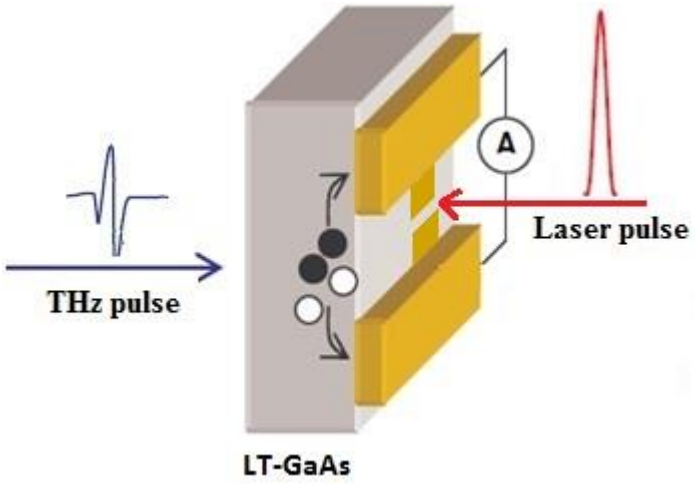

Fig 2.7: Schematic diagram shows principle of photoconductor detection of pulsed terahertz radiation.

The temporal resolution is mainly determined by the duration of the gating pulse and the antenna design whilst the carrier lifetime plays only a minor role. The current induced by the terahertz field is [5]

$$J(t) = N(t)e\mu E, \tag{7}$$

where N is the density of photogenerated carriers created by the probe beam, e the elementary charge, μ the mobility of electron, and E is the bias electric field. The density of photogenerated carriers is a function of time and depends on the probe beam pulse width and the carrier lifetime in the photoconductive material, and it is given by

$$\frac{dN}{dt} = G(t) - \frac{N(t)}{\tau_c}, \tag{8}$$

where $G(t)$ is the carrier generation rate of the laser pulse and τ_c is the carrier trapping time in the photoconductive material (~ 100 ps for SI-GaAs and ~ 1 ps for LT-GaAs).

For a broad spectrum response, the maximum current should be induced at the first resonant frequency. This frequency is given by [35],

$$\upsilon = \frac{c}{2L\sqrt{\varepsilon_r}}, \tag{9}$$

where ε_r is the relative dielectric constant of the material, c is the speed of light in vacuum, and the L is the effective antenna length which is estimated:

$$L = L_m + 2w, \tag{10}$$

where L_m is the length of the antenna and w the width of the antenna transmission line. The effective permittivity should lie between the air and the substrate permittivity.

We define the dynamic range of a terahertz system as the ratio between the maximum measured signal amplitude and the *RMS* receiver noise. The receiver noise is dominated by thermal noise, also called Johnson or Nyquist noise. The thermal noise current is given by [22].

$$I_{RMS} = \sqrt{\frac{4kT\Delta f}{R}}, \tag{11}$$

where k is Boltzman's constant, T is the temperature, Δf is the bandwidth, and R is the average resistance of the photoconducting gap which is typically ~1MΩ when it is illuminated. There are also two additional, smaller noise sources. One is shot noise of the dc photocurrent generated by the gating laser beam in the absence of a THz field. It arises from small, asymmetric Schottky barriers of the metal-semiconductor contacts and it is given by

$$I_{RMS} = \sqrt{2ei_{dc}\Delta f} \tag{12}$$

The other is the noise current due to the contribution of laser noise to the dc photocurrent noise and given by

$$I_{RMS} = \alpha i_{dc}\sqrt{\Delta f}, \tag{13}$$

where α is the fractional laser noise (~ 10^{-6} $Hz^{-1/2}$ at 6.5 kHz chopping frequency) and i_{dc} is the dc photocurrent.

In this work, a dipole and crossed-bowtie photoconductive detector antennas were used. The dipole receiver consist of a pair of 10 µm wide parallel Ti/Au tracks separated by 10 µm on a LT-GaAs photoconductive layer, and the crossed-bowtie PC antenna receiver is based on two perpendicular Ti/Au bowtie antennas used to contact a 50 µm square photoconducting gap on a LT-GaAs photoconductive layer and a germanium (Ge) window to avoid the coupling between the antenna arms. Each antenna is connected to a separate differential current amplifier and lock-in detector, thus allowing simultaneous measurement of the signal currents along the *x*-axis and the *y*-axis; the current I_x and I_y. Figure 2.8 (a) and figure 2.8 (b) show respectively a schematic diagram of the dipole and the crossed-bowtie photoconductive receivers.

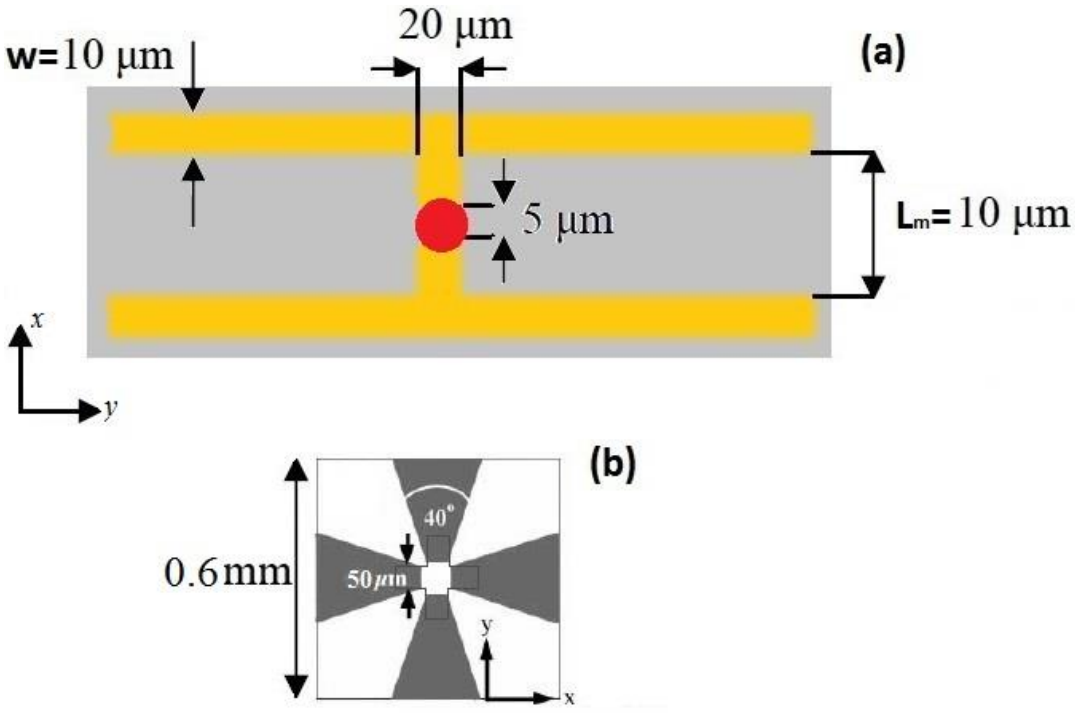

Fig 2.8: Schematic diagram showing the dimensions of (a) a dipole PC antenna receiver and the positioning of the focussed laser in red, and (b) the dimensions of a crossed-bowtie PC antenna device.

It should be noted that in system optimization, to achieve high bandwidth and sensitivity, we should also take into account the THz source, the alignment of the high resistivity silicon collimating substrate lens relative to the photoconducting gap which must be performed to a precision of order a few tens of µm, the polarization angle of the receiver gate beam which should be set perpendicular to the metal edges of the photoconducting switch [5], the off-axis parabolic mirrors that couple radiation between the transmitter and receiver substrate lenses should be positioned so as to obtain unity transfer function.

2.5 System characterisation

An example of the time domain signal obtained using the dipole receiver is shown in figure 2.9. The output of the terahertz source is linearly polarised along the *x*-axis and the dipole photoconductive antenna is designed as to detect only the electric field parallel to the incident radiation.

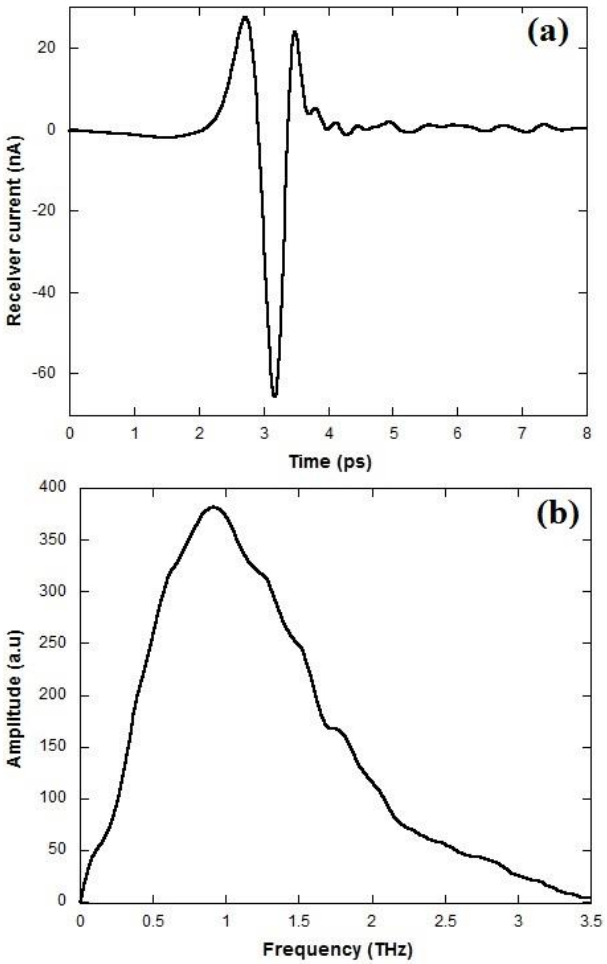

Fig 2.9: (a) THz transient detected using a LT-GaAs 10 µm dipole antenna. (b)The corresponding amplitude spectrum.

The time-domain trace in figure 2.9 (a) displays a small positive peak preceding the main negative transient which is due to the frequency dependence of the focal spot size of the silicon receiver lens. The large positive peak following the main negative is due to dynamic screening of the transmitter bias field [17]. The peak to peak receiver current, which is roughly proportional to the terahertz electric field, is ~ 90 nA. The corresponding spectrum of the signal is shown in figure 2.9 (b). The peak response is near 1 THz and the

detection bandwidth at 10% amplitude is ~ 2.9 THz. The noise current is ~ 400 fA/Hz$^{-1/2}$ which is consistent with the predictions of equations (11) to (13).

An example of signals obtained with terahertz pulses polarised along *x* using a crossed bowtie receiver are shown in figure 2.10. The experiment was performed using the same experimental setup as in figure 2.1 but with two linear polarisers in front of the receiver. The gate beam had a diameter equal to the electrode separation and was positioned so as to minimize the resistance between each pair of electrodes. The terahertz beam was positioned on the antenna so as to maximize the THz signal in both arms of the PC antenna with incident polarisation at 45^{o}.

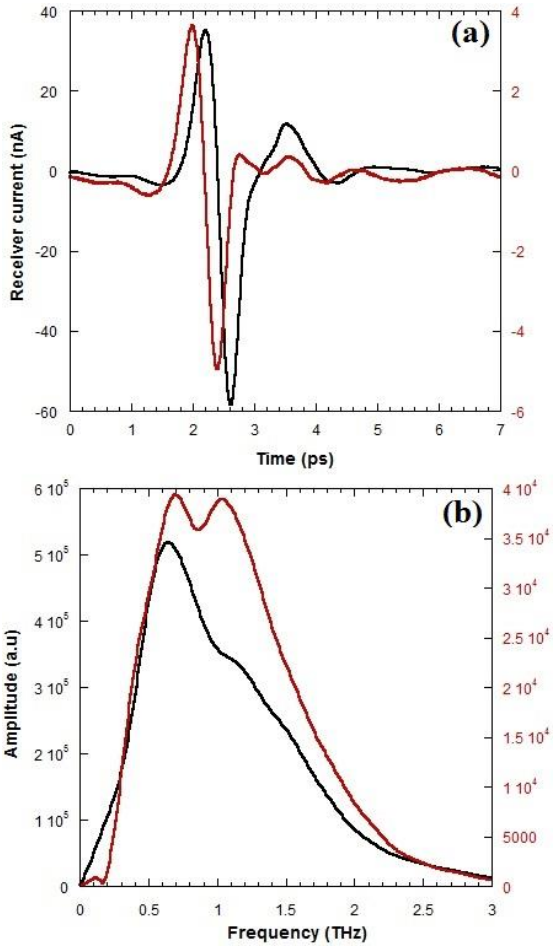

Fig 2.10: (a) and (b) are respectively the time-domain traces and their corresponding spectra obtained using a crossed-bowtie receiver of the electric field components of the THz pulse polarised along x-axis. (black) the electric field component polarised along x-axis and (red) the electric field component polarised along y-axis.

From figure 2.10 (a) of the electric field component polarised parallel to the incident radiation, we notice that the value of the peak to peak signal is larger using the crossed-bowtie receiver (~100 nA) than for the 10 μm receiver device (~90 nA) shown in figure 2.9

(a). Additionally, the spectrum in figure 2.10 (b) exhibits a 10% bandwidth detection of ~2.2 THz which is smaller than 2.9 THz bandwidth of the dipole. The time domain trace in figure 2.10 (a) shows also the electric the electric field component polarised perpendicular to the incident radiation of a peak to peak amplitude of the receiver current of ~ 8.7 nA, giving a field extinction ratio of ~ 11.5 which is smaller than the expected ratio and the ratio measured using the dipole antenna receiver.

To further understand this small ratio, we have placed two identical gold silica polarisers before the quadrant receiver antenna to try and eliminate the *y* polarised field, and we measured the *x* and *y* arm signals. Figure 2.11 shows the time-domain measurements of the electric components of the THz pulse and the calculated first derivative of the measured electric field component polarised parallel to the incident radiation.

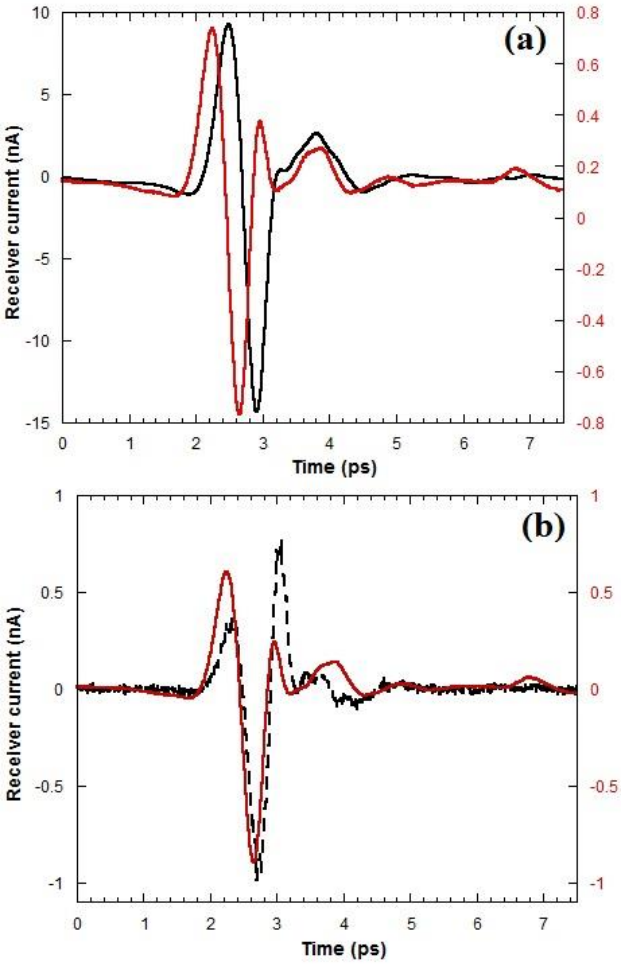

Fig 2.11: (a) Time domain traces of the measured (black) the electric field component polarised along x-axis and (red) the electric field component, using a crossed-bowtie receiver and two identical polarisers before the receiver. (b) The measured signal polarised along y-axis (red) and the calculated first derivative of the signal polarised along x-axis (black dashed).

Figure 2.11 (a) of the measured electric field components shows a peak to peak amplitude of ~ 24 nA and ~ 1.5 nA respectively of the component polarised parallel and perpendicular to the incident radiation, giving a field extinction ratio of ~ 16. It is clear from figure 2.11 (b) showing the calculated first derivative of the *x* signal and the time-domain signal of the detected terahertz radiations along *y* axis using a crossed-bowtie receiver device that the terahertz electric field component polarised perpendicular to the to the polarised radiation is proportional to the first derivative of the electric field component polarised parallel to the incident radiation. This is also observed when the polarisers are removed which leads us think that the *y*-polarised signal is probably due to capacitive coupling between orthogonal antenna arms.

2.6 Summary

In this chapter we have described the principles of an optoelectronic THz time-domain spectroscopy (TDS) system and details of the basic system that we have modified to perform polarisation resolved spectroscopy. There modifications are detailed in the following two chapters.

We have studied and compared the terahertz response sensitivity of a 10 μm dipole and a crossed-bowtie photoconductive receivers. The results showed a broader detection bandwidth using a dipole photoconductive receiver than the crossed-bowtie antenna device, and a significant cross-talk between orthogonal arms of the crossed-bowtie antenna due to capacitive coupling which make this device undesirable for sensitive polarisation resolved spectroscopy. In chapter 4, we describe a different and more sensitive approach using two separate detectors.

References

1. Mittleman D.M., Cunningham J., Nuss M.C., and Geva M., *Noncontact semiconductor wafer characterization with the terahertz Hall effect.* Appl. Phys. Lett., 1997. **71**: p. 16-18.

2. Yasumatsu N., Kasatani A., Oguchi K., and Watanabi S., *High-speed terahertz time-domain polarimeter based on an electro-optic modulation technique.* Applied Physics Express, 2014. **7**(9): p. 092401.

3. Yasumatsu N., and Watanabe S., *Precise real-time polarization measurement of terahertz electromagnetic waves by a spinning electro-optic sensor.* Rev Sci Instrum, 2012. **83**(2): p. 023104.

4. Morris C.M., Valdes Aguilar R., Stier A.V., and Armitage N.P., *Polarization modulation time-domain terahertz polarimetry.* Optics Express, 2012. **20**(11): p. 12303.

5. Andrews S.R., Armitage A., Huggard P.G., Hussain A., *Optimization of photoconducting receivers for THz spectroscopy.* Phys. Med. Biol., 2002. **47**: p. 3705-3710.

6. Castro-Camus E., Lloyd-Hughes J., Johnston M.B., Fraser M.D., Tan H.H., and Jagadish C., *Polarization-sensitive terahertz detection by multicontact photoconductive receivers.* Applied Physics Letters, 2005. **86**(25): p. 254102.

7. Martin van Exter, Fattinger Ch., and Grischkowsky D., *Terahertz time-domain spectroscopy of water vapor.* Optics Letters, 1989. **14**: p. 1128-1130.

8. Hunag Y., and Li D., *Comparison of terahertz antennas.* University of Liverpool review.

9. Rice A., Jin Y., Ma X.F., Zhang X.-C., Bliss D., Larkin J., and Alexander M., *Terahertz optical rectification from <110> zinc-blende crystals.* Appl. Phys. Lett., 1994. **64**: p. 1324.

10. Zhang X.C., and Auston D.H., *Optoelectronic measurement of semiconductor surfaces and interfaces with femtosecond optics.* Journal of Applied Physics, 1992. **71**(1): p. 326.

11. Grischkowsky D., S.K., Van Exter M., and Fattinger Ch., *Far-infrared time-domain spectroscopy with terahertz beams of dielectrics and semiconductors.* J. Opt. Soc. Am. B, 1990. **7**: p. 2006-2015.

12. Tsen K.-T., *Ultrafast Dynamical Process in Semiconductors.* Springer 2004. **Topics in Applied Physics**

13. Zhao G., Schouten R.N., Van der Valk N., Wenckebach W. Th., and Planken P.C.M., *Design and performance of a THz emission and detection setup based on a semi-insulating GaAs emitter.* Review of Scientific Instruments, 2002. **73**(4): p. 1715.

14. Pickwell E., and Wallace V.P., *Biomedical applications of terahertz technology.* Journal of Physics D: Applied Physics, 2006. **39**(17): p. R301-R310.

15. Zhang X.C., and Xu J., *Introduction to THz Wave Photonics.* Springer Science and Business Media, 2010.

16. Uhd Jepsen P., Jacobsen R.H., and Keiding S.R., *Generation and detection of terahertz pulses from biased semiconductor antennas.* J. Opt. Soc. Am. B, 1996. **13**: p. 2424-2436.

17. Williams C.R., *Terahertz waveguiding on Metamaterials.* PhD Thesis. University of Bath, August 2009.

18. Huggard P.G., Shaw C.J., Cluff J.A., and Andrews S.R., *Polarization-dependent efficiency of photoconducting THz transmitters and receivers.* Applied Physics Letters, 1998. **72**: p. 2069.

19. Hussain A, and Andrews S.R., *Ultrabroadband polarization analysis of terahertz pulses.* Optics Express, 2008. **16**: p. 7251.

20. Wu Q., and Zhang X.C., *Free-space electro-optic sampling of terahertz beams.* Applied Physics Letters, 1995. **67**(24): p. 3523.

21. Smith P.R., Auston D.H., and Nuss M.C., *Subpicosecond photoconducting dipole antennas.* Quantum electronics, 1988. **24**(2): p. 255-260.

22. Grischkowsky D., and Van Exter M., *Characterization of Optoelectronic Terahertz Beam System.* IEEE transactions on microwave theory and techniques, 1990. **38,** (11): p. 1684-1691.

23. Cai Y., Brener I., Lopata J., Wynn J., Pfeiffer L., Stark J.B., Wu Q., Zhang X.C., and Federici J.F., *Coherent terahertz radiation detection: Direct comparaison between free-space electro-optic sampling and antenna detection.* Appl. Phys. Lett., 1998. **73**(4): p. 444-446.

24. Sun F.G., Wagoner G.A., and Zhang X.C., *Measurement of free-space terahertz pulses via long-lifetime photoconductors.* Applied Physics Letters, 1995. **67**(12): p. 1656.

25. Tani M., Lee K.-S., and Zhang X.C., *Detection of terahertz radiation with low-temperature-grown GaAs-based photoconductive antenna using 1.55 μm probe.* Applied Physics Letters, 2000. **77**(9): p. 1396.

26. Liu T.-A., Tani M., Nakajima M., Hangyo M., Sakari K., Nakashima S., and Pan C.-L., *Ultrabroadband terahertz field detection by photoconductive antennas based on multi-energy arsenic-ion-implanted GaAs and semi-insulating GaAs.* Applied Physics Letters, 2003. **83**(7): p. 1322.

27. Peter F., Winnerl S., Nitsche S., Dreyhaupt A., Schneider H., and Helm M., *Coherent terahertz detection with a large-area photoconductive antenna.* Applied Physics Letters, 2007. **91**(8): p. 081109.

28. Hu B.B., and Nuss M.C., *Imaging with terahertz waves.* Optics Letters, 1995. **20**(16): p. 1716-1718.

29. Auston D.H., Cheung K.P, and Smith P.R., *Picosecond photoconducting Hertzian dipoles.* Applied Physics Letters, 1984. **45**(3): p. 284.

30. Brener, I. Dykaar D., Frommer A., Pfeiffer L.N., Lopata J., Wynn J., West K., and Nuss M.C., *Terahertz emission from electric field singularities in biased semiconductors.* Optics Letters, 1996. **23**: p. 1924-1926.

31. Y. Cai, Brener I., Lopata J., Wynn J., Pfeiffer L., and Federici J.F., *Design and performance of singular electric field terahertz photoconducting antennas.* Appl. Phys. Lett., 1997. **71**: p. 2076-2078.

32. Zeng Y., Kreouzis T., Chen X., and Donnan R., *Efficiency and Spectrum Evaluation of Terahertz Photoconductive Antenna Array Based on GaAs Substrates.* IEEE, 2014: p. 1-2.

33. Hirota Y., Hattori R., Tani M., and Hangyo M., *Polarisation modulation of terahertz electromagnetic radiation by four-contact photoconductive antenna.* Optics Express, 2006. **14**: p. 4486.

34. Makabe H., Hirota Y., Tani M., and Hangyo M., *Polarization state measurement of terahertz electromagnetic radiation by three-contact photoconductive antenna.* OPTICS EXPRESS, 2007. **15**: p. 11650.

35. Pozar David M., *Microwave engineering.* New York Chichester, 2004, Wiley.

Chapter 3

Terahertz Polarisers

3.1 Introduction

Systems measuring the polarisation states of electromagnetic waves were first developed for the visible and the near-IR region and very high performance devices capable of defining or analysing (polarisers) or converting (waveplates) polarisation states are available. In these regions of the spectrum, there are three popular and most used polarisers, polarising prisms (e.g. Glan-Taylor) which depend on the use of birefringent materials, anisotropic absorbers and multilayer reflective coatings which work near Brewster's angle. Such sophisticated components been developed for use at THz frequencies too.

Due to the recent development of terahertz technology and the increasing use of polarisation resolving terahertz time-domain spectroscopy, demands for high quality and low cost terahertz polarisation components are increasing. Characterisation of the polarisation of a terahertz wave requires precise determination of the magnitude and the direction of orthogonal electric field components. For this purpose, several devices have been developed such as semiconductor photoconductive antenna devices with two or three gaps that have different polarization sensitivities [1-5], electro-optic (EO) sampling, which has a terahertz E-field sensitivity that depends on the relative direction between the crystal axes and the polarization direction of the terahertz waves [6-8], and linear polarisers [9-11].

The most fundamental devices used for measuring the polarisation state of terahertz waves are linear polarisers. These polarisers are divided into two categories; pile-of-plates polarizers and wire-grid-polarizers [12, 13]. The first relies on different reflectivity of *s* and *p* polarised light incident on a dielectric surface at Brewster's angle and the second on the anisotropic conductivity of thin metal wires.

In this chapter, experimental and computational studies of four different linear polarisers are presented. The first polariser is a home-made pile-of-plates device and the others are based on wire-grids constructed using different methods and of different dimensions and substrates.

3.2 Pile-of-Plates polariser

The geometrical considerations for silver chloride (AgCl) 'pile-of-plates' polarisers were considered long ago by Bird and Shurcliff (1959) using a pile of 'thick' plates to cover the usual infrared region, Conn and Easton (1954) used a pile of very thin (about 3 μm) Selenium, for which interference effects dominate [14]. Pile-of-plates polariser composed of thin plates of polyethylene was also fabricated targeting the THz region [15]. Recently, a pile-of-plates polariser made of four silicon wafers was fabricated by Wojdyla and Gallot [16]. These polarisers use the fact that there is almost total transmission of the *p*-polarised (parallel to incident radiation) component of light at Brewster's angle and partial reflection of *s*-polarised (perpendicular to the incident radiation) light. Brewster's angle is given by

$$\theta_B = \arctan(n), \tag{1}$$

where n is the refractive index of the substrate used. In this work, our pile-of-plates polariser are based on silicon for which n=3.42 at 1THz, giving a value of θ_B = 73.7°. In a multiple plate polariser the *p*-plane transmission is essentially the single-surface transmission raised to the power of the number of surfaces, since multiple reflection effects are negligible. The *s* intensity reflectivity of a single of surface is given by the Fresnel formula [14]

$$r_s = \left(\frac{\sin(\theta_B - \theta_t)}{\sin(\theta_B + \theta_t)} \right)^2, \tag{2}$$

where θ_t is the internal propagation angle in the plane such that

$$\theta_t = \arcsin\left(\frac{\sin\theta_B}{n} \right) \tag{3}$$

The *s*-plane transmission of a single plate is

$$t_s = (1 - r_s)^2. \tag{4}$$

In our THz-TDS system, a pair of high resistivity silicon "pile-of-plates" polarisers [14] is used in series in such a way to leave the beam path unaltered by their insertion. This pair of polarisers was placed after the THz transmitter in order to reduce the orthogonal field radiation due to some quadrupolar emission from the emitter and the changes in polarization on reflection at the 90^{o} off-axis parabolic mirror in front of the transmitter [5].

Each of the pair of "pile of plates" polarisers consists of a stack of five identical high resistivity (50 kΩcm) 500μm thick optically polished silicon wafers. The plates are roughly 100 mm x 30 mm in size and each plate is spaced from its neighbours by 650 μm. The silicon plates are oriented close to Brewster's angle in the THz beam and the effective 'end on' aperture is 16 mm x 25 mm. The measured THz beam diameter has a maximum value of 15 mm (1/e amplitude) in the region occupied by the polarisers. The polarisers are used in series in such a way as to leave the beam path unaltered by their insertion. To minimise a possible reduction in performance due to slight relative misalignment of the rotation axes of the two polarisers, we have used a tilting mechanism as shown in figure 3.1. By substituting the parameters of our pile-of-plates polarizer in equation (4), we calculate a *s*-plane transmission of $t_s = 4x10^{-6}$ and a *p*-plane reflection of $t_p = 1$.

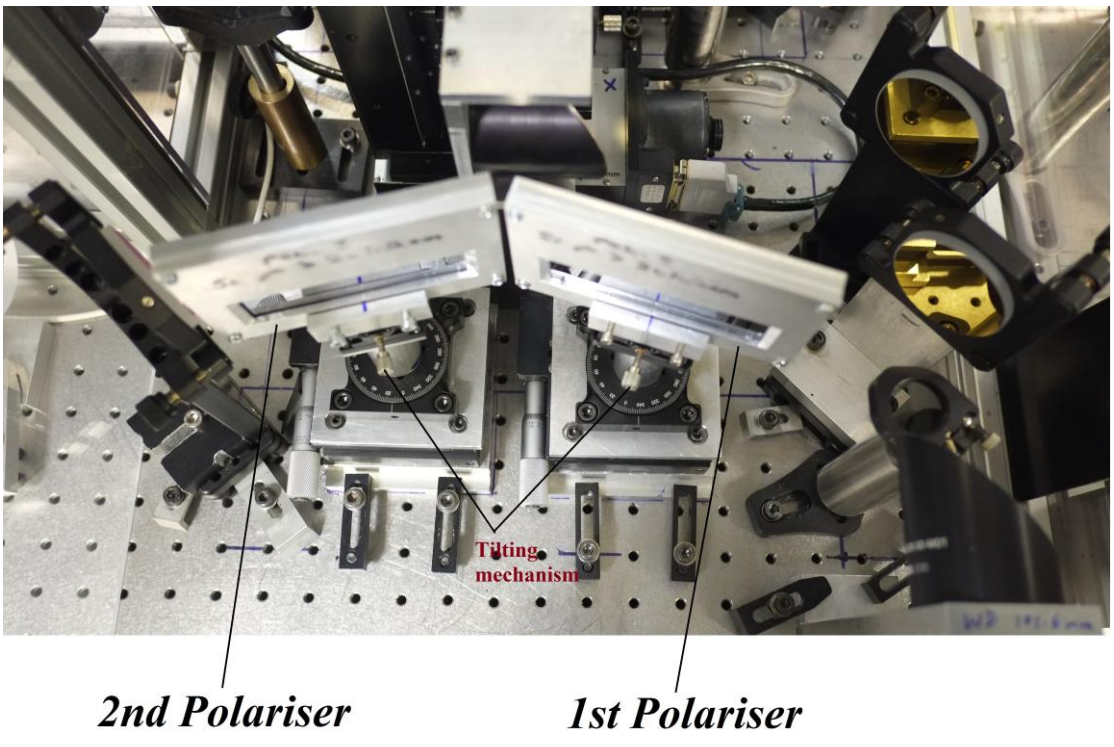

Fig 3.1: Photograph of pair of 'pile-of-plates' polarisers each consisting of five silicon plates, in a zero beam displacement geometry

To determine the polarization purity of our pile-of-plates polariser, we measured the orthogonal and the parallel electric fields for parallel and crossed polarisers. Figure 3.2 shows the time traces of the electric field components polarised along the *x* and the *y*-axes as well as their spectra.

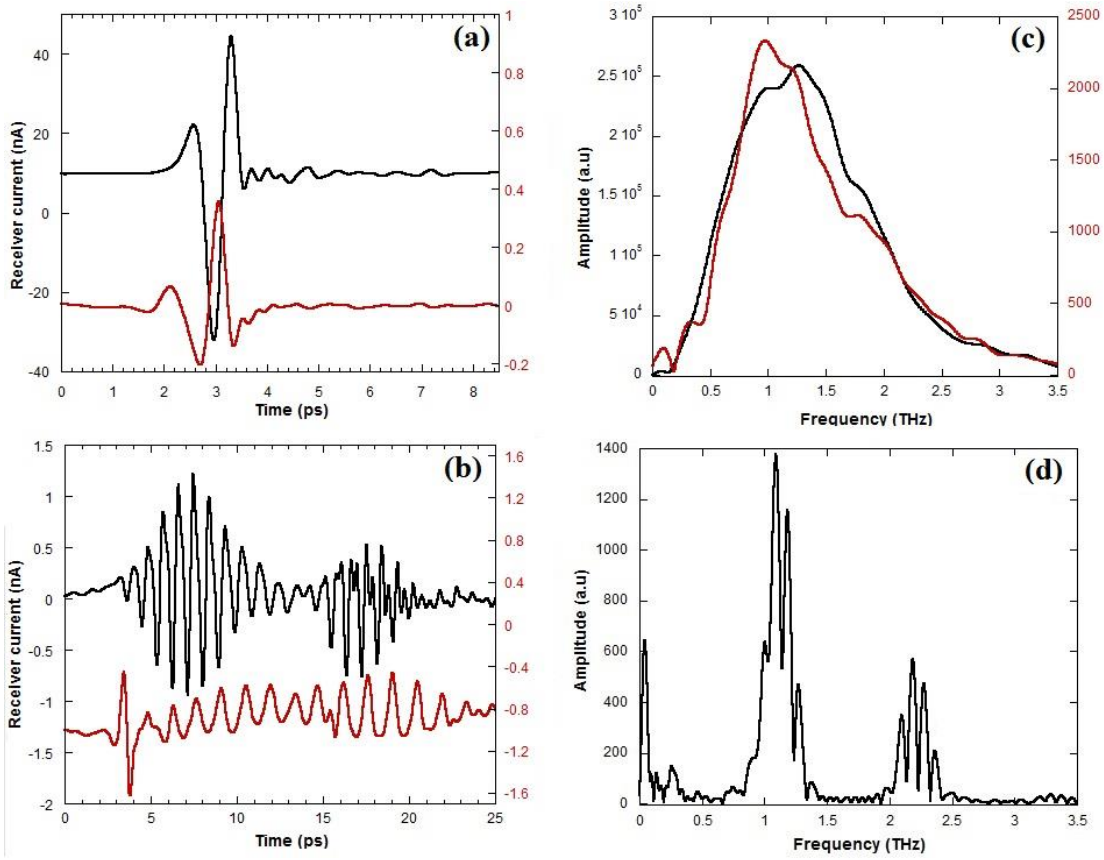

Fig 3.2: (a) and (b) Time domain THz signals after transmission through a pair of pile-of-plates polarisers set respectively parallel and perpendicular to each other. (black) measured electric field component polarised parallel to the incident polarisation along x-axis, (red) measured electric field component polarised along y-axis. (c) are the x and y-polarised spectra when the pair of polarisers are set parallel to each other. (d) the x-polarised spectra when the pair of polarisers are set perpendicular to each other.

The time-domain traces in figure 3.2 (a), when the pair of polarisers are set parallel to each other, display a peak to peak receiver currents of ~ 80 nA and 0.4 nA along the *x* and *y* axes respectively. The corresponding *x* and *y*-polarised spectra in figure 3.2 (c) show a detection bandwidth at 10% fall-off the amplitude of ~3 THz for both polarisations. When the polarisers are set perpendicular to each other the *p* and *s*-polarised signals show pronounced resonances and a peak to peak of the receiver currents of ~0.06 nA for polarisation along the *x*-axis and ~0.118 nA along the *y*-axis. The same resonances are also shown in figure 3.2 (d) of the spectra corresponding to the measured electric field

component polarised along the *x*-axis. These resonances are Fabry-Perot resonances associated with the 650 μm thick air cavities between the silicon plates in the polariser which have been rotated to give strong reflectivity. Figure 3.2 (d) shows also that the Fabry-Perot resonances are important in the frequency region between 0.9 THz and 1.3 THz and the frequency region between 2 THz and 2.3 THz which means that the polarisation is these regions is not perfect and it should be considered in our measurements.

From the results shown in figure 3.2 (a) and (b) of the transmitted terahertz waves through the polarisers, the calculated field extinction is around 0.0025±.00002, near 1 THz, which is in good agreement with the theoretical prediction of 0.004 of a single pile-of-plates polariser. This field extinction corresponds to an intensity extinction ratio of $4x10^{-6}$ for a single polariser which is very comparable with the best commercially available Glan type calcite polarisers in the visible. The calculated intensity extinction for a perfectly aligned pair of 'pile-of-plates' polarisers is $2x10^{-11}$. The amplitude transmission of our pair of 'pile-of-plates' polarisers for p-polarised radiation is about 90% due probably to the size of plates which are smaller than ideal. This transmitted field is pure to a few parts in 10^6 taking into account the *s*-polarised input field of about 10% due to some quadrupolar emission from the source and a slight depolarisation in the transmitter collection optics.

3.3 Wire-grid polarisers

We have used wire-grid polarisers both as simple polarisers and as polarising beam splitters which split the incident light beam into two orthogonal polarised beams, which may or may not have the same optical power. Different types of polarising beam splitters exist and are used for different purposes, for examples in interferometers and laser systems. Free standing wire-grid polarisers which are based on arrays of equidistant aligned parallel tungsten wires either free standing or on a substrate [17], are the most used polarisers in the terahertz frequency region. The principle of these polarisers is as follow, when an unpolarised electromagnetic wave is incident on the grids, free electrons are generated along the wires. If the electric field is polarised parallel to the wires, the electrons move along the wire direction and the polariser behaves as a typical metal surface, thus most of the incident radiation is reflected. On the other hand, if the electric field is polarised perpendicular to the wires, the electromagnetic wave does not see the wires and passes through the polariser as the free electrons movement in the direction perpendicular to the grids are highly restricted. In general, when the terahertz wave is incident on the polariser, the component polarised parallel T_p to the wire is reflected and that polarized orthogonal T_s to the grid is transmitted. Because of the difficulty in aligning the wires precisely parallel to each other in wire-grid polarisers and the relatively low conductivity of the high tensile strength metal that must be used (typically tungsten), these polarisers present a poor extinction ratios of ~ 30 dB for the best commercial free-standing metal wire-grid polariser with 5 μm diameter tungsten metal

wires on a frame at approximately 12.5 µm period intervals. The extinction ratio of a wire-grid polariser is the ratio between the transmittance of the orthogonal component and the transmittance of the parallel component (T_s/T_p) which is inversely proportional to the frequency and the pitch of the wires [18]. This means that we can improve the extinction ratio of the wire-grid polariser at high frequencies by decreasing the pitch.

In this section, three wire-grid polarisers with different designs were compared for use as THz polarising beam splitters. It should be noted that in this work, the study of our wire-grid polarisers is performed when the polarisers are set at normal incidence which is different from their normal use at 45°. When the polariser is set at 45°, the main difference is that the effective wire spaces are smaller so that higher extinction might be expected. However this assumes that the substrate is completely flat. The first wire-grid polariser is comprises on free standing tungsten wires of 5 µm diameter and a period of 12.5 µm. Figure 3.3 shows the signal waveform of the measured incident and transmitted THz pulse through the tungsten wire-grid polariser set as the grating oriented parallel to the electric field of the incident radiation.

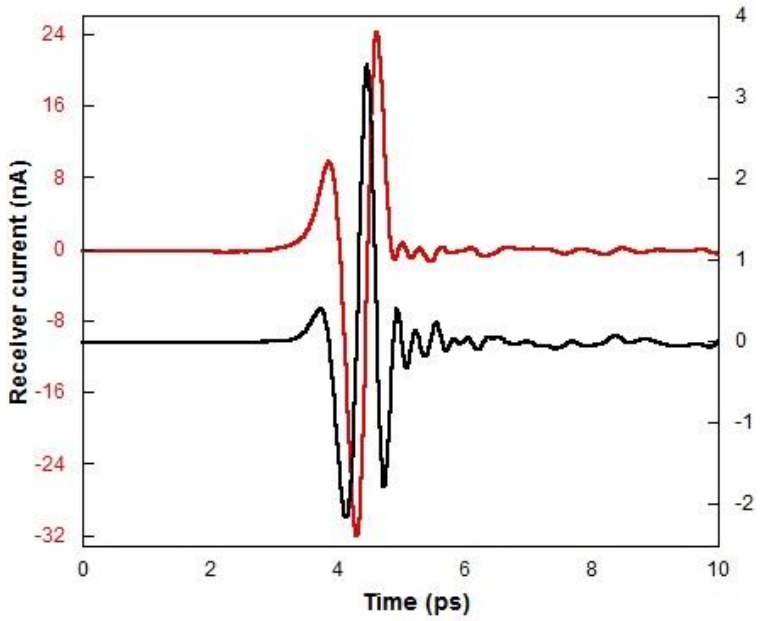

Fig 3.3: The signal waveform of (red) the incident pulse and (black) the measured transmitted electric pulse through the Tungsten wire-grid polariser (12.5 µm period) for a parallel orientation of grating lines with respect to the electric field of the incident light.

Figure 3.3 shows that the amplitude of the transmitted electric field measured when the grating lines of the tungsten wire-grid polariser are oriented parallel to the incident radiation is significantly reduced compared to the incident pulse. Moreover, it appears that this transmitted pulse arrives earlier than the incident pulse which corresponds to the measured transmitted pulse through a reference area that is not covered by metallic structures on the same polariser. A similar negative phase shift was reported for terahertz

pulses transmitted through metallic gratings and was explained by the fact that the signal is the first time-derivative of the incident pulse [13]. The properties of a transmitted pulse with polarisation parallel to the wires is related to two elements; the period of the grating *d* and the wavelength λ of the incident pulse. The transmitted electric field at a frequency ω for an electromagnetic wave polarised along the *x*-axis, is given by [13].

$$E_x^{tr}(t) = \frac{\omega l}{c}\frac{\partial}{\partial(\omega t)}E_x^{inc} - (\frac{\omega l}{c})^2\frac{\partial^2}{\partial(\omega t)^2}E_x^{inc} + ..., \quad (5)$$

where $l = (d \ln 2)/\pi$ and c is the speed of light and it is assumed that the wires are perfectly conducting and free-standing in air. Since the grating period for our tungsten wire-grid polariser is much smaller than the wavelength λ, $\omega l/c = (2d \ln 2)/\lambda << 1$. Thus means only the first term of equation (5) needs to be considered and the transmitted electric field is the first time derivative of the incident pulse. Figure 3.4 shows a comparison between the time-domain trace of the transmitted pulse and the calculated first derivative of the measured incident pulse. It is clear that there is a good agreement between the experimental data and the calculated first derivative.

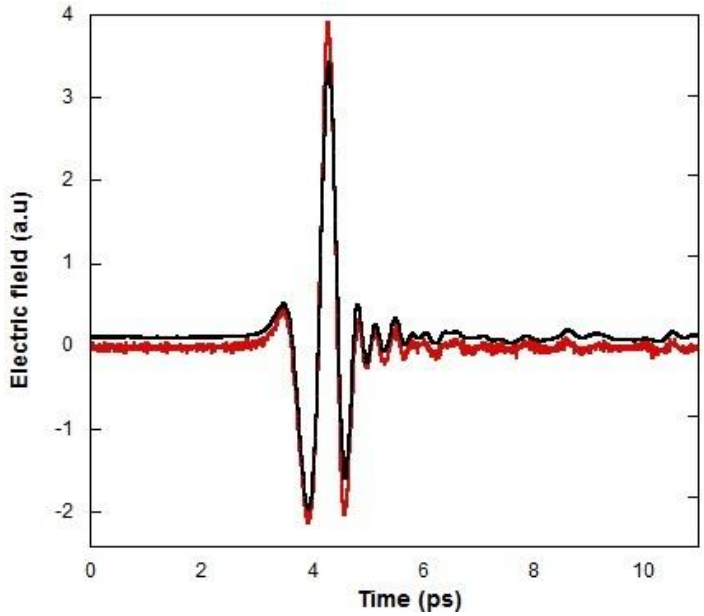

Fig 3.4: The terahertz signal waveform of (black) the measured transmitted electric field pulse through the Tungsten wire-grid polariser and (red) the calculated first derivative of the incident pulse.

The same experiments have been performed on the second wire-grid polariser which is a home-made device fabricated using standard photolithography and lift-off techniques. The polariser consists of a grating of 5 μm wide gold strips with 10 μm period over an area of 25 x 25 mm on a high resistivity silicon substrate. The strips of the wire-grid polariser were

aligned so that when the THz wave is incident on the wire-grid, nearly all the component polarised orthogonal to the grid is transmitted. Figure 3.5 shows the time traces of the incident and the transmitted THz pulse through the Au/Ti wire-grid polariser set as the grating oriented parallel to the electric field of the incident radiation as well as the time domain trace of the calculated first derivative of the incident pulse. Figure 3.5 shows that the Au/Ti wire-grid polariser exhibits the same characteristics as the tungsten wire polariser shown in figure 3.3 and 3.4.

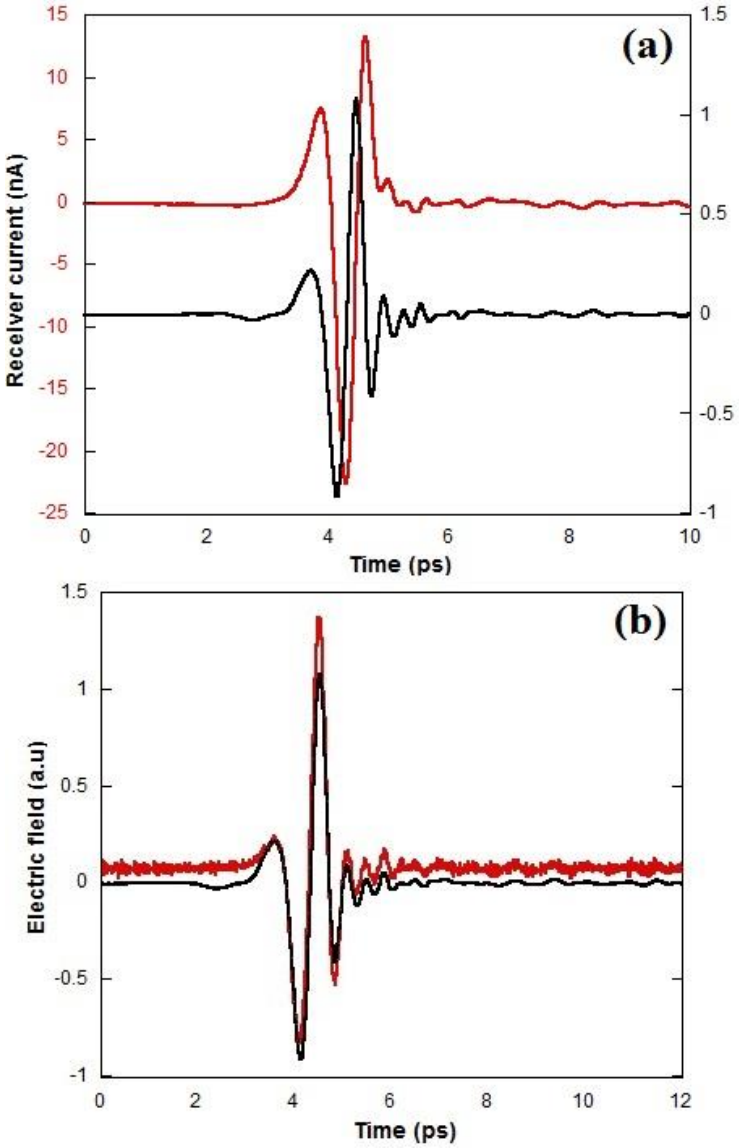

Fig 3.5: (a) The signal waveform of (red) the incident pulse and (black) the measured transmitted electric pulse through the Tungsten wire-grid polariser (10 µm period)for a parallel orientation of grating lines with respect to the electric field of the incident light. (b) The terahertz signal waveform of (black) the measured transmitted electric field pulse through the same wire-grid polariser and (red) the calculated first derivative of the incident pulse.

Most of the wire-grid polarisers were fabricated on substrates using photolithography technique. Recently, nanoimprinting lithography (NIL) has been developed for fabricating various planar nanosized patterns [19]. This nanoimprinting technique has a higher throughput than that of conventional photolithography, because molds repeatedly used are directly put into thermoset or UV-cured resin, which makes the regulation easer and the cost lower [12]. The third polariser uses is a wire-grid polariser fabricated on thin flexible triacetylcellulose (TAC) substrates using this nanoimprinting lithographic technique. The thin TAC film was coated with a thick light-curing resin of ~1 μm and then a nickel mold with negative pattern of the wire-grid was impressed onto this light-curing resin. The pattern of the mold was then transferred from the back side of the TAC film by UV exposure before the deposition of the aluminium layer. The wire-grid polariser was obtained from the Japanese company Asahi Kasei E-Materials and it consists of aluminium wires with a thickness d1=130 nm, a pitch p=140 nm and a filling factor D=0.4, deposited on an 80 μm thick triacetycellulose substrate [12]. Schematic and scanning electron microscope (SEM) image of the wire-grid polariser are shown in figure 3.6.

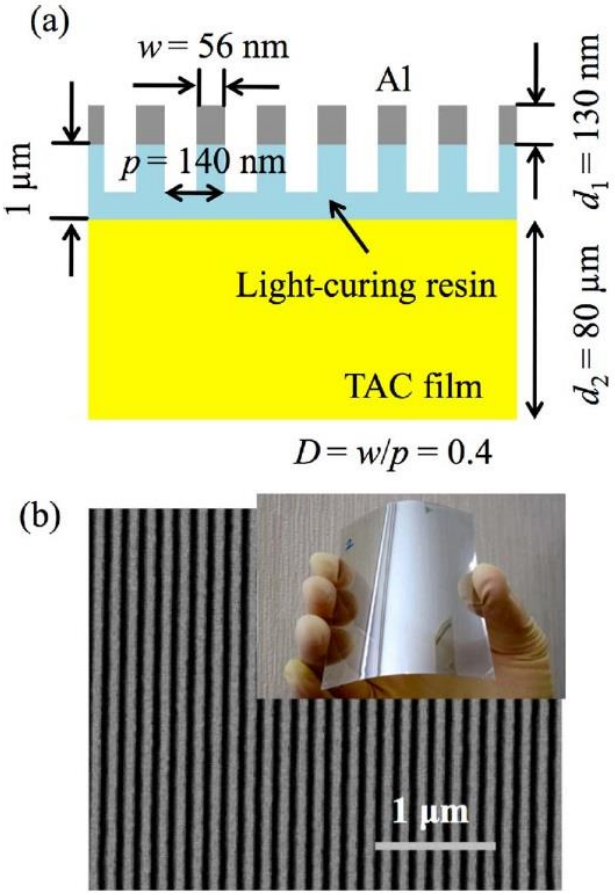

Fig 3.6: (a) Schematic and (b) SEM image of the nano-scale wire-grid polariser (140 nm period) fabricated on a triacetylcellulose film. Inset, photograph showing flexiblility of the polariser [12]

Figure 3.7 shows the time domain traces of the incident and the transmitted THz pulse through the nano-scale wire-grid polariser as well as the calculated first derivative of the incident radiation. It is clear from figure 3.7 (a) that the nano-scale wire polariser does not exhibit the same characteristics as the tungsten and the Au/Ti polarisers; both the transmitted and the incident pulse arrive in the same time, and the transmitted THz radiation does not correspond to the first derivative of the incident pulse which is evidently seen from the calculated first derivative of the incident pulse shown in figure 3.7 (b).

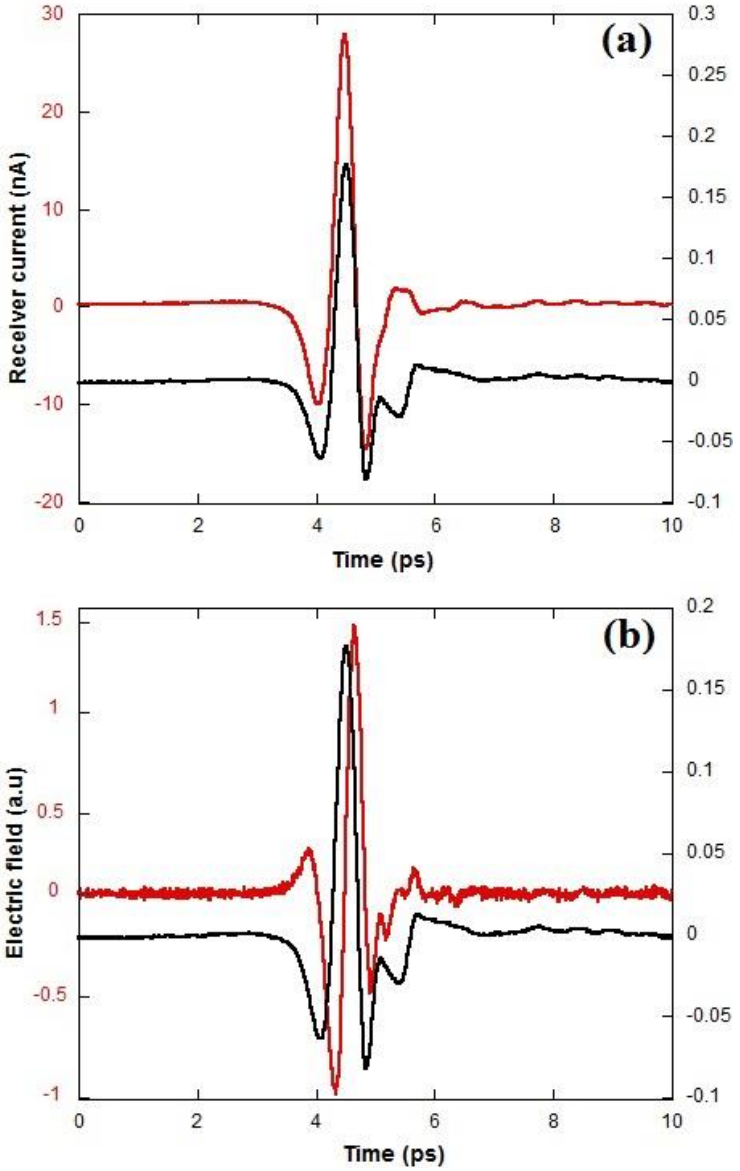

Fig 3.7: (a) The signal waveform of (red) the incident pulse and (black) the measured transmitted electric pulse through the nano-scale wire-grid polariser for a parallel orientation of grating lines with respect to the electric field of the incident light. (b) The time domain THz signal of (black) the measured transmitted electric field pulse through the same wire-grid polariser and (red) the calculated first derivative of the incident pulse.

The experimental and calculated extinction ratios of the three wire-grid polarisers are compared in figure 3.8 (a) and 3.8 (b). These extinction ratios were obtained by rationing the field spectrum for maximum and minimum transmission. The calculation of the extinction ratio was performed using the commercial finite element modelling package CST Microwave Studio. The optical response of the Al wires of the nano-scale polariser was described by the Drude model where the plasma angular frequency and the damping frequency of the metal are given respectively by ω_p=2.24 x 10^{16} rad/s and γ=1.24 x 10^{14} Hz [12]. Figure 3.8 shows the spectral response of the measured and the calculated extinction ratio of these three polarising beam splitters.

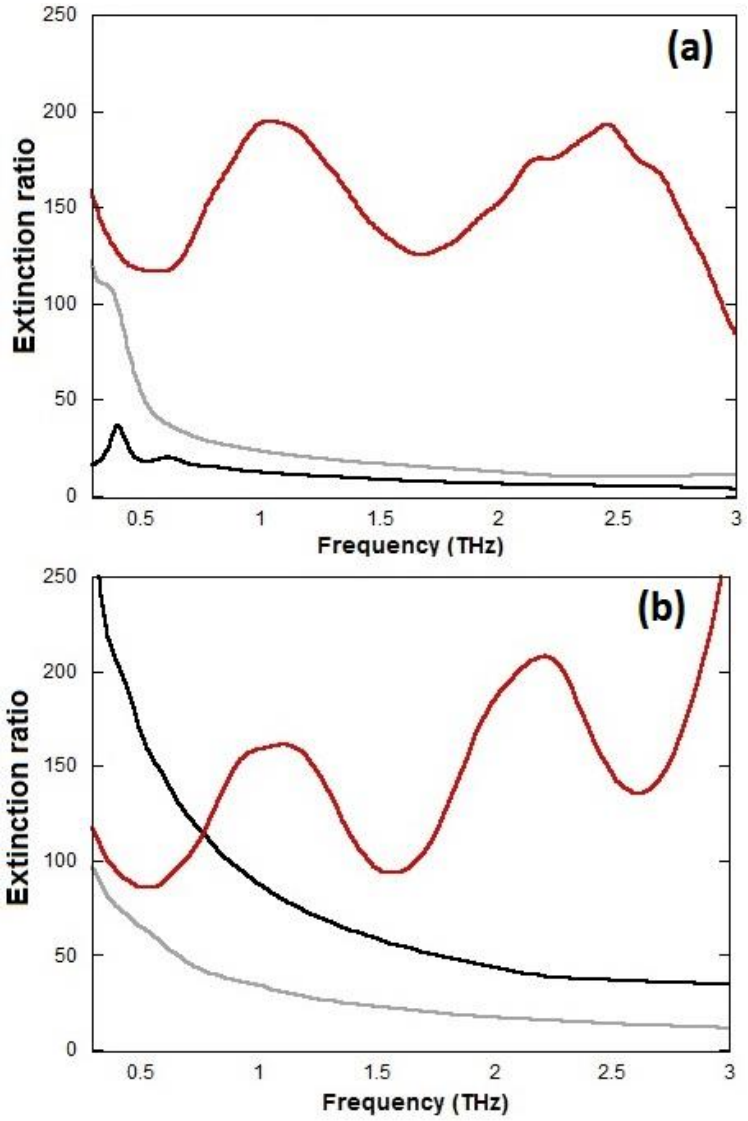

Fig 3.8: (a) and (b) are respectively the spectra of the measured and calculated extinction ratio of, (red) nano-scale wire-grid polariser (d=140 nm), (black) tungsten wire-grid polariser (d= 12.5 µm) and (gray) the Au/Ti wire-grid polariser (d= 10 µm).

Figures 3.8 (a) and (b) show an oscillation of the measured and the calculated extinction ratio of the wire-grid polarising beam splitter fabricated on the TAC film with nanoimprint techniques. This oscillation is due to the Fabry-Perot interference in the TAC substrate [12] which can be reduced by using a thinner substrate. Moreover it appears an increase in the measured extinction ratio of this wire-grid polariser above 2.8 THz caused by the limited sensitivity of the detection in our THz-TDS system. Figure 3.8 shows a good agreement between the measured and the calculated extinction ratio of the homemade Au wire-grid polariser unlike the commercial Tungsten wire-grid polariser. The disagreement between the experimental and the theoretical results of this latter commercial polariser is due to the poor parallelism of the wires which is apparent under an optical microscope.

3.1 Summary

For the polarisation measurement of terahertz radiation, we have developed a pair of high efficiency 'pile-of-plates' polarisers which are placed after the source and collection optics to eliminate the orthogonal polarisation due to the change in polarisation on reflection at OAPMs and some quadrupolar emission from the transmitter. The experimental studies of a single polariser showed an excellent agreement with the theoretical prediction a value of the extinction ratio of $4x10^{-6}$ which is very comparable with the best commercially available in the visible. And the calculated value of this extinction ratio for a perfectly aligned pair of 'pile-of-plates' polarisers was $2x10^{-11}$.

We have also studied and compared three polarisers which consist of wire-grid polarisers with different designs. These polarisers are used as beam splitters to separate the large *p*-polarised field component from the generally very much smaller *s*-polarised component induced by any optical activity in a sample. The experimental and theoretical results have shown an excellent extinction ratio (less than 10^{-4} below 2 THz) for the nano-scale wire-grid polariser fabricated on a thin flexible substrate (triacetycellulose) using a nanoimprint technique which makes this beam splitter the best choice for the characterisation of polarisation.

References

1. Castro-Camus E., *Polarization-Resolved Terahertz Time-Domain Spectroscopy.* Journal of Infrared Millimeter and Terahertz Waves, 2012. **33**: p. 418-430.

2. Castro-Camus E., Lloyd-Hughes J., Johnston M. B., Fraser M.D., Tan H.H., and Jagadish C., *Polarization-sensitive terahertz detection by multicontact photoconductive receivers.* Applied Physics Letters, 2005. **86**(25): p. 254102.

3. Tani M., Hirota Y., Que Christopher T., Tanaka S., Hattori R., Yamaguchi M., Nishizawa S., and Hangyo M., *Novel Terahertz Photoconductive Antennas.* International Journal of Infrared and Millimeter Waves, 2006. **27**(4): p. 531-546.

4. Hiroyuki M., Hirota Y., Tani M., and Hangyo M., *Polarization state measurement of terahertz electromagnetic radiation by three-contact photoconductive antenna.* OPTICS EXPRESS, 2007. **15**: p. 11650.

5. Hussain A., and Andrews S.R., *Ultrabroadband polarization analysis of terahertz pulses.* OPTICS EXPRESS, 2008. **16**: p. 7251.

6. PLanken Paul C.M., Nienhuys H.-K., Bakker H.J., and Wenckebach T., *Measurement and calculation of the orientation dependence of terahertz pulse detection in ZnTe.* J. Opt. Soc. Am. B, 2001. **18**: p. 313-317.

7. Van der Valk Nick C.J., Van der Marel Willemine A.M.,and Planken Paul C. M., *Terahertz polarisation imaging.* Optics Letters, 2005. **30**: p. 2802-2804.

8. Zhang L.L., Zhong H., Deng C., Zhang C.L., and Zhao Y.J., *Terahertz polarization imaging with birefringent materials.* Optics Communications, 2010. **283**(24): p. 4993-4995.

9. Dong H., Gong Y., Paulose V., and Hong M., *Polarization state and Mueller matrix measurements in terahertz-time domain spectroscopy.* Optics Communications, 2009. **282**(18): p. 3671-3675.

10. Dong H., Gong Y., and Olivo M., *Measurement of Stokes parameters of terahertz radiation in terahertz time-domain spectroscopy.* Microwave and Optical Technology Letters, 2010. **52**(10): p. 2319-2324.

11. Yandong G., Hui D., and Paulose V., *Simple methods to measure partial polarization parameters in the Terahertz band using THz-TDS.* Microwave and Optical Technology Letters, 2010. **52**(9): p. 2005-2007.

12. Takano K., Yokoyama H., Ichii A., Morimoto I., and Hangyo M., *Wire-grid polarizer sheet in the terahertz region fabricated by nanoimprint technology.* Optics Letters, 2011. **36**(14): p. 2665-2667.

13. Filin A., Stowe M., and Kersting R., *Time-domain differentiation of terahertz pulses.* Optics Letters, 2001. **26**: p. 2008-2010.

14. Rutt H.N., *A low-cost, ultra-wide-range infrared polarizer.* Meas. Sci. Technol., 1995. **6**: p. 1124-1132.

15. Mitsuishi A., Yamada Y., Fujita S., and Yoshinaga H., *Polarizer for the far-infrared region.* Optical Society of America, 1960. **50**: p. 433-436.

16. Wojdyla A., and Gallot G., *Brewster's angle silicon wafer terahertz linear polarizer.* OPTICS EXPRESS, 2011. **19**: p. 14099.

17. Mok C.L., Chambers W.G., Parker T.J., and Costley A.E., *The far-infrared performance and application of free-standing grids wound from 5um diameter tungsten wire.* Infrared Physics, 1979. **19**: p. 437-442.

18. Nagashima T., Tani M., and Hangyo M., *Polarization-sensitive THz-TDS and its Application to Anisotropy Sensing.* Journal of Infrared, Millimeter, and Terahertz Waves, 2013. **34**(11): p. 740-775.

19. Chou S.Y, Krauss P.R., and Renstrom P.J., *Nanoimprint lithography.* Vac. Sci. technol. B, 1996. **14**: p. 4129-4133.

Chapter 4

Polarisation resolved THz Spectroscopy

4.1 Introduction

In order to perform polarisation resolved THz-TDS and thus circular dichroism (CD) and optical rotational dispersion (ORD) measurements, it is necessary to be able to measure the amplitude and the phase of orthogonal field components the terahertz radiation. The measurements can be performed using either electro-optic (EO) detection or a conventional photoconductive (PC) receiver [1-3] as discussed in chapter 2. In both cases it is necessary to either rotate the electro-optic crystal [4] or the photoconductive antenna or to use two separate detectors and a polarising beam splitter [5, 6]. In all of these cases there is a possible phase error due to misalignment. In order to avoid this, various developments of photoconductive receivers to enable the measurements of both orthogonal components of the THz electric field simultaneously were proposed [7-9]. Unfortunately, as we have reported in chapter 2 section 2.5, these multi-contact photoconductive receivers have a significant cross-polarization component, which limits their sensitivity to small changes in polarisation, as reported also in other research [10, 11]. In this work we have chosen to use two separate photoconductive receivers because it appears possible to achieve the greatest sensitivity in this apparatus.

In this chapter we first describe how the parameters describing optical activity can be obtained from measurements of orthogonal field components and then give details of polarisation resolving spectrometer which continues the system described in chapter 2 with the elements described in chapter 3.

4.2 Formalism for describing optical activity

The electric field incident or/and transmitted by a material can be decomposed into left-handed E_L and right-handed E_R circularly polarized components. There are determined from the linear polarized field components via the relations

$$E_L = \frac{1}{\sqrt{2}}\left[E_{//}(t) + iE_{\perp}(t)\right], \tag{1}$$

and

$$E_R = \frac{1}{\sqrt{2}}\left[E_{//}(t) - iE_{\perp}(t)\right], \tag{2}$$

where $E_{//}$ is the field component parallel to the *x*-axis (horizontal in experiments) and $E_{\perp}$ the field component parallel to the *y*-axis (vertical in experiments). Equations (1) and (2) are valid when the time dependence of the wave is of the form $e^{i\omega t}$. For waves of the form $e^{-i\omega t}$, the signs for $iE_{\perp}(t)$ in equation (1) and (2) are reversed.

Information concerning liquids or solids containing chiral structures can be obtained from measurement of their optical activity. This optical activity of a chiral sample is generally characterised by its optical rotatory dispersion (ORD) and circular dichroism (CD). Optical rotatory dispersion describes the circular birefringence and rotation of the polarisation plane of linearly polarised light as it passes through the medium. Circular dichroism is the differential absorption of left-hand and right-hand circularly polarised light. The linear electric field transmitted by a material can be related to the incident field via a 2 x 2 Jones matrix $T(\omega)$, as follow [12]:

$$\underline{E^{out}}(\omega) = \underline{\underline{T}}(\omega)\underline{E^{in}}(\omega) \qquad \text{(a)}$$

, (3)

$$\begin{pmatrix} E^{out}{}_{//} \\ E^{out}{}_{\perp} \end{pmatrix} = \begin{pmatrix} t_{xx} & t_{xy} \\ t_{yx} & t_{yy} \end{pmatrix} \begin{pmatrix} E^{in}_{//} \\ E^{in}_{\perp} \end{pmatrix}, \qquad \text{(b)}$$

where t_{ij} are amplitude transmission coefficients. If a material has rotational symmetry, for example three or four-folder symmetry about the *z*-axis, the transmission matrix becomes

$$T(\omega) = \begin{pmatrix} t_{xx} & t_{xy} \\ -t_{xy} & t_{xx} \end{pmatrix}. \tag{4}$$

Similarly, when the linearly polarised light is propagating through a medium containing chiral structures, a difference between left-hand and right-hand circularly polarised light is occurred. The incident and transmitted left and right hand circularly polarised fields can be related by a different Jones matrix T_c as follow [12]:

$$\begin{pmatrix} E_L^{out}(\omega) \\ E_R^{out}(\omega) \end{pmatrix} = \underline{\underline{T_c}}(\omega) \begin{pmatrix} E_L^{in}(\omega) \\ E_R^{in}(\omega) \end{pmatrix} \quad \text{(a)}$$

,

$$\begin{pmatrix} E_L^{out} \\ E_R^{out} \end{pmatrix} = \frac{1}{2} \begin{pmatrix} t_{rr} & t_{rl} \\ t_{lr} & t_{ll} \end{pmatrix} \begin{pmatrix} E_L^{in} \\ E_R^{in} \end{pmatrix} \quad \text{(b)} \qquad (5)$$

,

$$\begin{pmatrix} E_L^{out} \\ E_R^{out} \end{pmatrix} = \frac{1}{2} \begin{pmatrix} t_{xx} + t_{yy} + i(t_{xy} - t_{yx}) & t_{xx} - t_{yy} - i(t_{xy} + t_{yx}) \\ t_{xx} - t_{yy} + i(t_{xy} + t_{yx}) & t_{xx} + t_{yy} - i(t_{xy} - t_{yx}) \end{pmatrix} \begin{pmatrix} E_L^{in} \\ E_R^{in} \end{pmatrix} \quad \text{(c)}$$

For circular birefringence, equation 5(c) shows that t_{xy} and t_{yx} are different. If they are equal, then we only have linear birefringence.

The optical activity of a chiral material is characterised by the polarisation azimuth rotation angle θ, and the ellipticity γ [13] which are defined respectively by

$$\theta = \frac{1}{2}\left[Arg(t_{rr}) - Arg(t_{ll})\right] \quad \text{(a)}$$

, (6)

$$\gamma = \frac{1}{2}\arctan\left(\frac{|t_{rr}|^2 - |t_{ll}|^2}{|t_{rr}|^2 + |t_{ll}|^2}\right) \approx \frac{|t_{rr}| - |t_{ll}|}{|t_{rr}| + |t_{ll}|} \quad \text{(b)}$$

It is clear from equations 6 (a) and 6 (b) that optical activity requires $t_{rr} \neq t_{ll}$ and therefore also $t_{xy} \neq t_{yx}$.Artificial chiral materials with large rotation angle and small ellipticity are important for application such as negative index metamaterials.

When circularly polarised light passes through a medium containing chiral structures, left-hand and right-hand polarised light are phase shifted because they "see" two different refractive indices, n_L and n_R. The difference in these two refractive indices is called optical rotatory dispersion and it results in a rotation of the plane of the linear polarised light. The spectrum of the optical rotational dispersion ($\Delta n = n_L - n_R$) is calculated from the equation of the rotation angle by

$$\Delta n(\omega) = \frac{\theta(\omega)c}{\omega L}, \qquad (7)$$

where L is the length of the material, c is the speed of the light and ω is the angular frequency. Left and right hand circularly polarised light can also be absorbed to a different extent; that is, $\alpha_L \neq \alpha_R$. The difference in the absorption $\Delta\alpha = \alpha_L - \alpha_R$ is called circular dichroism and it is calculated from the Jones matrix by

$$\Delta\alpha = \frac{2}{L}\ln\left[\frac{t_{rr}}{t_{ll}}\right] \tag{8}$$

The spectra of the circular dichroism and the optical rotational dispersion are related to the optical activity susceptibility $\Delta\chi = \chi_L - \chi_R$ called also the complex chiral susceptibility. For a material with rotational symmetry about z (propagation axis), $\Delta\chi$ is calculated from the Jones matrix by the following relationship

$$\Delta\chi = \frac{4cn}{\omega L}\left(\frac{\tilde{E}_{\perp}}{\tilde{E}_{//}}\right) = \frac{4cn}{\omega L}\left(\frac{\tilde{t}_{xy}}{\tilde{t}_{xx}}\right), \tag{9}$$

and the optical rotational dispersion (ORD) and the circular dichroism (CD) are given respectively by

$$\Delta n = \frac{1}{2n}\mathrm{Re}\{\Delta\chi\} \quad \text{(a)}$$
$$, \tag{10}$$
$$\Delta\alpha = \frac{\omega}{cn}\mathrm{Im}\{\Delta\chi\} \quad \text{(b)}$$

The circular dichroism and the optical rotational dispersion can thus be calculated from the transmitted electric field components respectively by,

$$\Delta n = \frac{2c}{\omega L}\mathrm{Re}\left(\frac{E_{\perp}}{E_{//}}\right) \quad \text{(a)}$$
$$, \tag{11}$$
$$\Delta\alpha = \frac{4}{L}\mathrm{Im}\left(\frac{E_{\perp}}{E_{//}}\right) \quad \text{(b)}$$

4.4 Polarisation resolving spectrometer

Figure 4.1 shows a schematic diagram of the polarization-sensitive THz time-domain spectroscopy setup. The setup is essentially the same as described in chapter 2 but with the addition of some components to allow sensitive polarisation analysis. The design of the THz transmitter and photoconductive receiver antennas are identical to those previously described in chapter 2.

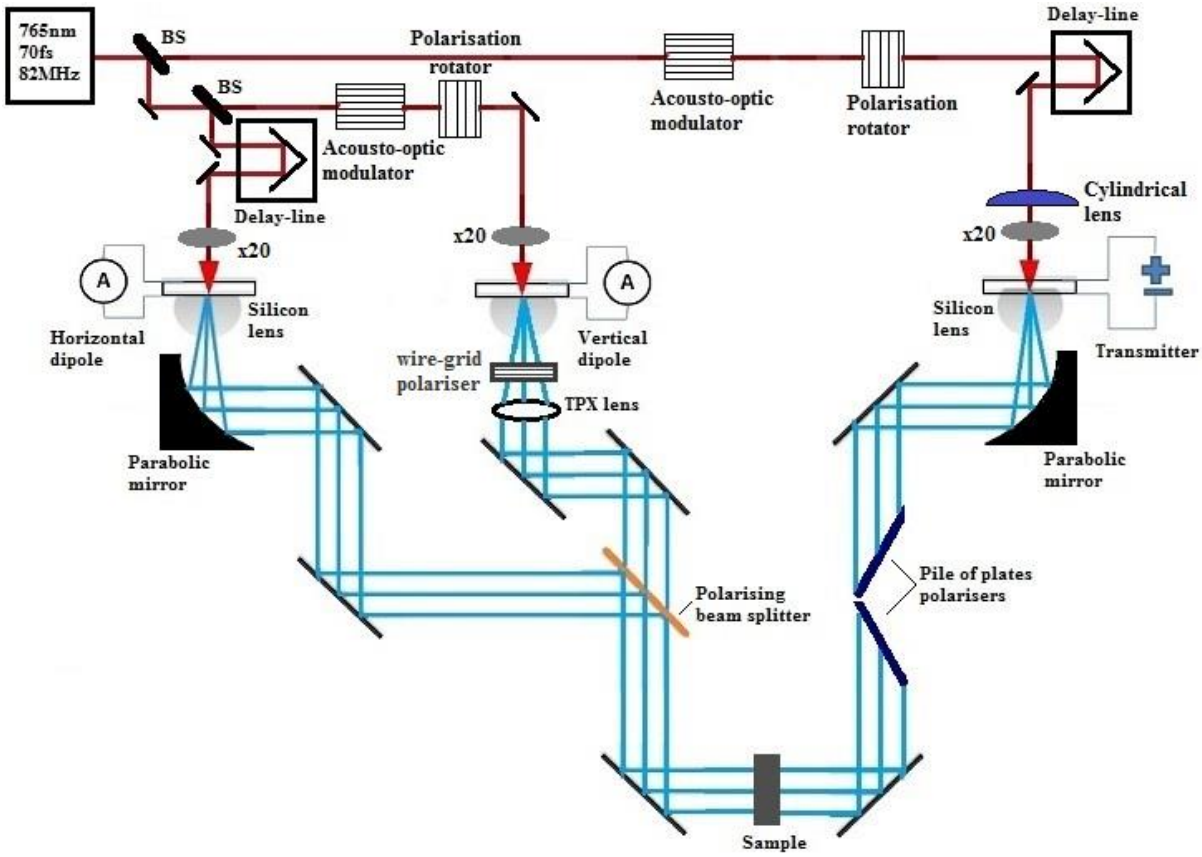

Fig 4.1: Experimental setup for the generation and the detection of THz radiation. The red line shows the laser beam path and the blue lines show the THz beam path. The setup is shown for method 1. For method 2 the polarising beam splitter is rotated to be normal to the THz beam and is used as a polariser.

The terahertz pulses incidents on the sample are linearly *p*-polarised (along the *x*-axis). Detection is performed by two LT-GaAs, 10 µm photoconductive dipole antennas. One of the dipole antennas is oriented to detect *p*-polarised radiation and the other to measure *s*-polarised radiation.

The dipole receivers have microfabricated wire-grid polarisers integrated into their substrates (8μm period Ti:Au grids) to reduce their sensitivity to orthogonal polarisations. A second delay-line in the probe arm is used to adjust the timing between detectors. A pair of "pile-of-plates" polarisers is placed after the transmitter and the parabolic collimating mirror to improve the polarisation purity. The sample is positioned in the collimated beam immediately after the pile-of-plates polarisers and the beam emerging from the sample is divided into *s* and *p* components using a polarising beam splitter; the nano-scale Al/TAC wire-grid polariser described in the previous chapter. In general there is a large p-polarised field component and a very much smaller s-polarised component induced by any optical activity in the sample.

An important consideration in the spectrometer design is the existence of a cross-polarisation effect due to off-axis illuminations when using of off-axis parabolic mirrors [7]. This effect can be as large as 10% of the peak field and its affects are avoided by using plane mirrors or lenses between the pile-of-plates polarisers in front of the sample and the detection for *s*-polarisation.

To measure the terahertz electric field of the parallel and the perpendicular radiation we have used two different methods with the same experimental system: the first method consists of using two photoconductive receivers to measure $E_{//}(t)$ and $E_{\perp}(t)$ at the same time, and the second method is based on using only one receiver to detect $E_{\perp}(t)$.

4.3.1 Method 1

In this method, one receiver detects the electric field component $E_{//}^{out}(t)$, while the other receiver detects the electric field component $E_{\perp}^{out}(t)$ of the THz pulses emerged from the sample and polarised perpendicular to the incident THz radiation. This orthogonal electric field component is due to the imperfectness of the THz transmitter and some changes in polarization on reflection at the 90° off-axis parabolic mirrors as mentioned previously in chapter 2.

Unfortunately the use of two different receivers and the different interactions of s and p-polarised beams with the beam splitter make the spectral response of the co-polarized electric field component and the cross-polarized electric field component different which required correction. There is also a possible phase error between the signals from the two receivers. Both the spectral response correction and the phase adjustment are made in prudence by changing the azimuthal angle of the beam splitter by 45 degrees. We then assume that the spectra and phases should be the same for both receivers and correct accordingly.

4.3.2 Method 2

This second method is based on the use of only the *s*-polarised receiver. The polarising beam splitter is rotated about the vertical axis by 45 degrees to act as a simple polariser as shown in figure 4.2. The advantage of this technique is that all measured electric fields have the same spectral response, which makes this method more accurate compared to the previous one. Unfortunately, this technique does measure one component ($E_{\perp}^{out}(t)$) of the electric pulse emerged from the sample which required performing more measurements of $E_{\perp}^{out}(t)$ for different angles of the polarising beam splitter (0°,+45°,-45°).

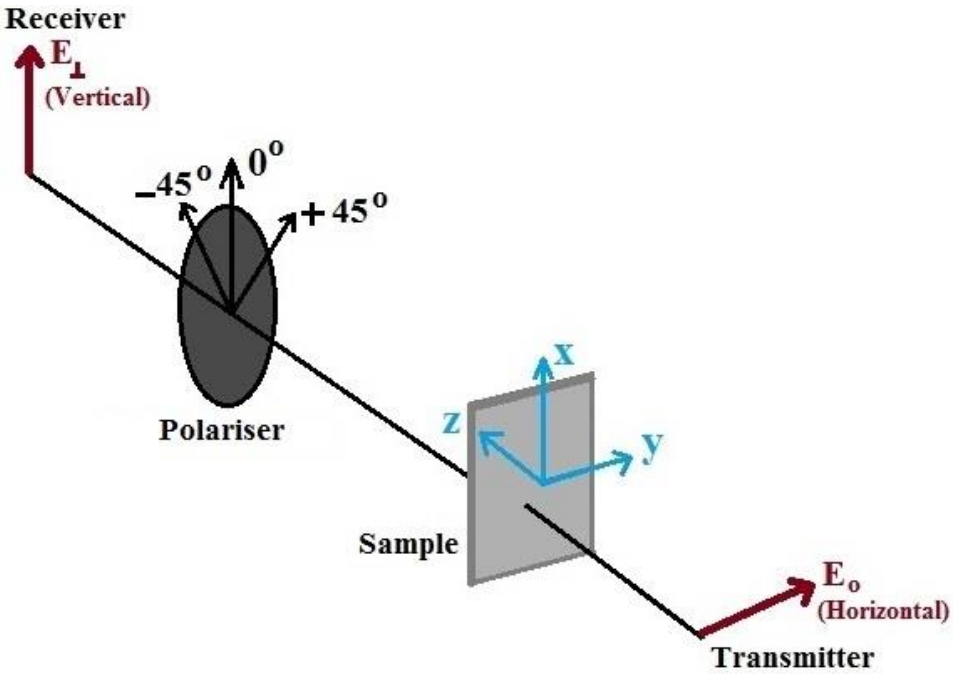

Fig 4.2: Schematic of the detection of the generated polarised light using one receiver polarised perpendicular to the incident radiation

The co-polarised component of the pulses emerging from the sample $E_{//}^{out}(t)$ can be calculated using the following equation

$$E_{//}^{out}(t) = E_{\perp}^{+45}(t) - E_{\perp}^{-45}(t), \tag{12}$$

where $E_{\perp}^{+45}(t)$ and $E_{\perp}^{-45}(t)$ are the detected electric fields of the cross-polarised component of the terahertz pulses transmitted through the sample for the polariser set at an angle of

+45° and -45° respectively. The calculated response spectra of $E_{\perp}^{+45}(\omega)$ and $E_{\perp}^{-45}(\omega)$ components are found from the fundamental equation for transmission through the sample

$$\begin{pmatrix} E_{\perp}^{out}(\omega) \\ E_{//}^{out}(\omega) \end{pmatrix} = \underline{\underline{P}}\underline{\underline{T}}(\omega) \begin{pmatrix} 0 \\ E_{//}^{in}(\omega) \end{pmatrix}, \tag{13}$$

where $\underline{\underline{T}}(\omega)$ is the transmission matrix of the sample, $\underline{\underline{P}}$ is the Jones matrix characterising the polariser and $E_{//}^{out}(\omega)$ is the spectrum of the incident pulse which can be measured by removing the sample. Considering an ideal polariser letting through only the cross-polarised component of the THz radiation, equation (13) then becomes

$$\begin{pmatrix} E_{\perp}^{out}(\omega) \\ E_{//}^{out}(\omega) \end{pmatrix} = \begin{pmatrix} 1 & 0 \\ 0 & 0 \end{pmatrix} \cdot \begin{pmatrix} t_{xx} & t_{xy} \\ t_{yx} & t_{yy} \end{pmatrix} \cdot \begin{pmatrix} 0 \\ E_{//}^{in}(\omega) \end{pmatrix} \tag{14}$$

If the structure studied has four-folder symmetry about the *z*-axis, the cross-polarised component of the incident radiation emerging from the sample is

$$E_{\perp}^{out}(\omega) = t_{xy} E_{//}^{in}(\omega) \tag{15}$$

When the polarising beam splitter is set at +45° equation (14) becomes

$$\begin{pmatrix} E_{\perp}^{+45}(\omega) \\ E_{//}^{+45}(\omega) \end{pmatrix} = \frac{1}{2} \begin{pmatrix} 1 & 1 \\ 1 & 1 \end{pmatrix} \begin{pmatrix} t_{xx} & t_{xy} \\ t_{yx} & t_{yy} \end{pmatrix} \begin{pmatrix} 0 \\ E_{//}^{in}(\omega) \end{pmatrix}, \tag{16}$$

and the spectrum of the orthogonal electric field component transmitted through the sample is

$$E_{\perp}^{+45}(\omega) = \frac{1}{2}(t_{xy} + t_{yy}) E_{//}^{in}(\omega) \tag{17}$$

When the polarising beam splitter is rotated to -45° equation (13) becomes

$$\begin{pmatrix} E_{\perp}^{-45}(\omega) \\ E_{//}^{-45}(\omega) \end{pmatrix} = \frac{1}{2}\begin{pmatrix} 1 & -1 \\ -1 & 1 \end{pmatrix}\begin{pmatrix} t_{xx} & t_{xy} \\ t_{yx} & t_{yy} \end{pmatrix}\begin{pmatrix} 0 \\ E_{//}^{in}(\omega) \end{pmatrix}, \tag{18}$$

and then the spectrum of the orthogonal electric field component transmitted through the sample is

$$E_{\perp}^{-45}(\omega) = \frac{1}{2}(t_{xy} - t_{yy})E_{//}^{in}(\omega). \tag{19}$$

By substituting the expressions for $E_{\perp}^{+45}(t)$ and $E_{\perp}^{-45}(t)$ in equation (12), we obtain the spectral response of the co-polarised transmitted field

$$E_{//}^{out}(\omega) = t_{yy}E_{//}^{in}(\omega) \tag{20}$$

Table (4.1) shows the advantages and the disadvantages of the two methods used to measure optical activity.

Methods	Advantages	Disadvantages
Method 1: using two photoconductive receivers	- direct and simultaneous measurement of the co-polarised and cross-polarised components.	- relative time delays -different spectral response of the co-polarised and the cross-polarised components: needs correction.

Method 2: using one photoconductive receiver	- directly measures cross-polarised component which is sensitive to optical rotation - uses one receiver so that no problem with spectral correction assuming that polariser transmission spectrum is independent of azimuthal angle.	- measurement of co-polarised component is indirect - needs three measurements using a polariser set at different angles - Jones matrix for polariser needs to be established experimentally.

Table 4.1: Comparison of the two methods used to determine ORD and CD

An example of the measured electric field components polarised parallel and perpendicular to the incident THz radiations thought a high resistivity silicon wafer using both methods is shown in figure 4.3. The cross-electric field component (perpendicular to the incident radiation) of the THz pulses in method 2 using one dipole photoconductive receiver was calculated from the equation (12) by measuring the electric field components when the wire-grid polariser is set at $+45^{o}$ and -45^{o}.

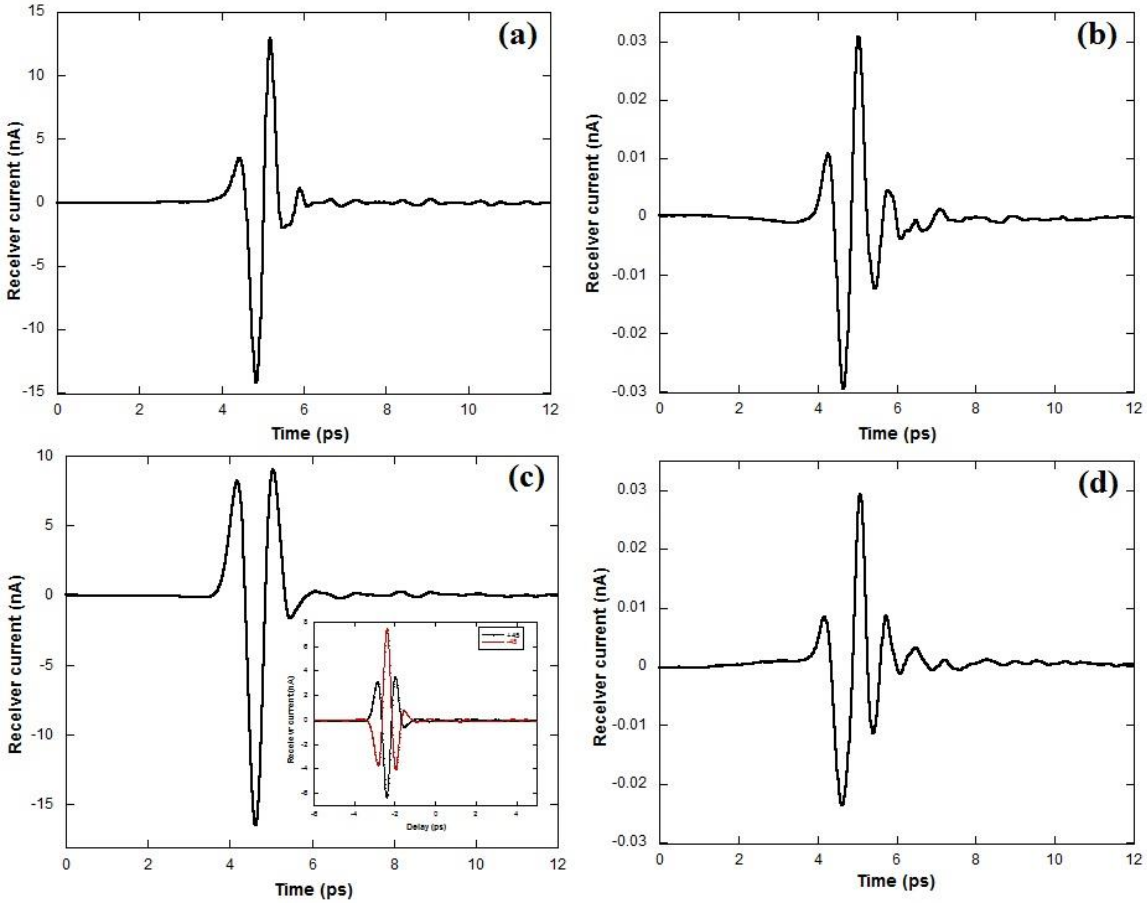

Fig 4.3: Time domain waveforms of: the measured co-polarised and cross-polarised components of the THz pulse respectively (a) and (b) using method 1, (c) the extracted co-polarised component of the THz pulse from the measured electric field components for a polariser set at +45 and -45 and (d) the measured cross-electric component of the radiation using method 2.

It is clear from figures 4.3 (a) and (c) that the amplitude of the transmitted co-polarised components using both methods is almost the same and that the shape of signals are slightly different because of the first method which is performed using two different receivers. Figures 4.3 (b) and (d) of the measured cross-polarised components show a good agreement between both methods as the detection is performed using the same receiver. It is clear from figure 4.3 that both methods used in this present work to detect the THz radiation give good results and that method 2 is more accurate as the detection is performed using the same photoconductive receiver. The figure 4.3 shows also an unwanted background signal in the *p*-polarisation with peak-to-peak amplitude ~ 1/400 of the *p*-polarised field. We attribute the existence of the s-polarised signal to polarisation conversion due to edge roughness of the metal stripes making up the polarising beam splitter and the fact that the thin substrate was noticeably distorted out of plane. This is evidently seen from the

measured electric field components as a function of the polarising beam splitter angles as shown in figure 4.4.

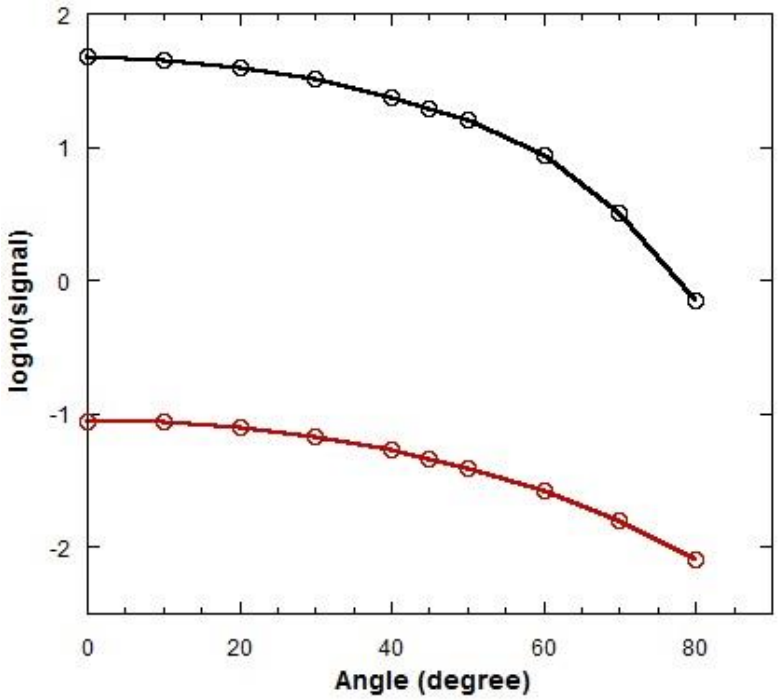

Fig 4.4: The measured (black)co-polarised and (red) cross-polarised components of the THz pulse as a function of the polarising beam splitter angles.

Figure 4.4 shows that the measured *s*-polarised component is obtained by polarisation conversion of the *p*-polarised component in the beam splitter and that it does not come from the beam before the beam splitter because if it was the case, the s-polarised component would increase with increasing the angles.

4.4 Summary

In this chapter, we have described the formalism for describing optical activity and described a spectrometer designed to measure optical activity with high sensitivity using two methods. The first one is based on a separate detection of the electric field components and the second is based on the detection of only the s-polarised component.

References

1. Rice A., Jin Y., Ma X.F., and Zhang X.-C., *Terahertz optical rectification from <110> zinc-blende crystals.* Appl. Phys. Lett., 1994. 64, 1324.

2. Chen Q, and Zhang X.-C., *Polarization modulation in optoelectronic generation and detection of terahertz beams.* Appl. Phys. Lett., 1999. 74(23): p. 3435.

3. Shimano R., Nishimura H., and Sato T., *Frequency Tunable Circular Polarization Control of Terahertz Radiation.* Japanese Journal of Applied Physics, 2005. 44(21): p. L676-L678.

4. Casto-Camus E., *Polarization-Resolved Terahertz Time-Domain Spectroscopy.* Journal of Infrared Millimeter and Terahertz Waves, 2012. 33: p. 418-430.

5. Mittleman D.M., Cunningham J.C., Nuss M.C., and Geva M., *Noncontact semiconductor wafer characterization with the terahertz Hall effect.* Appl. Phys. Lett., 1997. 71: p. 16-18.

6. Byrne M.B., Shankat M.U., Cunningham J.E., Linfield E.H., and Davies A.G., *Simultaneous measurement of orthogonal components of polarization in a free-space propagating terahertz signal using electro-optic detection.* Applied Physics Letters, 2011. 98(15): p. 151104.

7. A. Hussain, and Andrews S.R., *Ultrabroadband polarization analysis of terahertz pulses.* OPTICS EXPRESS, 2008. 16: p. 7251.

8. Makabe H., Hirota Y., Tani M., and Hangyo M., *Polarization state measurement of terahertz electromagnetic radiation by three-contact photoconductive antenna.* Optics Express, 2007. 15: p. 11650.

9. Castro-Camus E., Lloyds-Hughes J., Johnston M. B., Fraser M. D., Tan H. H., and Jagadish C., *Polarization-sensitive terahertz detection by multicontact photoconductive receivers.* Applied Physics Letters, 2005. 86(25): p. 254102.

10. Gong Y., Dong H., and Chen Z., *Cross-polarization Response of Two-contact Photoconductive Terahertz Detector.* Terahertz Science and Technology, 2011. 4(3): p. 137.

11. Neshat M., and Armitage N.P., *Improved measurement of polarization state in terahertz polarization spectroscopy.* Optics Letters, 2012. 37(11): p. 1811.

12. Menzel C., Rockstuhl C., and Lederer F., *Advanced Jones calculus for the classification of periodic metamaterials.* Physical Review A, 2010. 82(5): p. 053811.

13. Zhu W., Rukhlenko I.D., Huang Y., Wen G., and Premaratne M., *Wideband giant optical activity and negligible circular dichroism of near-infrared chiral metamaterial based on a complementary twisted configuration.* Journal of Optics, 2013. 15(12): p. 125101.

Chapter 5

Optical Activity in Metal Screw Hole Array

5.4 Introduction

Significant efforts have been devoted to conceiving and studying various materials containing chiral structures for enhanced optical activity, including thin structured metallic layers such as conjugated gammadions [1] and double four-U structures [2]. These structured metals show strong optical properties compared with structured dielectrics owing to their high conductivity. Helical conformations are considered to be the most universal form of chiral materials due to their wide presence in nature. Over a century ago, experiments demonstrated the significance of the helical shape in affecting light polarisation [3] and showed polarisation rotation of radiation transmitted through helices, which qualitatively established the structural similarities between the macroscopic helical structures and the microscopic optically active molecules [4, 5]. Since then various theoretical and experimental works have been performed in the terahertz and microwave range [6-8] that showed that the optical activity of helical conformations fundamentally arises from the anisotropic scattering of left- and right- circular light from the geometrical shape of the helix [9].

Since the extraordinary optical transmission (EOT) phenomena were reported in metallic films perforated with sub-wavelength size holes [10], the optical properties of these structures have been the focus of an increasing research activity. In EOT the transmittance per hole in a structure containing subwavelength apertures is several orders of magnitude larger than expected from its area [10]. Similar behaviour was also reported in the terahertz region [10]. At optical frequencies, EOT is associated with the excitation of surface plasmon polaritons (SPPs) at corrugated metal surfaces which can propagate efficiently through holes because of their strong surface localisation [10-13]. At THz and microwave regions, enhanced transmission has also been realised [14-15] and it was shown that the resonantly enhanced transmission process is mediated by geometrically controlled cavity resonances called Spoof plasmons [13] rather than surface plasmons.

The polarisation characteristics of metal hole arrays has received less attention than the transmittance. In this chapter, the polarisation conversion properties of metal screw hole arrays are presented. These metal screw hole arrays are arrays of cut-through screw holes in a metal plate.

5.2 Metal screw hole array

We designed two metal hole arrays, the first one has threaded (chiral) holes and the second one smooth wall (achiral) holes. The latter metal hole array is used as reference and has the same overall dimensions as the metal screw hole array. The array of screw holes is a two-dimensional square periodic structure with *a=2.00mm*; the distance between the centres of two adjacent holes. The slab is made of aluminium and has a thickness *t=2.00mm*. The outside and inside diameters of the screw hole are d_{out}*=1.00mm* and d_{in}*=0.76mm* respectively and the pitch of the screw is *p=0.25mm*. Figure 5.1 shows the array of screw holes as well as a cross section of the screw hole. We note that the metal screw hole array used in our experiments has a right-hand thread.

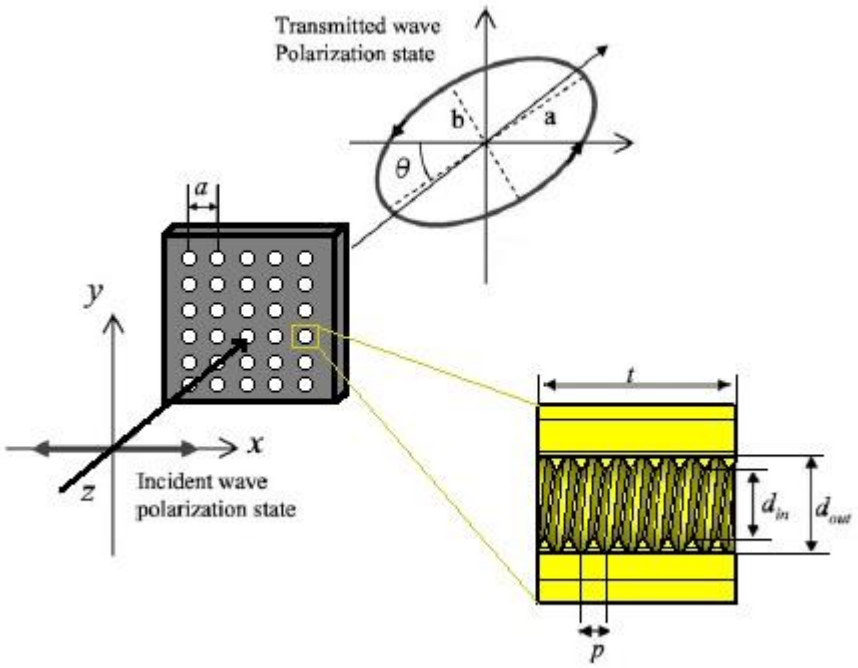

Fig 5.1: Optical configuration for the THz wave and the chiral material and a cross section of one of the metal screw.

We explored the terahertz optical activity of both structures by measuring the time evolution of the transmitted THz electric field pulse using the THz time domain spectroscopy setup described in chapter 3. Orthogonal linearly polarised components of the electric field transmitted through the two chiral materials are measured independently: the co-polarized, $E_{//}(t)$ (parallel to incident THz electric field pulse polarization), and cross-polarized, $E_{\perp}(t)$ (perpendicular to incident THz electric field polarization). From these electric field components of the THz radiations, the left-hand $E_L(t)$ and the $E_R(t)$ right-hand

electric fields components transmitted through the samples, are constructed according to equations (1) or (2) in chapter 4. By Fourier transformation, the measured left-hand and right-hand terahertz fields were converted into the spectra of the transmission amplitude and phase shift, and then into the spectra of the optical rotational dispersion (ORD), the circular dichroism (CD) and the rotation angle θ.

Computational studies have been performed using electromagnetic simulation in CST Microwave Studio. Both structures were modelled as lossy metal aluminium (Al) with an electric conductivity of 3.56 x 10^7 S/m and by applying periodic boundary conditions over a single unit cell. The constructed model used specification for the basic isometric screw thread of size 1. Figure 5.2 illustrates a side view of the simulated screw thread and a sketch of the isometric thread profile. H and P are respectively the height and the pitch, and are related by the following expression H= (2/√3) x P. The dimensions of the metal screw hole arrays matched physically with the ones employed in the experiments as closely as possible, although same uncertainty in experimental parameters.

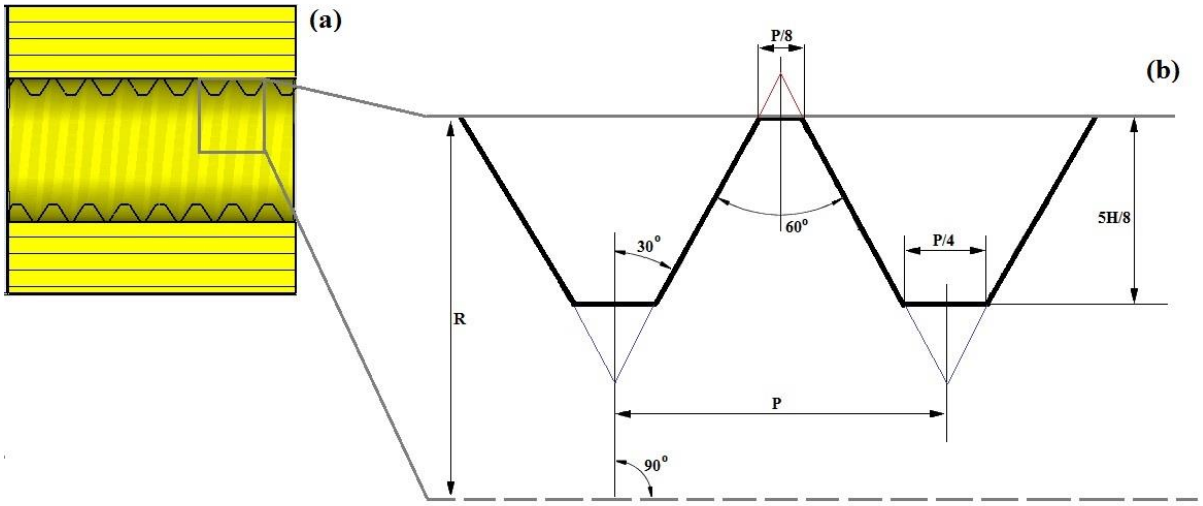

Fig 5.2: (a) Cross-section of the simulated CST screw thread model. (b) Sketch of the isometric screw thread profile.

5.3 Experimental and computational results

In order to explore and understand the optical activity associated with our metal hole array, we used the polarisation sensitive THz time domain spectroscopy setup described in the previous chapter. The metal hole array (achiral) and metal screw hole array (chiral) were mounted on a 3D translation stage in order to centre the generated terahertz beam of ~16 mm diameter on the metal arrays and to ensure that the whole material is sampled.

We first measured the transmitted electric field through both at normal incidence. The linear polarisation of the incident pulses is parallel to an axis of the square cell structure. Figures 5.3 (a) and (b) show respectively the spectra corresponding to the measured co-polarised and the cross-polarised transmitted components of the THz pulses through both samples. Figures 5.3 (c) and (d) show respectively the spectra of the optical rotational dispersion (Eq. 10 a) and the circular dichroism (Eq. 10 b).

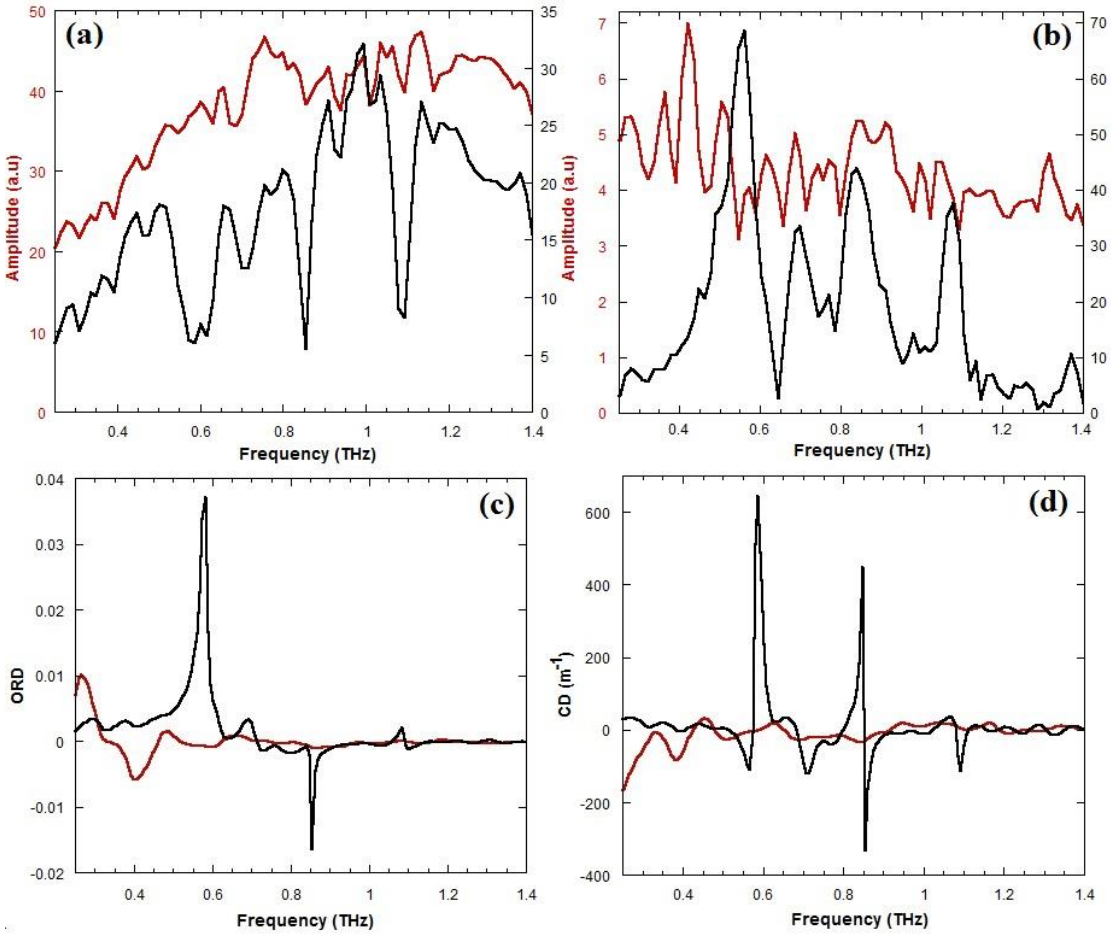

Fig 5.3: (a) and (b) are respectively the spectra of the measured co-polarised component and the cross polarised component of the THz radiation transmitted through: (red) the metal hole array and (black) the metal screw hole array. (c) and (d) are respectively the optical rotational dispersion and the circular dichroism spectrum.

The spectra of the co-polarised and cross-polarised components of the THz radiation transmitted through the metal screw hole array respectively in figures 5.3 (a) and (b) show pronounced dips at three different frequencies; 0.6, 0.9 and 1.1 THz which do not appear in the spectra for the smooth bare metal hole array. Moreover the measured spectra of ORD and CD in figure 5.3 (c) and (d) respectively of the achiral sample show a flat spectrum close to zero over the entire spectral range. This indicates that the terahertz waves preserve

their polarization state after transmission through the achiral holes as expected. The ORD and CD spectra in figure 5.3 (c) and (d) respectively, of the metal screw hole arrays show a strong peak at around 0.6 THz with the peak value of 0.04 (ORD) and 700m^{-1} (CD) and other distinctive peaks at 0.9 THz and 1.1 THz which correspond to the peaks and dips in the spectra of the co-polarised and cross-polarised components of the THz radiation transmitted through the metal screw hole array. This means that the transmitted terahertz waves have elliptical polarization, and that the screw hole array has a chiral structure. Simulations were also performed to study transmission through the metal screw hole arrays. Figures 5.4 (a) and (b) show respectively the calculated spectra of the electric field components polarised parallel and perpendicular to the incident radiation and transmitted through the chiral material and figure 5.4 (c) shows the calculated spectra of CD for the metal screw hole array.

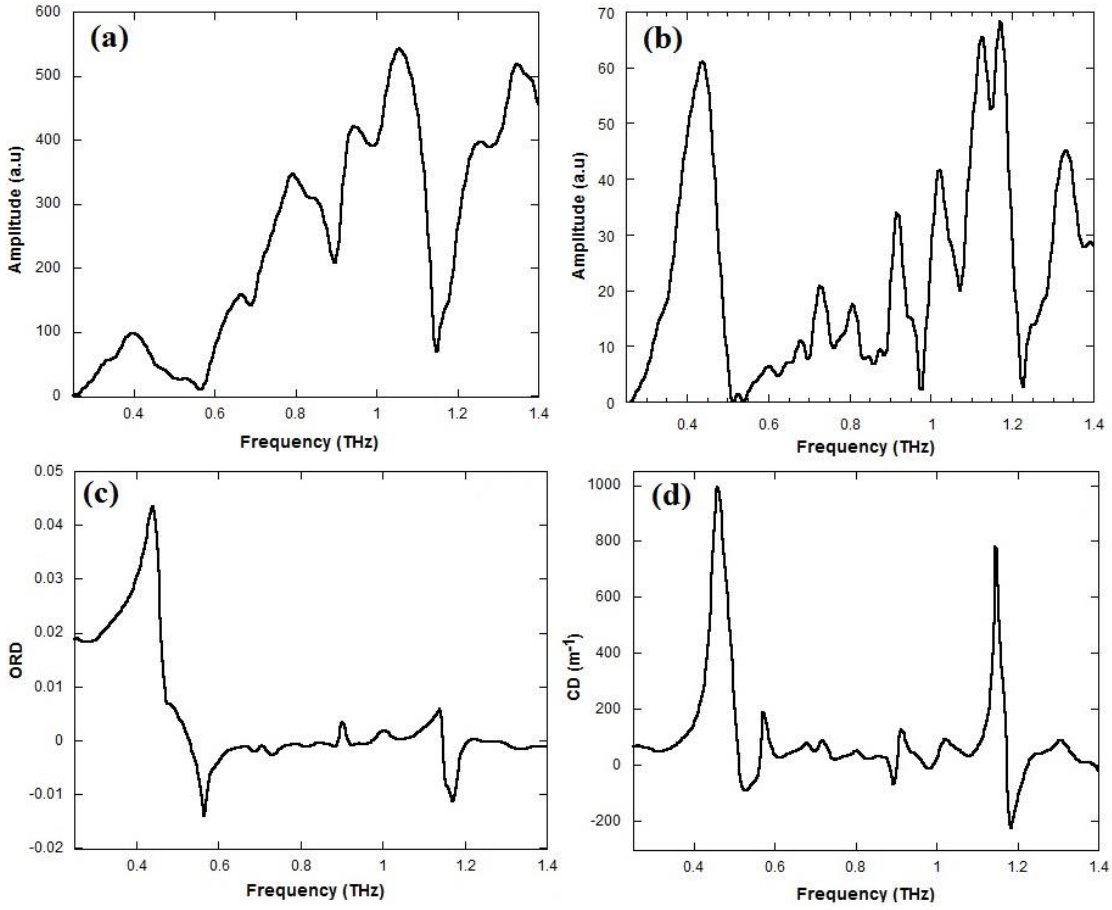

Fig 5.4: (a) and (b) are respectively the calculated spectra of the co-polarised component and the cross polarised component of the THz radiation transmitted through a metal screw hole array.(c) and (c) are respectively the calculated optical rotational dispersion and the circular dichroism spectrum.

The spectrum of the calculated electric field component polarised parallel to the incident linear polarisation in figure 5.4 (a) shows three spectral dips at ~ 0.6 THz, 0.9 THz and 1.1 THz which agree with the three of the dips shown in figure 5.3 (a) of the measured spectrum. However in perpendicular polarisation shown in figure 5.4 (b), the peaks are slightly shifted in the calculation compared to the measurements. The calculated spectrum of the optical rotational dispersion and the circular dichroism in figure 5.4 (c) and (d) respectively, show three pronounced peaks at ~ 0.5, 0.9 and 1.2 THz which almost agree with the experimental results in figure 5.3.

The strong optical activity around 0.6 THz shown in figure 5.3 and figure 5.4 is probably due to the cavity resonance of the screw hole in which electromagnetic waves exist in a hollow space inside the screw hole ($L= n\lambda/2$, n=1,2…) where L is the length of the sample, the transmission resonant mediated by surface plasmon polariton (SPP) or the screw pitch resonance [16]. In order to examine these three hypotheses and determine the actual origin of the optical activity, we first calculated the polarisation state after transmission through three metal screw hole arrays with different thicknesses (t=2.0, 2.5, and 3.0 mm). Figure 5.5 shows the spectra of the calculated co-polarised and cross-polarised components of a transmitted THz pulse.

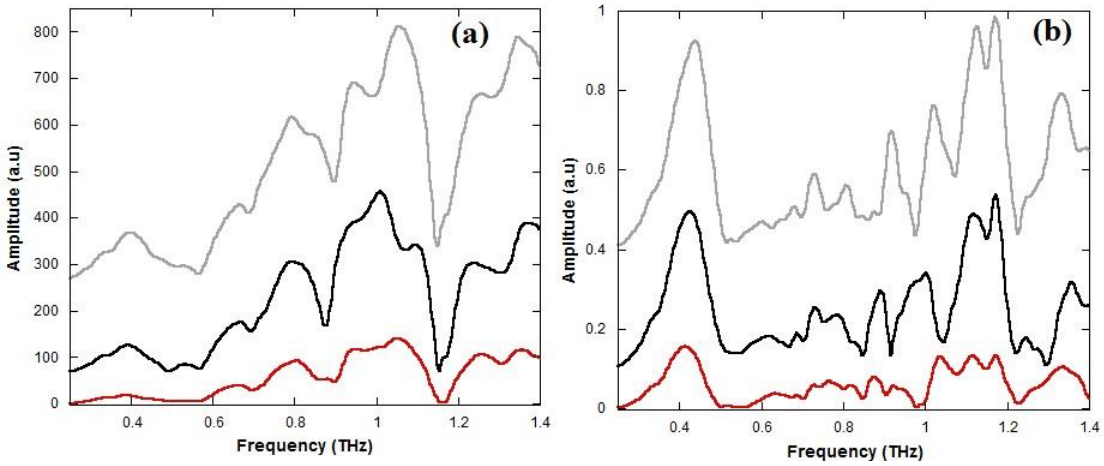

Fig 5.5: (a) and (b) are respectively the spectra of the co-polarised component and the cross-polarised component of the THz radiation transmitted through the metal screw hole arrays with (gray) 2.0 mm, (black) 2.5 mm and (red) 3.0 mm thicknesses.

The spectra of the calculated co-polarised and cross polarised components of the THz pulse transmitted through the three metal screw hole array in figures 5.5 (a) and (b) respectively, show the same characteristic frequency dependence. The three chiral materials have distinctive dips and peaks at the same frequencies; 0.6 THz, 0.9 THz and 1.1 THz. Figures 5.5 (a) and (b) show also that the amplitude of the transmitted electric field components of the incident radiations through the three chiral materials decreases with increasing the thickness of the metal arrays. This decrease of amplitude is mainly due to

ohmic loss. Figure 5.6 shows the rotation angle corresponding to the calculated electric field components of the THz radiation emerging from the three metal screw hole arrays with different thicknesses (t=2.0, 2.5, and 3.0 mm).

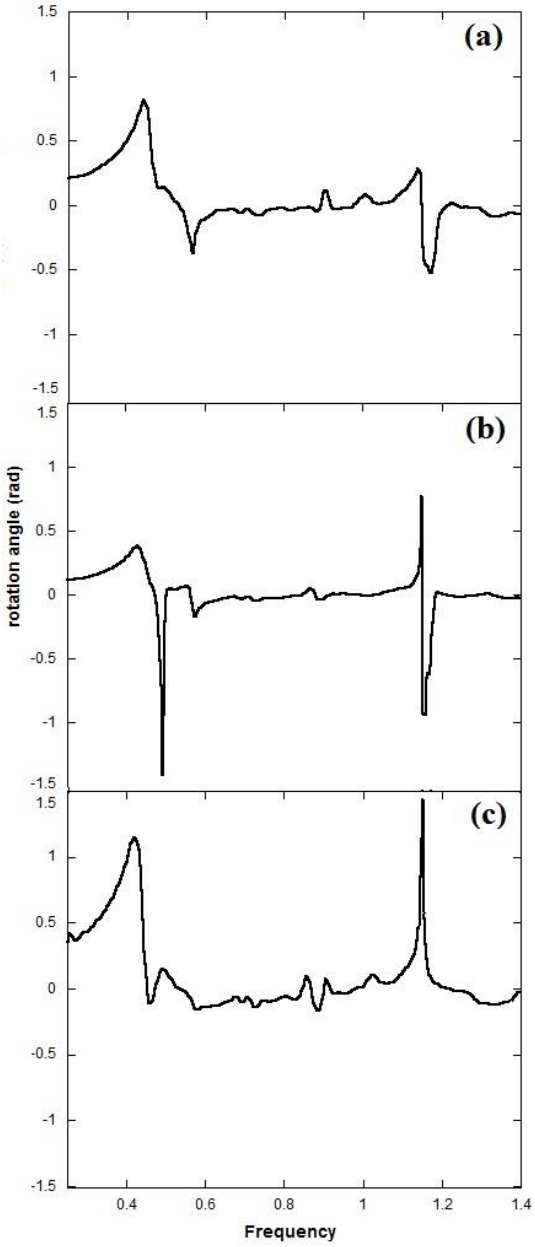

Fig 5.6: (a), (b) and (c) are respectively the calculated spectra of the rotation angle of the THz radiation transmitted through the metal screw hole arrays with 2.0 mm, 2.5 mm and 3.0 mm thickness.

The spectra of the rotational angle in figure 5.5 show permanent features at ~ 0.5, 0.9 and 1.2 THz for the three samples with different thicknesses which almost coincide with the peak frequencies found in figure 5.3 and figure 5.4. The results in figure 5.5 and figure 5.6

show that the rotational angle spectrum is unaffected by the thickness which means that the three resonant frequencies are independent of the thickness of the chiral metal screw hole arrays. These results confirm that the resonant frequencies are unrelated to cavity resonances.

To examine the second hypothesis of transmission mediated by spoof surface plasmon polariton (SPP), we performed experimental and computational studies of a single screw hole. Figure 5.7 shows the measured and calculated CD and rotational angle spectrum corresponding to the co-polarised and the cross-polarised components of THz pulse transmitted through a single screw hole.

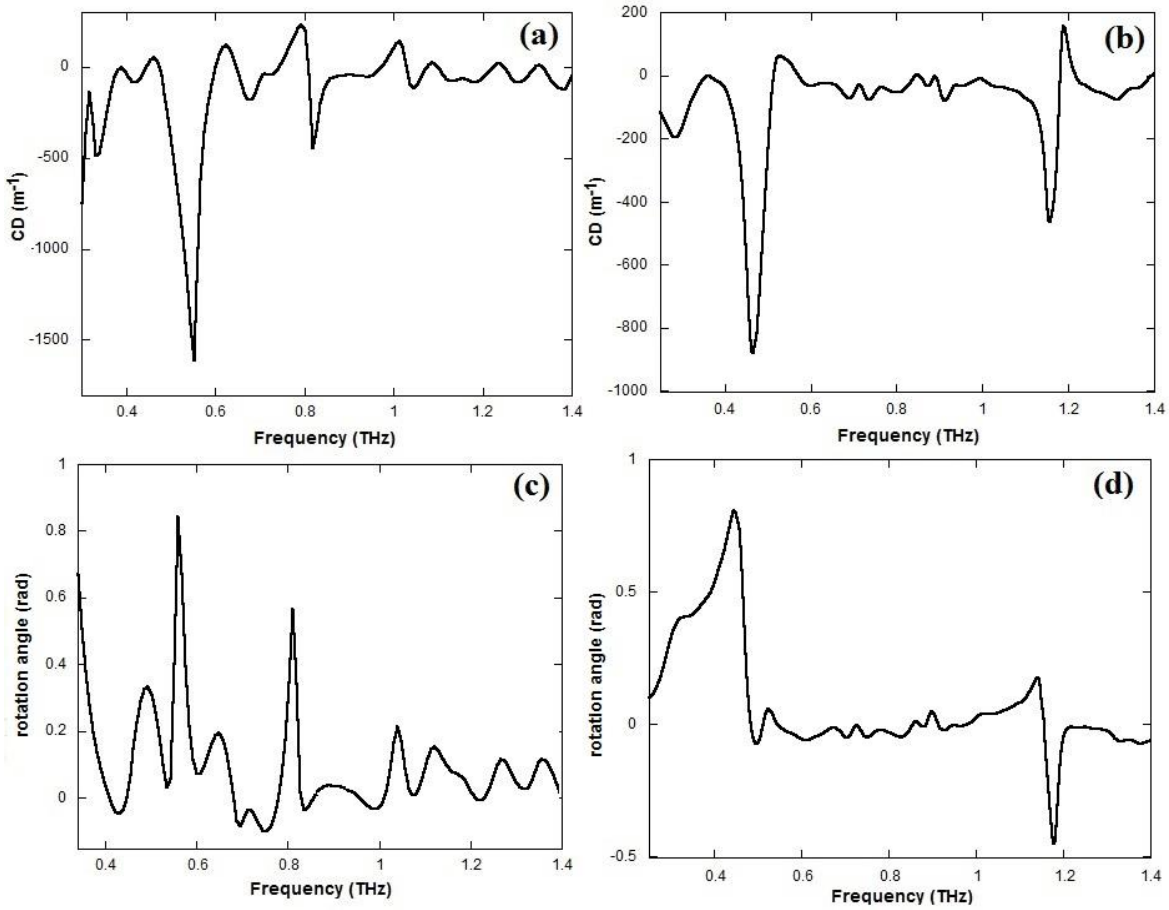

Fig 5.7: (a) and (b) are respectively the spectra of the measured and the calculated CD for THz radiation transmitted through a single screw hole. (c) and (d) are respectively the spectra of the measured and the calculated rotation angle of THz radiation transmitted through a single screw hole.

Figures 5.7 (a) and (b) show measured and calculated the CD spectra for a single screw hole and exhibit three pronounced dips at ~ 0.5 THz, 0.9 THz and 1.1 THz which closely correspond to the dips observed in figure 5.3 and figure 5.4 for the screw hole array. Moreover the measured and the calculated rotation angle spectra of the transmitted field through the single screw hole shown respectively in figure 5.7 (c) and figure 5.7 (d) also show features at ~ 0.5, 0.9 and 1.1 THz which are in a good agreement with the distinctive dips shown in figure 5.6 (a) of the screw hole array. These results indicate that the optical activity in the screw hole array is induced by the structure of a single hole which excludes the second hypothesis of transmission mediated by surface plasmon polariton (SPP) as the resonant frequencies for optical activity of the single hole and the array of holes coincide.

To examine the last hypothesis of screw pitch resonance, we investigated the relation between the screw pitch and the resonant frequency. It is well known that the relation between the wavelengths of an electromagnetic wave λ_g in a waveguide is different from that in free space and can be expressed as

$$\lambda_g = \frac{\lambda}{\sqrt{1-(\lambda/\lambda_c)^2}}, \tag{2}$$

where λ is the wavelength in the vacuum and λ_c is the cutoff wavelength of the TE_{11} mode in a metallic waveguide (screw hole) [16] . The dominant mode of the screw waveguide that can couple to linearly polarised light is the TE_{11} mode. In our experiment, the diameter of the hole is considered equal to the average diameter between the inside and the outside diameters of the screw holes (d= [d_{in}+d_{out}]/2= 0.88 mm). The cutoff wavelength of TE_{11} mode in a metallic waveguide is given by

$$\lambda_{c,11} = \frac{2\pi d}{\chi'_{11}}, \tag{3}$$

where χ'_{11} is the 1st zero of the derivative of the Bessel function of the first kind of order 1. For the TE_{11} mode, the cutoff wavelength in the metallic waveguide corresponds to λ_c=1.50 mm. The wavelength of the electromagnetic wave in an infinitely long screw waveguide satisfies the relation [16]

$$\lambda_g = np, \tag{4}$$

where *p* is the screw pitch and n is an integer corresponding to the resonant frequencies of the waveguide modes in the cavity [17]. Figure 5.8 shows the position in the measured rotation angle spectrum of the calculated frequencies at which the corresponding wavelengths of the waveguide modes in the cavity λ_g satisfy equation (4).

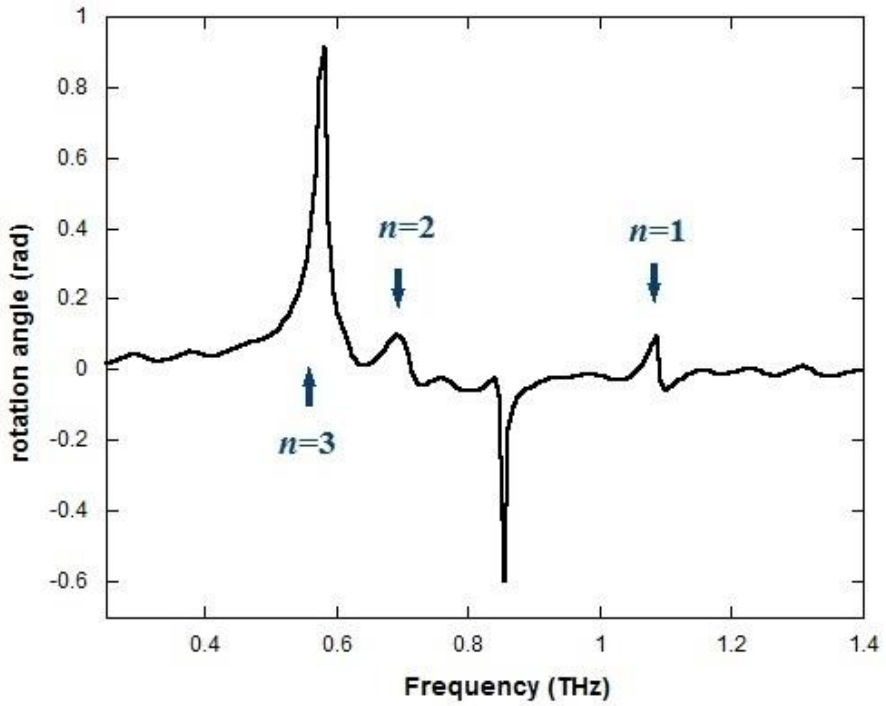

Fig 5.8: The rotation angle spectra corresponding to the calculated electric components of the THz radiation transmitted through the metal screw hole arrays and the frequencies of the screw pitch resonances (blue arrows).

The calculated frequencies of the screw pitch resonances are indicated by vertical solid arrows in figure 5.8 and show a good agreement with the spectral position of some peaks and dips in the measured rotational angle spectra of the transmitted THz pulse through the screw hole array. These results confirm that the resonant optical activity is associated with the screw pitch rather than with cavity resonances or surface waves.

5.3 Conclusion

We have presented experimental and computational studies of the THz optical activity in a metal screw array via the optical rotational dispersion, the circular dichroism and the rotation angle spectra of the THz transmitted radiation. The results show that the optical activity of the chiral material is enhanced when the frequency of the terahertz radiation coincides with the resonant frequency of the screw pitch but do not appear to be associated with cavity resonances as was previously suggested in reference [17].

References

1. Zhao R., Zhang L., Zhou J., Koschny Th., and Soukoulis C.M., *Conjugated gammadion chiral metamaterial with uniaxial optical activity and negative refractive index.* Physical Review B, 2011. **83**: p. 035105.

2. Li Z., Zhao R., Koschny T., Kafesaki M., Alici Kamil B., Colak E., Caglayan H., Ozbay E., and Soukoulis C.M., *Chiral metamaterials with negative refractive index based on four "U" split ring resonators.* Applied Physics Letters, 2010. **97**(8): p. 081901.

3. Bose J.C., *On the Rotation of Plane of Polarisation of the Electric Waves by Twisted Structure.* Proceedings of the Royal Society of London A, 1898. **63**: p. 146-152.

4. Mason S.F., *Optical Activity and Molecular Dissymmetry.* Contemp. Phys., 1968. **9**: p. 239-256.

5. Francis P., *Polarization of Light Scattered by Isotropic Opalescent Media.* The Journal of Chemical Physics, 1942. **10**(7): p. 415-427.

6. Vallius T., Jefimovs K., Turunen J., Vahimaa P., and Svirko Y., *Optical activity in subwavelength-period arrays of chiral metallic particles.* Applied Physics Letters, 2003. **83**(2): p. 234.

7. Kuwata-Gonokami M., Saito N., Ino Y., Kauranen M., Jefimovs K., Vallius T., Turunen J., and Svirko Y., *Giant Optical Activity in Quasi-Two-Dimensional Planar Nanostructures.* Physical Review Letters, 2005. **95**(22): p. 227401.

8. Papakostas A., Potts A., Bagnall D., Prosvirnin S., Coles H., and Zheludev N., *Optical Manifestations of Planar Chirality.* Physical Review Letters, 2003. **90**(10): p. 107404.

9. Chau K. J., Quong M.C., and Elezzabi A.Y., *Terahertz time domain investigation of axial optical activity from a sub-wavelength helix.* Optics Express, 2007. **15**(6): p. 3557-3567.

10. Ebbesen T.W., Lezec H.J., Ghaemi H.F., Thio T., and Wolff P.A., *Extraordinary optical transmission through sub-wavelength hole arrays.* Nature 1998. **391**: p. 667-668.

11. Barnes W., and Sambles R., *Only Skin Deep.* science, 2004. **305**: p. 785-786.

12. Garcia-Vidal F.J., Martin-Moreno L., Ebbesen T.W., and Kuipers L., *Light passing through subwavelength apertures.* Reviews of Modern Physics, 2010. **82**(1): p. 729-787.

13. Pendry J.B., Martin-Moreno L., and Garcia-Vidal F.G., *Mimicking Surface Plasmons with Structured Surfaces.* Science, 2004. **305**: p. 847-848.

14. Ciao H., and Nahata A., Resonantly enhanced transmission of terahertz radiation though a periodic array of suvwavelength apertures. Opt. Express **12**(6): p. 1004-1010 (2004).

15. Qu D., Grischkowsky D., and Zhang W., Terahertz transmission properties of thin, subwavelength etallic hole arrays. Opt. Lett. **29**(8): p. 896-898 (2004).

16. Nagashima T., Tani M., and Hangyo M., *Polarization-sensitive THz-TDS and its Application to Anisotropy Sensing.* Journal of Infrared, Millimeter, and Terahertz Waves, 2013. **34**(11): p. 740-775.

17. Miyamaru F., Hangyo M., *Strong optical activity in chiral metamaterials of metal screw hole arrays.* Applied Physics Letters, 2006. **89**(21): p. 211105.

Chapter 6

Optical Activity in Quasi-2D metamaterials

6.3 Introduction

Chiral materials are materials having electric and magnetic dipole moments which exhibit optical activity when they are excited by the field of an incident electromagnetic wave [1]. This optical activity phenomenon which is manifested in the ability to rotate the plane of polarisation of electromagnetic waves, has been widely exploited in many areas of science, including optoelectronics, analytical chemistry, molecular biology and displays. Optical activity can be exhibited either by natural or artificial chiral materials. However natural chiral materials such as quartz exhibits very weak optical activity (κ=5 x 10^{-5} at λ=400 nm), where κ is the chirality parameter which links D and H and B and E in the macroscopic constitutive relations. (κ= [n_R-n_L]/2) and n_R, n_L are respectively the refractive index of the right and left handed circular polarised wave [1]. Consequently a number of research groups have investigated the development and the design of artificial chiral materials which exhibit large optical rotation, circular dichroism [2, 3] and negative refractive index [1], and are of interest for polarisation control applications in microwave, terahertz and optoelectronic devices [4-6]. Recently the development of chiral metamatrials research has focused on the achievement of unusual optical functionalities at terahertz frequencies [7-11]. However, due to the complex geometry of these chiral metamaterials, experimental achievements of metamaterials with negative index of refraction at the terahertz region and higher frequencies is still a big challenge. Metamaterials exhibiting negative refraction at optical frequencies have been developed in the past couple of years [12, 13]. Metamaterials are made from periodic arrays of conducting elements that exhibits negative electric and/or magnetic permittivity over a band of frequencies [14]. It was demonstrated that the negative refraction of these materials increased considerably if chirality is introduced [15, 16]. These metamaterials can behave as an effective medium for electromagnetic scattering if only the dimension of both the elements and the cell spacing is much smaller than the wavelength.

Recently, a new category of chiral structures, known as planar chiral metamaterials has made it possible to extend the concept of chiral structures to higher frequencies. These chiral metamaterials have attracted much interest due to their intriguing polarisation properties such as large polarisation conversion and large optical rotation [17-19]. Various structures have been proposed such as arrays of gammadion-shaped nanoparticles [20-23], conjugated double Z metamaterial [24], twisted pairs of rossetes [25, 26] or crosses [3, 25, 27], U-shaped SRRs [28, 29]. Since these chiral metamaterials have a planar structure,

operating from microwaves up to optical regime is in principle achieved by using planar technologies to fabricate patterns down to the nm scale. However the plasmon response of materials is very different at these extreme frequencies so that not all properties are easily translated between frequencies.

In this chapter, an experimental and theoretical study of the terahertz polarisation properties of planar gammadion structures is described. The chiral properties of these materials are substantially enhanced through electromagnetic coupling between neighbouring pairs of conductors.

6.4 Planar Gammadion structures

The planar chiral designs employed in the present study are shown in figure 6.1. The chiral metamaterial structures are based on unit cells composed from gamma shapes, rotated relative to each other by an angle of $\varphi = 90^{o}$ to form what are called gammadions. The structures are only in the presence of the substrate. The cells are arranged in a two-dimensional square periodic lattice, and the period is 160 μm. The thickness of the gammadion metal and the line width are t = 0.2 μm and w = 20 μm respectively. The maximum length of the gammadion structure is l = 100 μm. The fabrication was performed using standard UV-lithography. The process of the manufacturing was as follow: we started by spinning S1813 photoresist on a thin film of 36 μm thick Mylar. We baked it for a few minutes to harden the photoresist and then exposed and developed it. A 200 nm metal-layer of aluminium was deposited, followed by a lift-off process in which for the first sample in figure 6.1 (a), the metal layer was removed around the patterns, whilst the second sample shown in figure 6.2 (b) only had metal around the patterns. The two structures are therefore complementary. The resultant samples cover an area of 1500 μm x 1500 μm. The structures have a four-fold symmetry, which allows for observation at normal incident with no birefringence.

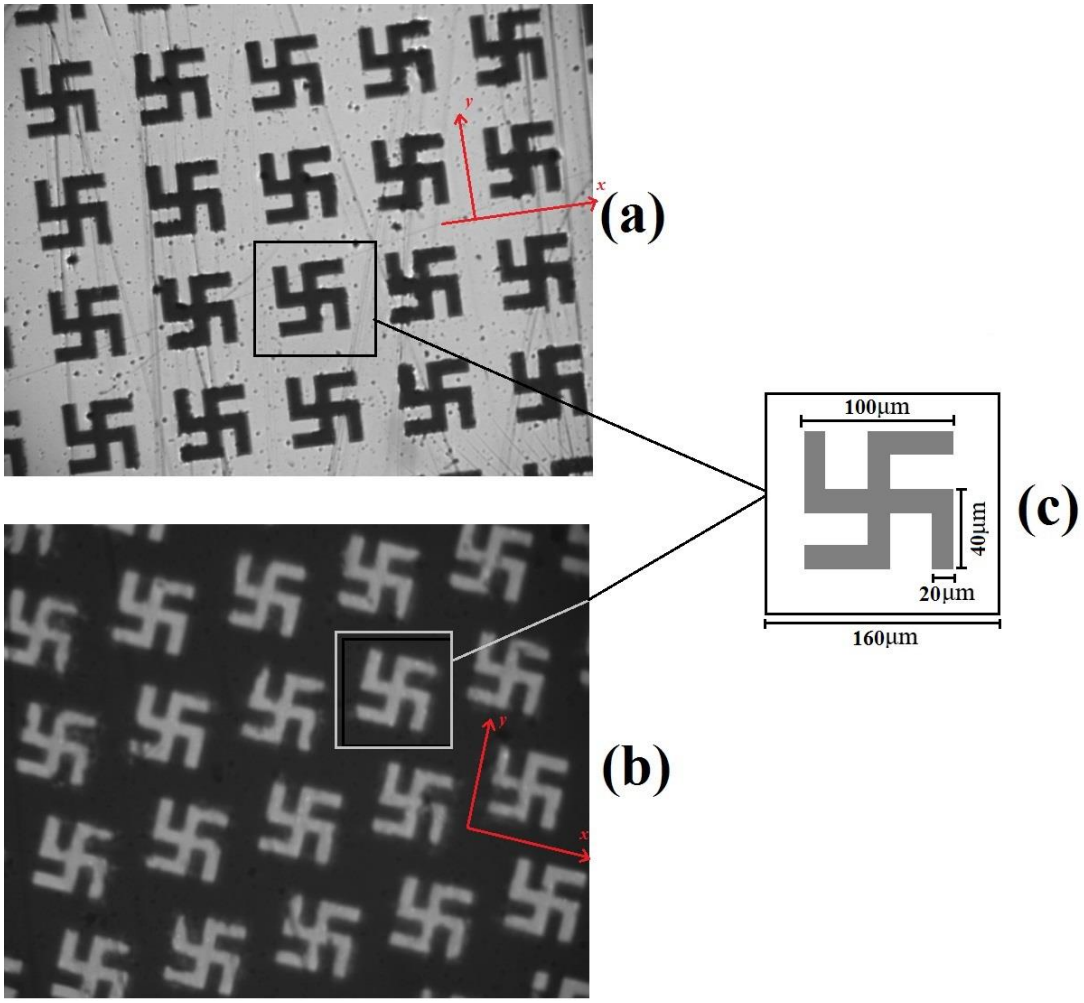

Fig 6.1: Microscopic image of the fabricated gammadion structures with a periodic lattice in both lateral directions with: (a) the aluminium metal deposited on the gammadion patterns and (a) the aluminium metal deposited outside the gammadion patterns. (c) Schematic figure of a unit cell of the gammadion structure and their dimensions.

The polarisation characteristics exhibited by these two chiral structures and the transmission measurements of the electric field components parallel and perpendicular to the incident radiation were performed using the terahertz time-domain spectroscopy setup described in chapter 4. The results were then compared with responses calculated using a commercial three-dimensional full-wave solver (CST Microwave Studio) based on the Finite Integration Technique [30]. For the simulations we have used the same dimensions as in the experiments. The propagation direction of the incident radiation was along *z*. For the metallic parts (on patterns figure 6.1 (a) and outside patterns figure 6.1 (b)) we used lossy aluminium in the calculation with an electric conductivity of $\sigma_{Al} = 3.56 \times 10^7$ (S/m). For the thin Mylar substrate, we used a permittivity of 3.1.

6.3 Experimental and theoretical results

In order to study the behaviour of the planar chiral structures, they were illuminated by linearly polarised terahertz collimated radiation, where the electric field *E* was in the *x* direction (see fig 6.1). Transmitted electric field components polarised in the *x* and *y* directions, were measured using two separated dipole photoconductive receivers (i.e. method 1 chapter 4). The time domain traces with a reference Mylar substrate and with the samples are shown in figure 6.2.

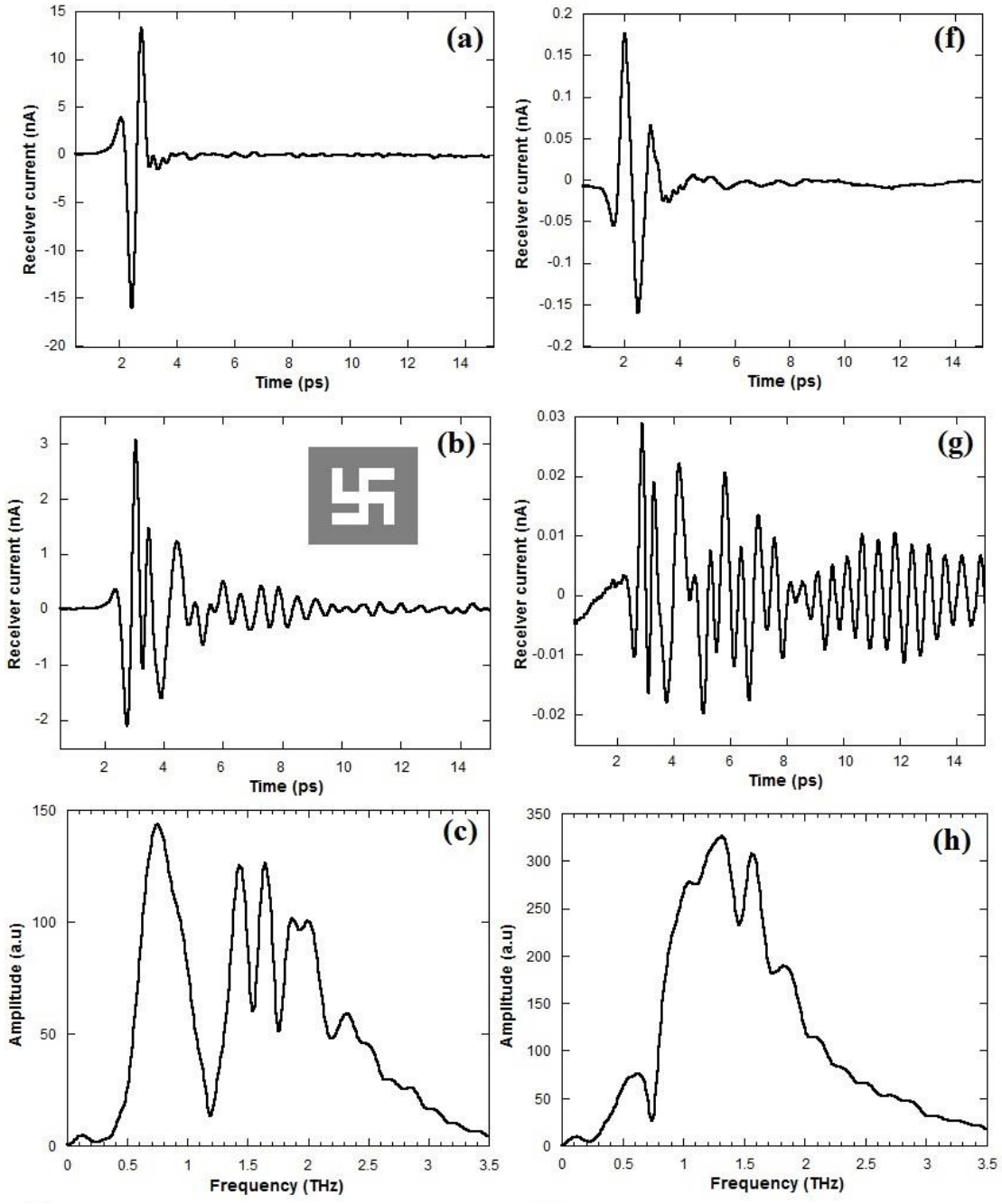

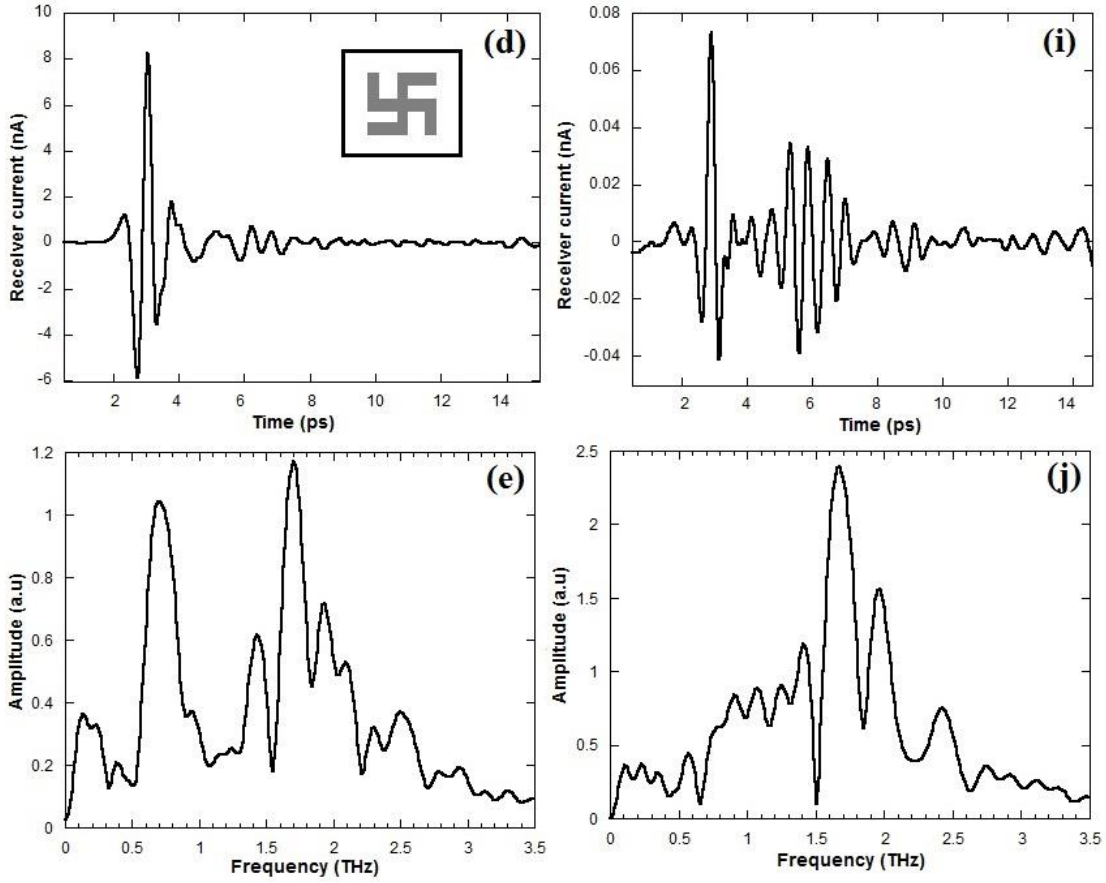

Fig 6.2: Time domain traces of the transmitted electric field components polarised parallel (left-hand panels) and perpendicular (right hand panels) to the incident radiation: (a), (f) with Mylar substrate, (b), (g) through the gammadion with aluminium metal outside the patterns and (d),(i) through the gammadion with aluminium metal on the patterns. (c), (e), (h) and (j) are respectively the spectra corresponding to (b), (d), (g) and (i).

One can observe from the time domain traces of the electric field components transmitted through the planar structures in figures 6.2 (b)/(d) and figures (e)/(i) respectively, that the signals are slightly delayed compared to the reference signal measured with Mylar substrate in figures (a) and (f). This relative delay between the signals is related to the propagation delay times of the terahertz radiations during the propagation through the gammadion structures. Figures 6.2 (b), (d), (e) and (i) show pronounced oscillations in the electric field after ~ 1.3 ps after the first pulse, compared to the transmitted field through Mylar substrate in figures 6.2 (a) and (f), which correspond to the different dips shown in the spectra figures 6.2 (c)/(e)/(h) and (j). Figure 6.3 compares time domain traces of the measured and the simulated electric field polarised perpendicular to the polarised radiation and transmitted through both samples for two different azimuthal positions which differ by 90^{o}.

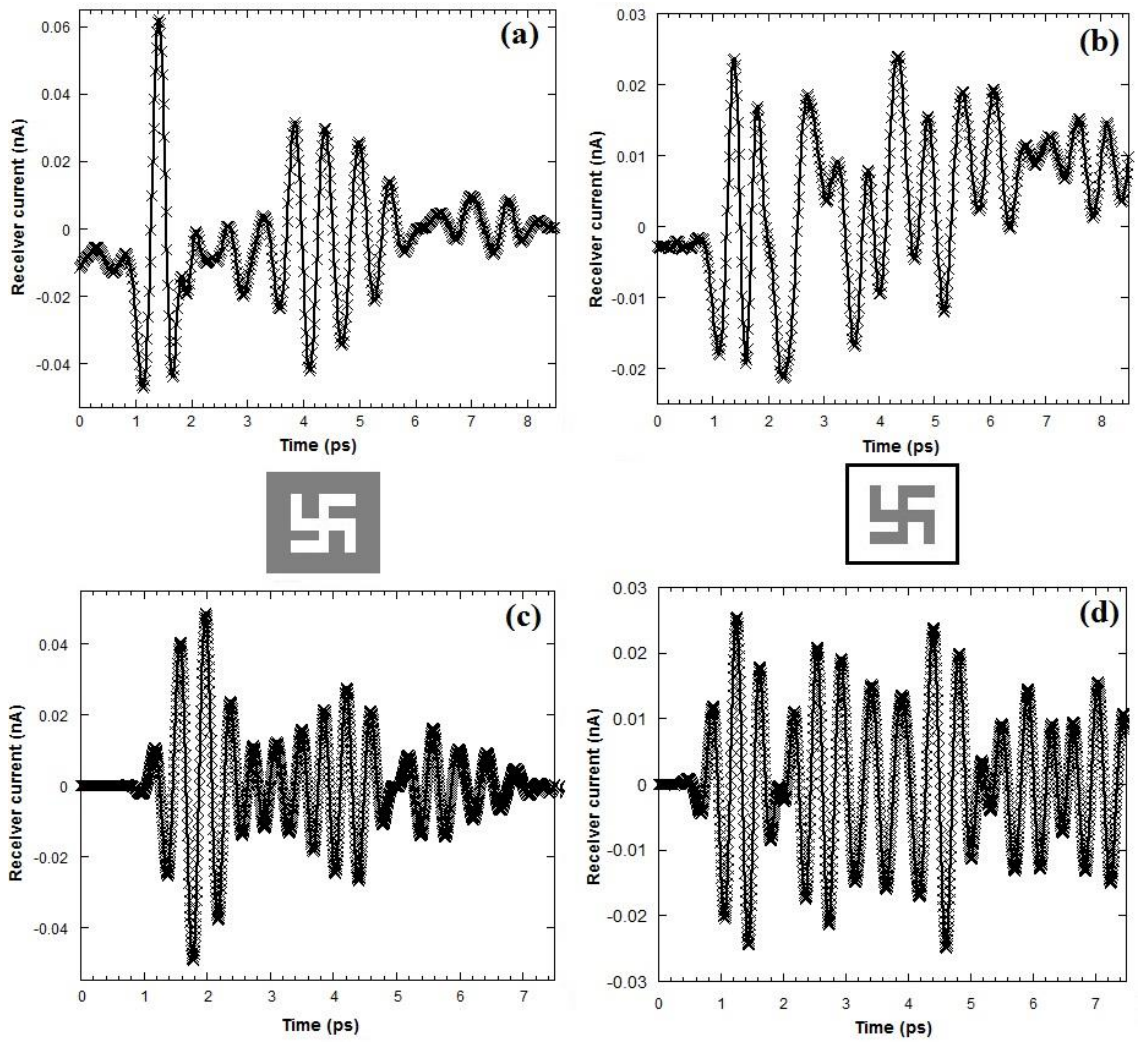

Fig 6.3: Transmitted electric field components polarised perpendicular to the incident radiation through the samples set at azimuthal angle of either polarised 0 (line trace) or 90 (cross trace) degrees. (a) and (c) are respectively the measured and simulated fields of gammadions with aluminium metal outside the patterns. (b) and (d) are respectively the measured and calculated fields of gammadions with aluminium metal on the patterns.

For both measurement and calculation, the transmitted electric field through both samples at azimuthal positions, 0^o and 90^o in figure 6.3 (a) and (c) respectively, show signals with the same amplitude and no phase shift. This means that the gammadions exhibits circular birefringence and $t_{xy} \neq t_{yx}$, as expected. The transmission matrix for these four-fold symmetry structures can be written as

$$T(\omega) = \begin{pmatrix} t_{xx} & t_{xy} \\ -t_{xy} & t_{xx} \end{pmatrix}, \qquad (1)$$

this transmission matrix has opposite and equal off-diagonal components; $t_{yx} = -t_{xy}$ and $t_{xx} = t_{yy}$ which means that our structures exhibits circular birefringence due to the gammadion geometry and the presence of the substrate.

To characterise the optical activity we used the data in figure 6.2 to calculate the polarisation rotation angle θ (Eq 7) and the circular dichroism (CD) (Eq 11 (a)). These quantities are defined in chapter 4. Figure 6.4 shows the spectrum of the measured rotation angle and circular dichroism for both gammadion structures.

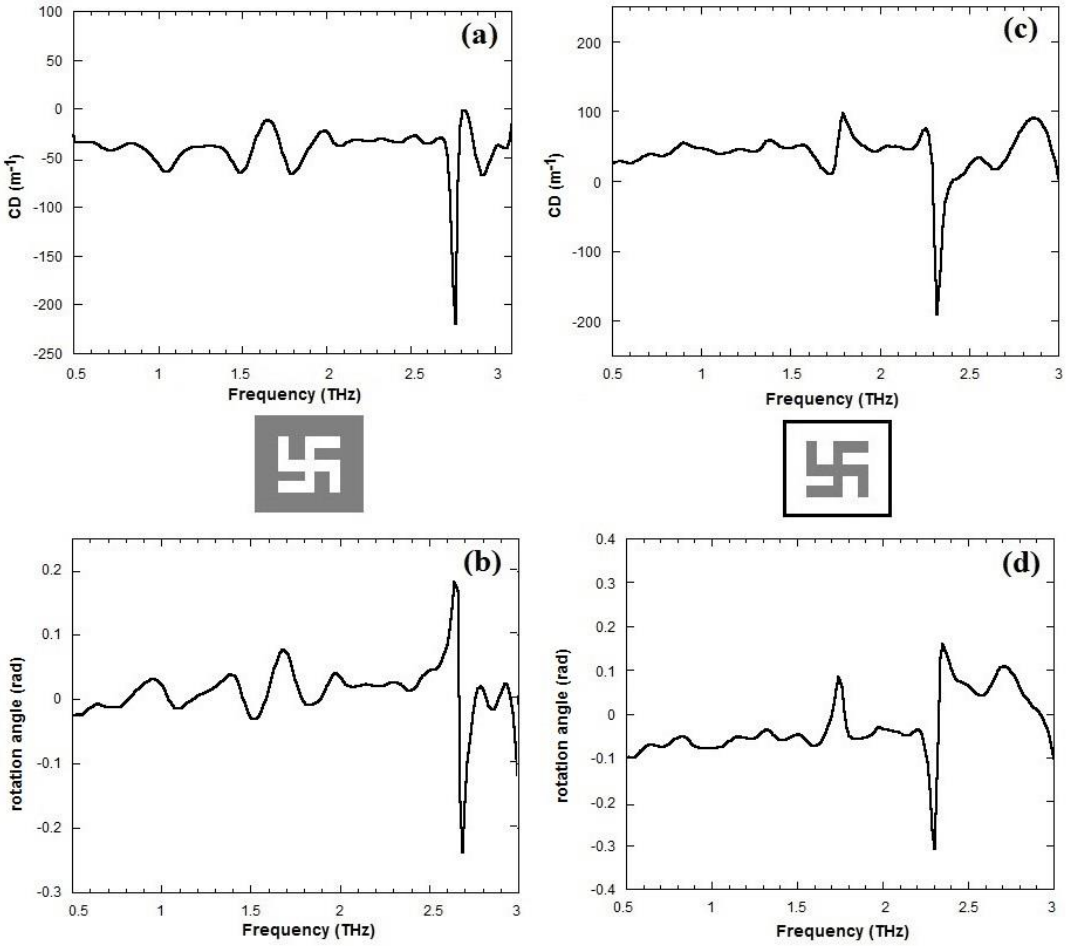

Fig 6.4: (a) and (b) are respectively the spectra of the measured rotation angle and CD for gammadions with aluminium metal outside the patterns. (c) and (d) are the spectra of the measured rotation angle and CD for gammadions with aluminium metal on the patterns

In figure 6.4 (a), the CD spectra of the gammadion with aluminium metal outside the patterns, shows a pronounced frequency dependence in the range between 1 THz and 3 THz with a strong deep at ~ 2.6 THz with a value of 240 m^{-1} and a small peak at 1.6 THz. The CD spectra in figure 6.4 (c) of the second structure (aluminium deposited on the gammadion patterns) shows the same features as the first sample but the strongest resonance is at a

different frequency ~ 2.3 THz with a value of 260 m^{-1}. The spectra of the rotation angle in figure 6.4 (b) of the gammadion with aluminium metal outside the patterns shows features at 1.6 THz and 2.6 THz, the first of which corresponds to the strongest resonance found in the CD spectra for the same structure. In figure 6.4 (d), the spectra of the rotation angle of the gammadion with aluminium metal outside the patterns shows the same frequency dependence as the first structure with a different frequency for the strongest resonance ~ 2.3 THz. We notice also from figure 6.4 that the frequencies resonance for both gammadion structure are in the region where the pile-of-plates polarisers work perfectly as shown in figure 3.2, which means that these frequencies are independent of the polarisers.

To validate the experimental rotation angle and circular dichroism spectra, we simulated the propagation of the linearly polarised incident light to characterize the transmission through the samples and then extracted the spectra of the rotation angle and the circular dichroism. Figure 6.5 presents the calculations.

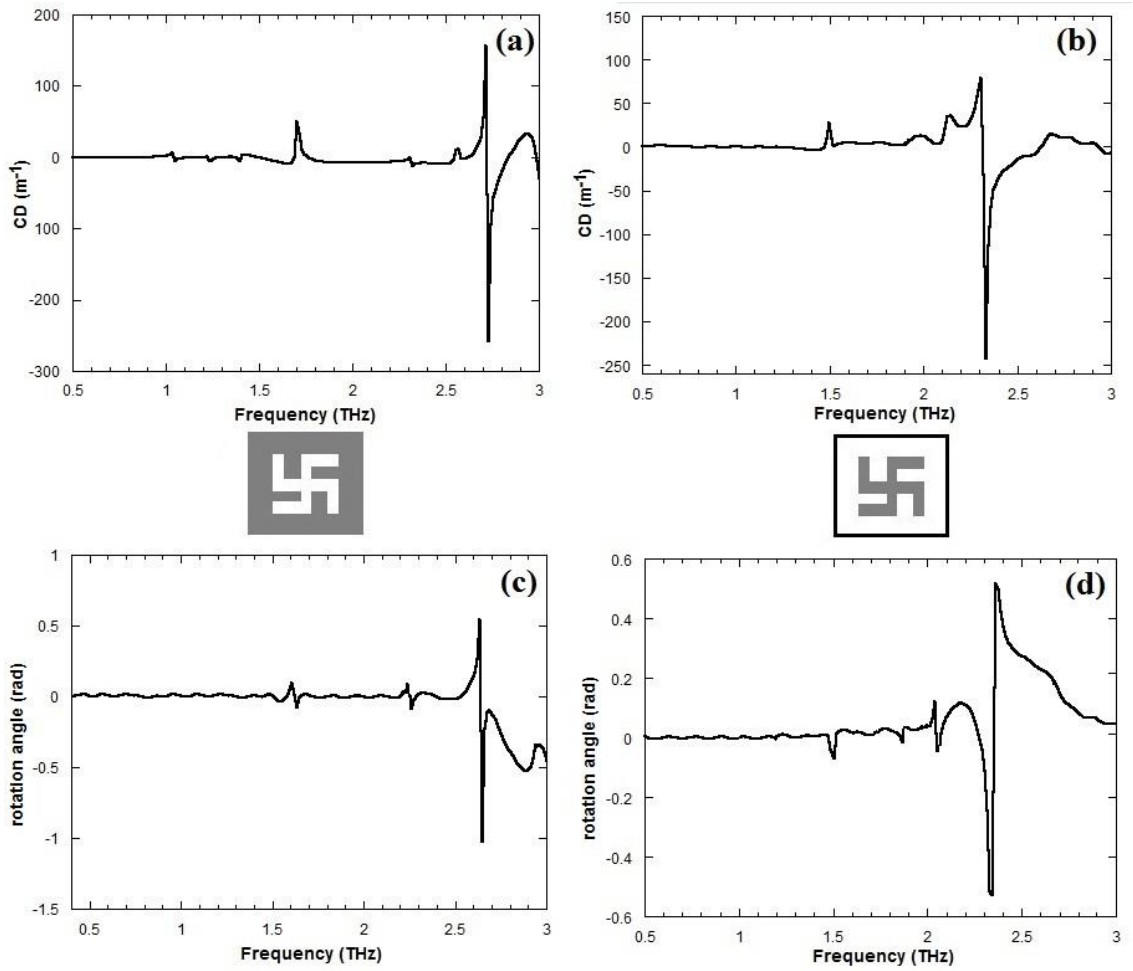

Fig 6.5: (a) and (b) are respectively the spectra of the calculated rotation angle and CD for gammadions with aluminium metal outside the patterns. (c) and (d) are the spectra of the calculated rotation angle and CD for gammadions with aluminium metal on the patterns.

As shown in figures 6.5 (a) and (d), there is a strong resonance in the CD spectra near 2.6 THz and 2.3 THz for the gammadion with aluminium outside and on the patterns respectively, and another small peak at ~ 1.6 THz for both structures, which is in a good agreement with the resonances found in the measured CD spectra shown in figures 6.4 (a) and (c). The spectra of the rotation angle are also similar in experiment and calculation. These results support the hypothesis that this resonance might come from the surface plasmon dispersion of the uniform aluminium and grating period which depend on the detailed shapes of the structures [21].

In order to calculate the resonance frequency resonance of a gammadion, we used a coupled RLC model shown in figure 6.6. In this model, each gammadion in one unit lattice is represented by an equivalent LC circuit resonator [24].

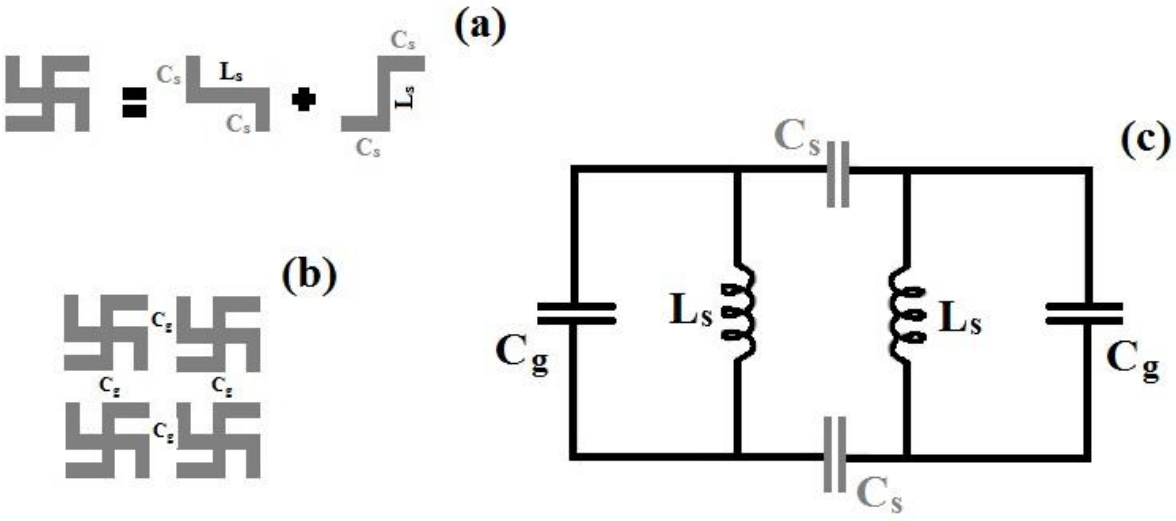

Fig 6.6: The pair of crosses gammadion structure and an equivalent LC model. (a) Schematics of the equivalent LC model for a pair of crosses gammadion. C_s is the capacitances of the side strips and L_s is the inductances of the central strips. (b) Schematics of pair of crosses gammadion arrays and C_g represents the of the gap between the cells. (c) Equivalent LC circuit.

A gammadion can be considered as a combination of an inductance L_s shared by two resonators which are distinguished by separate capacitances C_s and C_g, where L_s is the inductance of the central strips, C_s is the capacitance of the side strips and C_g is the gap capacitance between neighbouring unit lattices [24]. The capacitive coupling between gammadion can play a considerable role in enhancing the effective chirality parameter. To understand this effect, we considered two cases. In the first case the width of the gap g is similar to the line width w. In that case the capacitance C_g is much smaller than the capacitance C_s as the surface of the metallic area facing each other in C_g is smaller than the

ones in C_s, which means that we can ignore the contribution of the capacitance C_g to the current induced in the central lines. The second case is where the gap is smaller or equal to the thickness (t) of the gammadion metal. In that case the capacitance C_g can be equal or larger than the capacitance C_s. Therefore, more charge can be accumulated in the gap capacitance which will allow the flow of more current in the central lines. As a result, by reducing the width of the gap between metallic lines in neighbouring unit cells, we can improve the optical activity of a metamaterial [24]. By using a coplanar strip capacitance formula [31], the gap capacitance C_g can be evaluated as follows

$$C_g \approx \varepsilon_0 \varepsilon_r \left[1.15\left(\frac{2t}{g}\right) + 2.80\left(\frac{2w}{g}\right)^{0.22} \right] l, \tag{2}$$

where ε_0 is the permittivity of the vacuum, ε_r is the relative permittivity of the substrate, t and w and l are respectively the thickness, the width and the effective length of the strips.

The resonance frequency for the pair of crosses gammadion structure can be deduced from the equivalent RLC circuit in figure 6.6 (c) and its expression is then as follow

$$f = \frac{1}{2\pi}\sqrt{\frac{1}{L_s(C_s + C_g)}}. \tag{3}$$

The value of the resonance frequency of our planar gammadion structure is then f = 2.35 THz which is in a good agreement with the measured and the calculated spectra of the circular dichroism and the rotational angle in figure 6.4 and figure 6.5.

To examine the relationship between the optical activity and the width of the gap between gammadions in neighbouring unit cells, we calculated the rotation angle with different width of gap (g = 20, 40, and 60 μm) for the structure with metal deposited on the gammadion patterns as shown in figure 6.7.

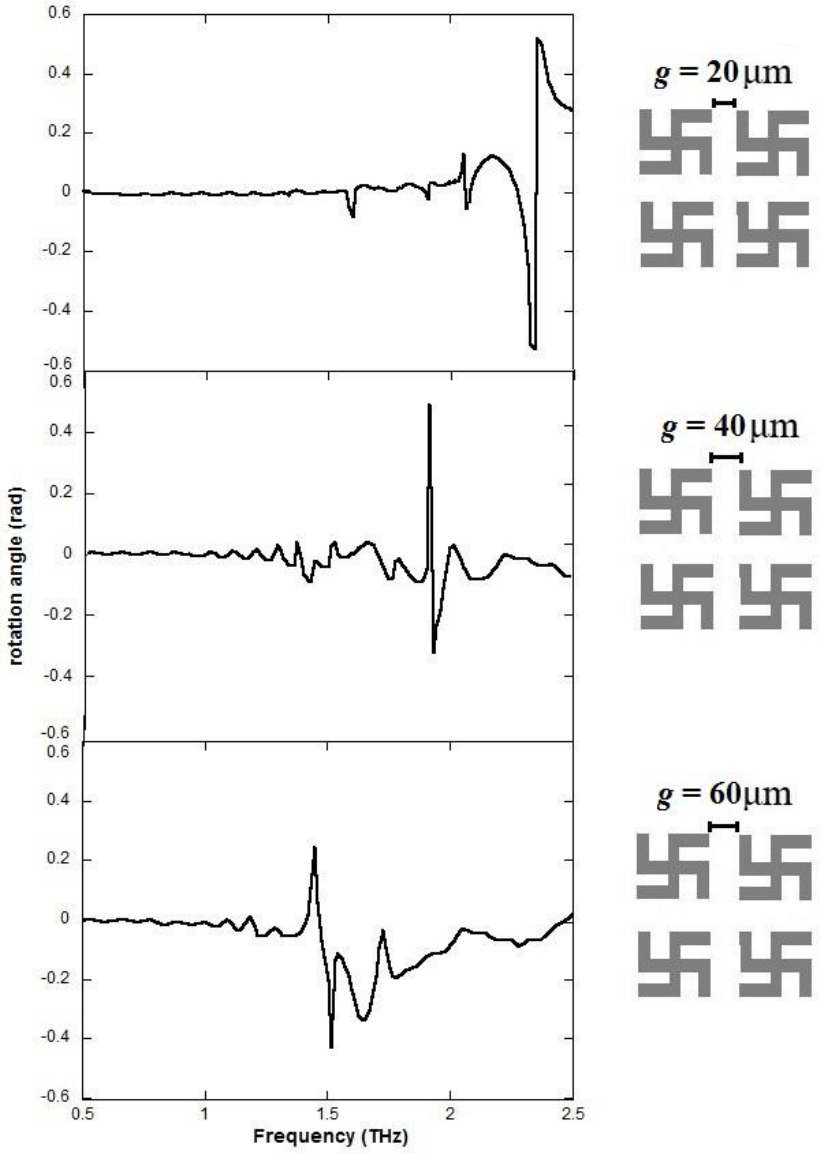

Fig 6.7: Dependence of the rotation angle spectrum on the gap between gammadions. Schematics of the samples are shown on the right.

It is clear from the rotation angle spectra shown in figure 6.7 that the resonance frequency shifts with the variation in the gap g and increases with decreasing g. This means that the strong resonances observed in the rotation angle spectra of the planar structure depend essentially on the inter-structure coupling C_g since the capacitance of the side strips is independent of the gap width g. The rotation angle spectra of the three planar structures in figure 6.7 also shows also that the magnitude of the rotation angle changes with the gap width and becomes larger with smaller width of the gap between neighbouring unit cells. As a result, optical activity is mainly determined by the frequency arising from the surface plasmon dispersion of the uniform aluminium and grating period. Moreover the optical activity exhibited by our planar chiral structures is enhanced by reducing the width of the gap g.

6.4 Conclusion

In this chapter we experimentally and computationally studied gammadion arrays where the deposition of the aluminium metal is different; one of the structures has the metal on the gammadion patterns and the second structure has the metal outside the gammadion. The results of the circular dichroism and the rotation angle, have shown a strong frequency dependence on the spectra which is due to the inter-structure coupling referring to the coupling between the metallic lines of the gammadion in neighbouring unit cells. This means that the optical activity exhibited by the gammadion structures is originated from the resonance frequency of the dispersion of the metallic surface and the gap between the unit cells and that the gap width g applies an important role in the control of the enhancement of this optical activity.

References

1. Zhao R., Zhang L., Zhou J., Koschny Th., and Soukoulis C.M., *Conjugated gammadion chiral metamaterial with uniaxial optical activity and negative refractive index.* Physical Review B, 2011. **83**: p. 035105.

2. Decker M., Zhao R., Soukoulis C.M., Linden S., and Wegener M., *Twisted split-ring-resonator photonic metamaterial with huge optical activity.* Optics Letters, 2010. **35**(10): p. 1593-1595.

3. Decker M.,Ruther M., Kriegler C.E., Zhou J., Soukoulis C.M., Linden S., and Wegener M., *Strong optical activity from twisted-cross photonic metamaterials.* Optics Letters, 2009. **34**(16): p. 2501-2503.

4. Jaggard D.L, and Engheta N., *Chirosob TM as an invisible medium.* Electron. Lett., 1989. **25**: p. 173.

5. Svirko Y., Zheludev N., and Osipov M., *Layered chiral metallic microstructures with inductive coupling.* Applied Physics Letters, 2001. **78**(4): p. 498-500.

6. Gennady S., *Optical polarizer/isolator based on a rectangular waveguide with helical grooves.* Applied Physics Letters, 2006. **89**(14): p. 141127.

7. Yen T. J., Padilla W.J., Fang N., Vier D.C., Smith D.R., Pendry J. B., Basov D.N., and Zhang X., *Terahertz magnetic response from artificial materials.* Science, 2004. **303**(5663): p. 1494-6.

8. Padilla W.J., Taylor A.J., and Averitt R.D., *Dynamical Electric and Magnetic Metamaterial Response at Terahertz Frequencies.* Physical Review Letters, 2006. **96**(10): p. 107401.

9. Chen H.-T., Padilla W.J., Cich Michael J., Azad Abul K., Averitt Richard D., and Taylor Antoinette J., *A metamaterial solid-state terahertz phase modulator.* Nature Photonics, 2009. **3**(3): p. 148-151.

10. Chen H.-T., O'Hara John F., Azad Abul K., Taylor Antoinette J., Averitt Richard D., Shrekenhamer David B., and Padilla W.J., *Experimental demonstration of frequency-agile terahertz metamaterials.* Nature Photonics, 2008. **2**(5): p. 295-298.

11. Zhang S., Park Y.-S., Li J., Lu X., Zhang W., and Zhang X., *Negative Refractive Index in Chiral Metamaterials.* Physical Review Letters, 2009. **102**(2): p. 023901.

12. Dolling G., Wegener M., Soukoulis C.M., and Linden S., *Negative-index metamaterials at 780 nm wavelength.* optics Letters, 2007. **32**: p. 53-55.

13. Yao J., Liu Z., Liu Y., Wang Y., Sun C., Bartal G., Stacy Angelica M., and Zhang X., *Optical Negative Refraction in Bulk Metamaterials of Nanowires.* Science, 2008. **321**: p. 930.

14. Smith D.R., Padilla W.J., Vier D.C., Nemat-Nasser S.C., and Schultz S., *Composite Medium with Simultaneously Negative Permeability and Permittivity.* physical Review Letters, 2000. **84**: p. 4184-4187.

15. Pendry J.B., *A Chiral Route to Negative Refraction.* Science, 2004. **306**: p. 1353-1355.

16. Monzon C., and Forester D., *Negative Refraction and Focusing of Circularly Polarized Waves in Optically Active Media.* Physical Review Letters, 2005. **95**(12): p. 123904.

17. Papakostas A., Potts A., Bagnall D., Prosvirnin S., Coles H., and Zheludev N., *Optical Manifestations of Planar Chirality.* Physical Review Letters, 2003. **90**(10): p. 107404.

18. Vallius T., Jefimovs K., Turunen J., Vahimaa P., and Svirko Y., *Optical activity in subwavelength-period arrays of chiral metallic particles.* Applied Physics Letters, 2003. **83**(2): p. 234.

19. Kuwata-Gonokami M., Saito N., Ino Y., Kauranen M., Jefimovs K., Vallius T., Turunen J., and Svirko Y., *Giant Optical Activity in Quasi-Two-Dimensional Planar Nanostructures.* Physical Review Letters, 2005. **95**(22): p. 227401.

20. Bai B., Svirko Y., Turunen J., and Vallius T., *Optical activity in planar chiral metamaterials: Theoretical study.* Physical Review A, 2007. **76**(2): p. 023811.

21. Kanda N., Konishi K., and Kuwanta-Gonokami M., *Terahertz wave polarization rotation with double layered metal grating of complimentary chiral patterns.* Optics Express 2007. **15**: p. 11117.

22. Konishi K., Nomura M., Kumagai N., Iwamato S., Arakawa Y., and Kuwata-Gonokami M., *Circularly Polarized Light Emission from Semiconductor Planar Chiral Nanostructures.* Physical Review Letters, 2011. **106**(5): p. 057402.

23. Decker M., Klein M.W., Wegener M., and Linden S., *Circular dichroism of planar chiral magnetic metamaterials.* optics Letters, 2007. **32**(7): p. 856-858.

24. Kim T.T., Oh S.S., Park H.S., Zhao R., Kim S.H., Choi W., Min B., and Hess O., *Optical activity enhanced by strong inter-molecular coupling in planar chiral metamaterials.* Sci Rep, 2014. **4**: p. 5864.

25. Wang B., Zhou J., Koschny T., Kafesaki M., and Soukoulis Costas M., *Chiral metamaterials: simulations and experiments.* Journal of Optics A: Pure and Applied Optics, 2009. **11**: p. 114003.

26. Plum E., Zhou J., Dong J., Fedotov V., Koschny T., Soukoulis C.M., and Zheludev N., *Metamaterial with negative index due to chirality.* Physical Review B, 2009. **79**(3): p. 035407.

27. Zhou J., Dong J., Wang B., Koschny T., Kafesaki M., and Soukoulis C.M., *Negative refractive index due to chirality.* Physical Review B, 2009. **79**(121104).

28. Li Z., Mutlu M., and Ozbay E., *Chiral metamaterials: from optical activity and negative refractive index to asymmetric transmission.* Journal of Optics, 2013. **15**(2): p. 023001.

29. Xiong X., Sun W.-H., Bao Y.-J. Bao, Peng R.-W., Wang M., Sun C., Lu X., Shao J., Li Z.-F. Li, and Ming N.-B., *Construction of Chiral Metamaterial with U-Shaped Resonator.* phys. rev. B, 2010. **81**(7): p. 075119.

30. Kenanakis G., Zhao R., Stravrinidis A., Konstantinidis G., Katsarakis N., Kafesaki M., Soukoulis C.M., and Economou E.N., *Flexible chiral metamaterials in the terahertz regime: a comparative study of various designs.* Optical Materials Express, 2012. **2**(12): p. 1702-1712.

31. Sakurai T., and Tamaru K., *Simple Formulas for Two- and Three-Dimensional Capacitances.* IEEE Transactions on Electron Devices, 1983. **30**(2): p. 183-185.

Chapter 7

THz Time-Domain Investigation of Optical Activity in quasi 2D and 3D Chiral Metamaterials

7.4 Introduction

The study of optical activity phenomena and the manipulation of electromagnetic waves by the use of artificially engineered chiral metamaterials has lately generated a lot of interest and resulted in many intriguing applications [1-7]. Metamaterials can exhibit unusual electromagnetic properties such as negative refraction [8] when the difference between the refractive index of the left-hand n_L and the right-hand n_R circularly polarised light is large. Materials exhibiting negative index (negative permeability and permittivity) also called left-handed media usually consist of continuous wires and concentric rings with gaps called also split-ring resonators [9-12]. Three-dimensional chiral metamaterials with strong optical activity are also candidates for achieving negative refractive index [13-15] in the far-infrared. Recently, 3D chiral metamaterial with negative refractive index working at THz regime was also demonstrated [2] and it was reported that even planar chiral structures can exhibit optical activity [16-19].

In recent years, there have been an explosion of interest to the properties of electromagnetic waves propagating through planar chiral structures [20]. The first experimental investigations were performed by Papakostas et al [16, 21] and they demonstrated that planar chiral media could affect the polarisation state of light in a similar way to 3D chiral structures. Their experiments were carried out using a range of fabricated nanoscale planar chiral structures etched in Ti/Au silica substrate. The results demonstrated also that when the linearly polarised light is transmitted through arrays of these planar chiral structures, its polarisation changes and becomes elliptical and that the degree and the direction of the polarisation rotation was associated with the chirality of the structure element shape. However, the process behind the optical activity exhibited by these planar chiral structures is not totally understood. Spectroscopic measurements revealed that optical activity can be enhanced by exciting surface plasmons [18]. A giant optical activity in two parallel layers of planar metal rosette patterns rotated with respect to each other was demonstrated, the two layers were not connected as in 3D chiral materials [2, 22, 23] but can be coupled electromagnetically. Later, various chiral metamaterials consisting of more than two layers of planar structures were investigated [4, 24-28].

In this work, we present a design of a two-dimensional and a three-dimensional chiral material for terahertz frequencies, which consist of square arrays of metallic Archimedean spirals with four-fold symmetry. To examine the optical activity exhibited by these chiral metamaterials, we measured and simulated the transmitted THz electric field through the samples.

7.2 Sample fabrication

The two-dimensional chiral material is based on a periodic square array of four-fold symmetry unit cells on a high resistivity silicon substrate of 650 µm thickness. Each cell contains four spirals rotated by 90° to each other to ensure four-fold symmetry. The four planar metallic spirals are constructed such that the radius is $R = R_0 e^{\theta}$ where $R_0 / R_{\max} = 0.5$ and θ_{max} = 1.05 x 360°. The spirals have a linewidth of 6.00 µm and are spaced by 26 µm. The 100 µm x 100 µm cells are arranged in a 200 x 200 lattice with period P=100 µm. A chip of 20 mm wide patterns is larger than the THz beam size of ~ 15 mm. Figure 7.1 shows a schematic diagram of the arrangement of spiral elements.

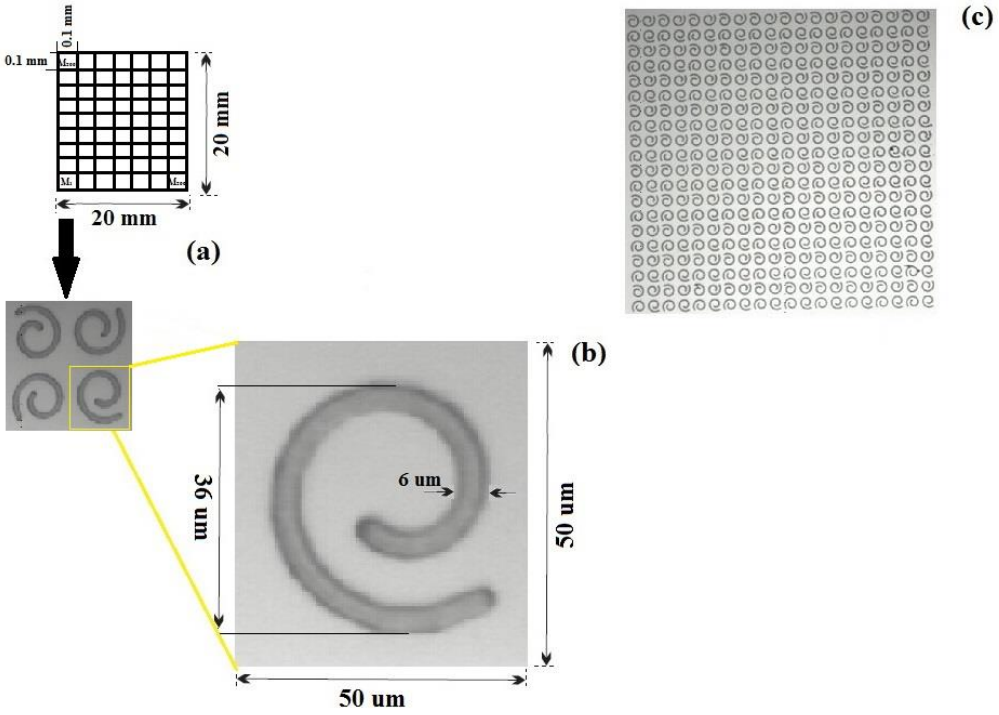

Fig 7.1: (a) Schematic diagram of the unit cell and its arrangement in the chip. (b) Image of a single spiral with dimensions. (c) Microscope image of the array of planar chiral spirals.

The 2D chiral structure was manufactured by using standard lithography and lift-off techniques. A thin, uniform coating of positive photoresist (S1813) at 6000 rpm for 30 seconds were applied to a high resistivity Si substrate (15 kΩ/cm), and then baked to harden the resist and improve adhesion. Exposure of the spiral pattern was performed using a laser writer for a maximum resolution and to avoid uneven exposure due to poor mask contact. The power of the laser was 22 mW at 40 % and the filter of the laser on. Exposure and development were followed by a remove of oxide layers from the sample surface to improve the metal adhesion, and metallisation using a thermal evaporator. A 200 nm thick aluminium (Al) film was deposited and then the chip was immersed in acetone at room temperature to enable metal lift-off. Figure 7.2 shows a schematic view of the fabrication process.

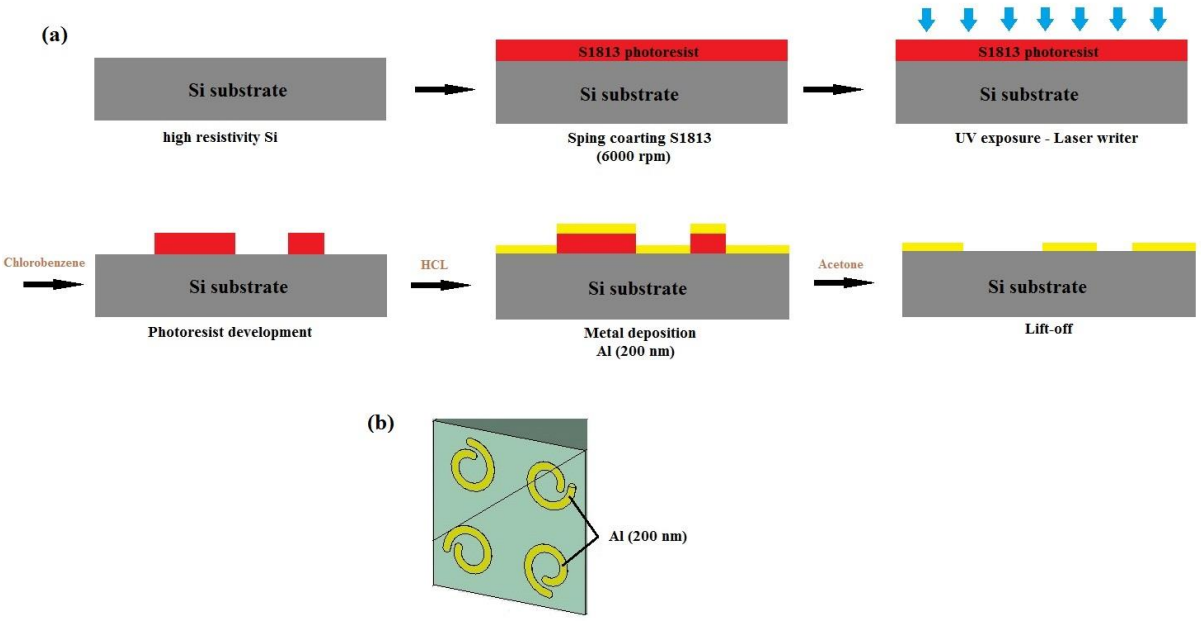

Fig 7.2: (a) Schematic diagram of the fabrication process of the array of planar spirals. (b) Schematic side view of one unit cell of the fabricated sample.

To eliminate the effect of substrate asymmetry, we also made a sample with a piece of high resistivity silicon wafer identical to the substrate, and stuck on the patterned side of the structure.

A “three-dimensional” sample was produced using the same lithography design as the 2D spiral arrays. The difference is that the spirals were defined in a SU8-50 photoresist and the aluminium metal was deposited over whole structure except for the edge of the spirals. The SU8 is a negative resist so that the exposed region remains after developing the sample. The photoresist SU8-50 was diluted using EC solvent so as to achieve a 10 μm thick layer

after spin coated at 6000 rpm onto a high resistivity Si substrate. The exposure of the pattern was performed using the laser writer. After the exposure, the sample was baked for 5 min at 65ºC and 10 min at 95ºC and developed in EC solvent for 5 min. The development of the chip was followed by deposition of 200 nm of aluminium using a thermal evaporator. A schematic of the fabrication process, an image of the chiral structure obtained with a scanning electronic microscope and a schematic of the structure are shown in figure 7.3.

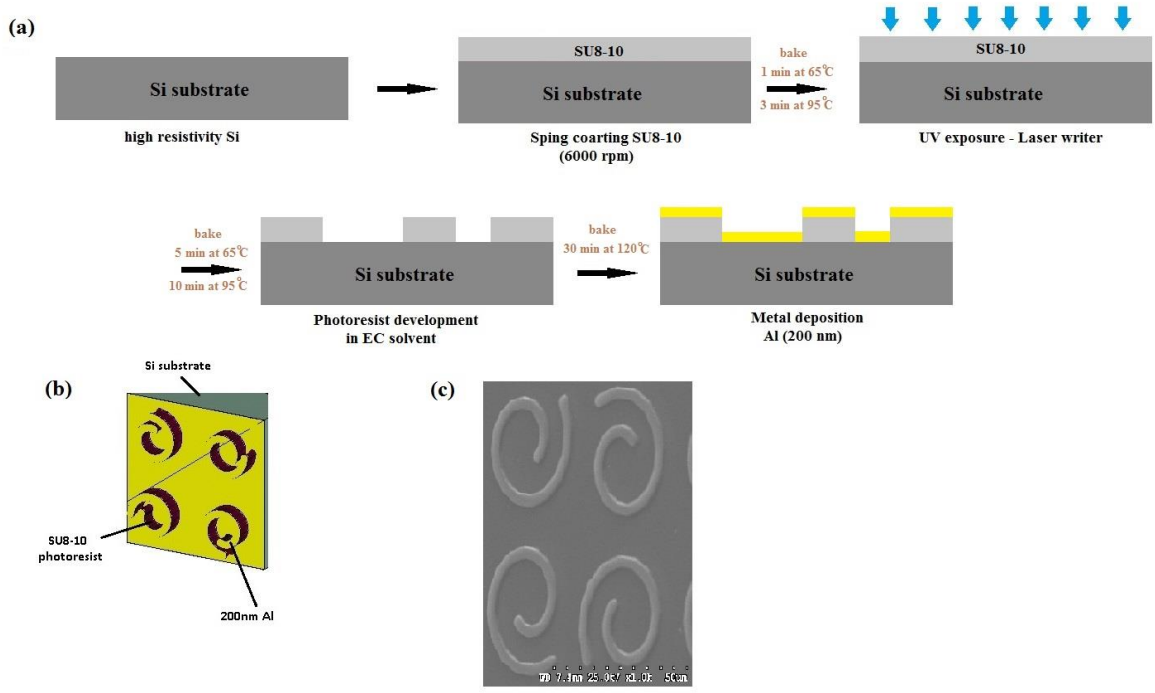

Fig 7.3: (a) Schematic diagram of the fabrication process of the "3D" spiral array. (c) Schematic view of a unit cell. (c) Scanning electron microscope image.

7.3 Experimental and computational results

Polarised transmission experiments were carried out using the THz Time-Domain Spectroscopy (TDS) setup described in Chapter 4. Computer simulations were performed using the commercial software package (CST Microwave Studio). The dimensions of the Al spirals and the Si substrate matched physically with the ones employed in the experiments and the optical response of the Al metal was described by the Drude model of the dielectric function which is given by [29]

$$\varepsilon_c = \varepsilon^{'} - \frac{\omega_p^2}{\omega^2 + i\omega\omega_\tau} \quad (1)$$

where ω_p and ω_τ are respectively the plasma frequency and the damping frequency, and have units of cm^{-1}. The plasma frequency and the damping frequency are defined respectively as follow

$$\omega_p = \frac{1}{2\pi c}\sqrt{\frac{4\pi N e^2}{m^*}}, \quad \text{(a)}$$

and (2)

$$\omega_\tau = \frac{1}{2\pi c\,\tau}, \quad \text{(b)}$$

where c is the speed of light in vacuum, N is the free electron density, e is the electronic charge, m^* is the effective mass of electrons and τ is the electron lifetime in seconds. The plasma angular frequency and the damping frequency of aluminium used in the simulation are given respectively by $\omega_p = 2.24 \times 10^{16}$ rad/s and $\omega_\tau = 1.24 \times 10^{14}$ Hz [29].

7.3.1 Quasi-2D structure

To examine the anisotropy of the sample, we performed two different transmission measurements using method 1. The first measurement was made by setting the sample at one azimuthal position called 0° and the second measurement by rotating the sample about the normal to the plane by 90° relative to the first position. Figure 7.4 shows time-domain traces of the transmitted electric field components for the quasi-two dimensional planar structure with the Si substrate on one side and the quasi-2D planar structure with Si substrate on both sides, after subtracting the reference signal of the transmitted electric fields components through a bare Si substrate.

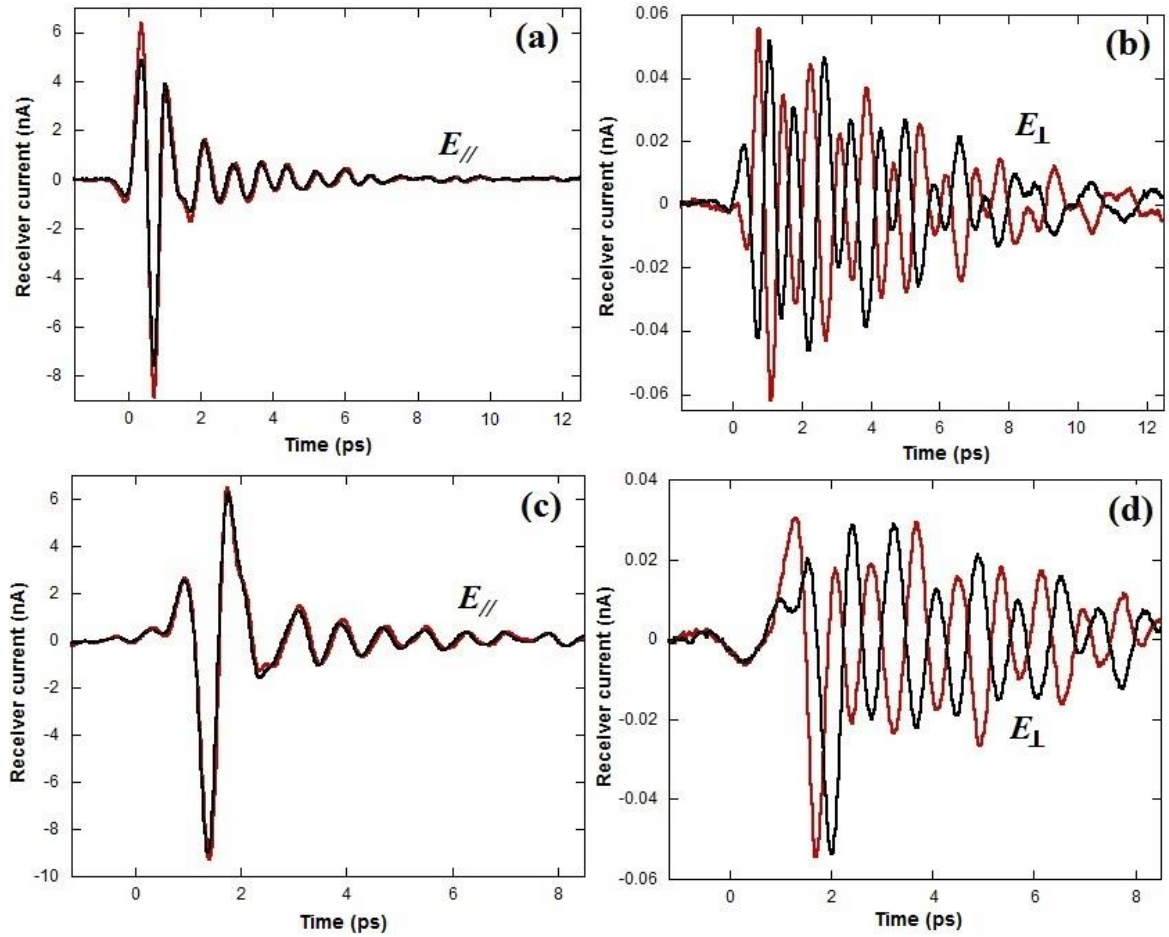

Fig 7.4: Time-domain measurements of the electric field transmitted through: (a) and (b) the quasi-2D array of spirals with Si substrate on one side, and (c) and (d) the quasi-2D array of spirals with Si substrate on both sides. Both samples were set at azimuthal axes of 0° (red) and 90° (black).

We can observe from figures 7.4 (a) and (c) that the co-polarised transmitted electric fields overlap for both azimuthal positions of the samples (0° and 90°). This can be explained by the fact that the chirality of the grating is very small and is usually observed only in the cross-polarised transmission as shown in figures 7.4 (b) and (d). We notice from these latter figures a pronounced transmitted component of the electric field polarised perpendicular to the incident radiations for both azimuthal positions of the planar structures but they are π out of phase for the two azimuthal positions. This is different than what we expected as the spiral structures have a four-fold symmetry around *z*. To confirm this behaviour, we calculated the electric field component polarised perpendicular to the incident radiation and transmitted through three different samples: the structure with the Si substrate on one side, the structure with Si substrate on both sides and an array of spirals with no four-fold symmetry as shown in figure 7.5.

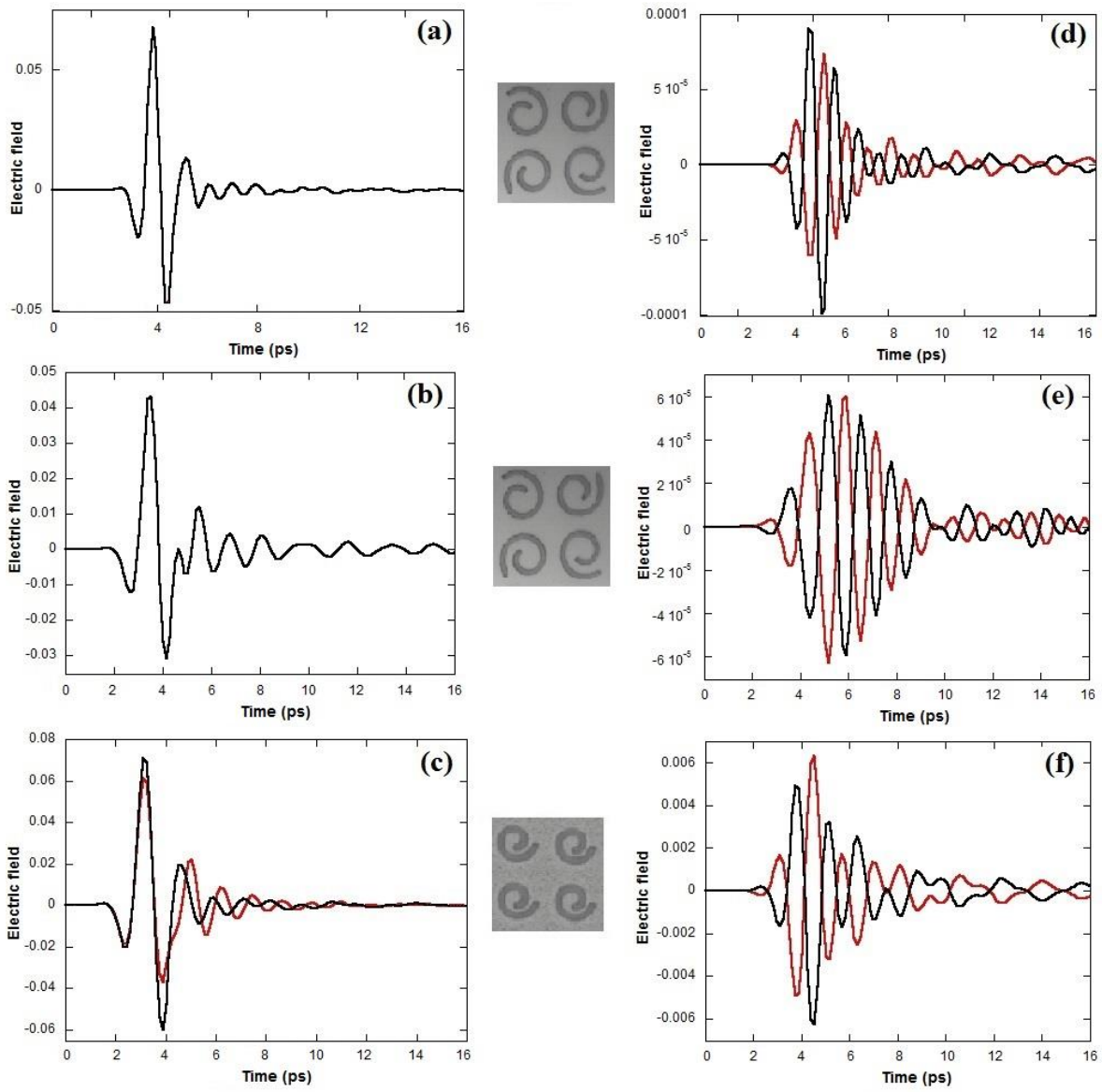

Fig 7.5: Calculated electric field components polarised parallel (left hand panels) and perpendicular (right hand panels) to the incident polarisation and transmitted through: (a) and (d) the 2D array of four-fold symmetry spirals with Si substrate on one side, (b) and (e) the same array with Si substrate on both sides, and (c) and (f) array of spirals lacking four-fold symmetry. The simulations were made for two azimuthal positions of the samples: 0° (red) and 90° (black).

In figures 7.5 (a) and (b), the calculated co-polarised transmitted fields through the two samples with four-fold symmetry spirals are similar to the experiments shown in figures 7.4 (a) and (c). Figure 7.5 (c) of the calculated co-polarised transmitted electric fields through the array of spirals without the four-fold symmetry shows a different magnitude and a $\pi/2$ phase shift between the two azimuthal positions. The three spiral arras in figures 7.5 (d), (e) and (f) show a pronounced component of the electric field polarised perpendicular to

the incident polarisation. Moreover the amplitude of this transmitted electric field through the three samples has almost the same value and changes sign when the samples are rotated by 90^{o} which is in agreement with experiment in figures 7.4 (b) and (d). We notice also that the amplitude of the cross-polarised transmitted electric fields through the array of spirals lacking four-fold symmetry is 10^3 times bigger than the electric fields transmitted through the two arrays of four-fold symmetry spirals. These results indicate that our structures with nominal four-fold symmetry behave as if they do not have rotational symmetry even through the unit cell and the lattice appears to. Figure 7.6 shows the circular dichroism (CD) and the rotational angle spectra for the two samples with nominal four-fold symmetry.

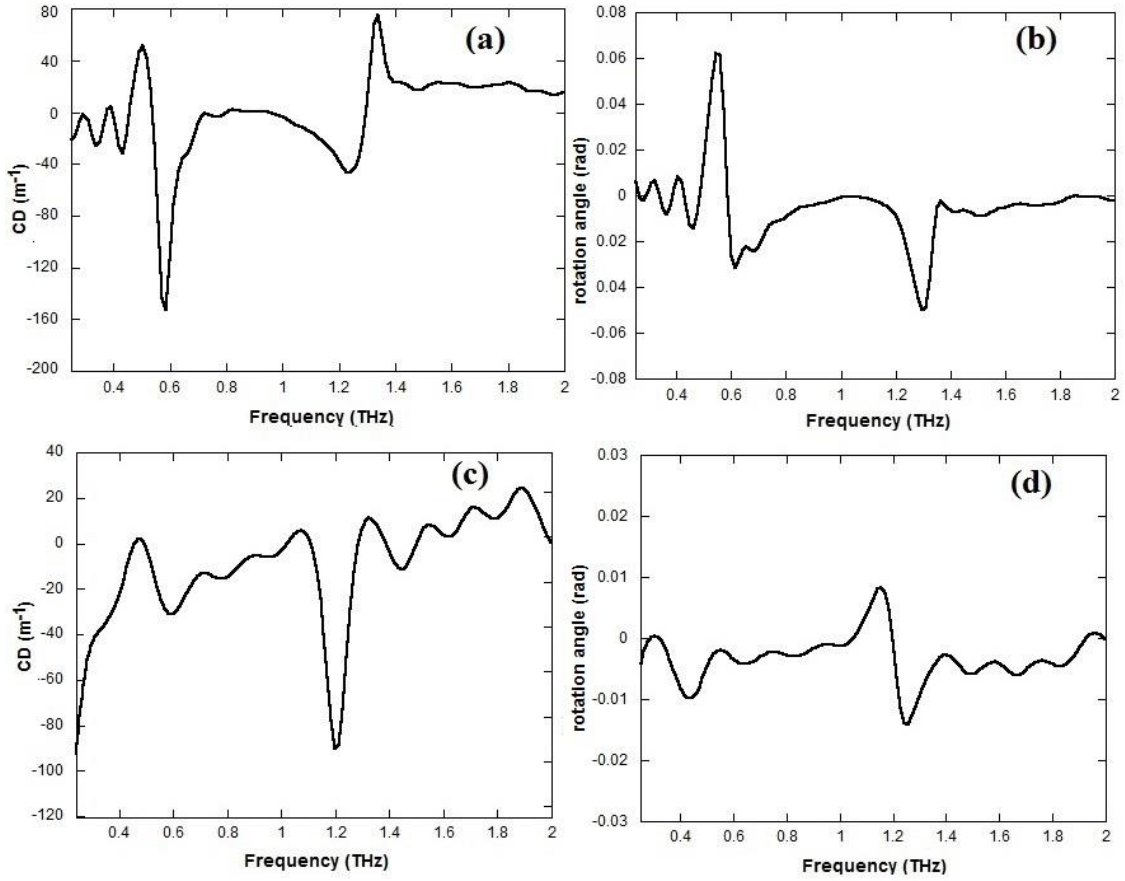

Fig 7.6: (a) and (c) are respectively the spectra of circular dichroism for 2D array of spirals with Si substrate on one side and the 2D array of spirals with Si substrate on both sides. (b) and (d) are the spectra of the rotation angle of the 2D array of spirals with Si substrate on one side and the 2D array of spirals with Si substrate on both sides respectively.

Figure 7.6 (a) shows the circular dichroism spectra for the 2D planar structure with the Si substrate on one side. It shows pronounced resonances at 0.6 THz and ~ 1.2 THz. The 2D planar structure with the Si substrate on both sides shows similar resonances but different shaped CD spectrum (figure 7.6 (c)). The rotation angle spectra in figures 7.6 (b) and (d) show similar resonances for both samples at 0.6 THz and 1.2 THz with a different shaped rotation angle spectrum. To validate the experimental rotation angle and CD spectra, we calculated the CD and the rotation angle spectra for the structure with the Si substrate on one side, the structure with Si substrate on both sides and the array of spirals lacking four-fold symmetry as shown in figure 7.7.

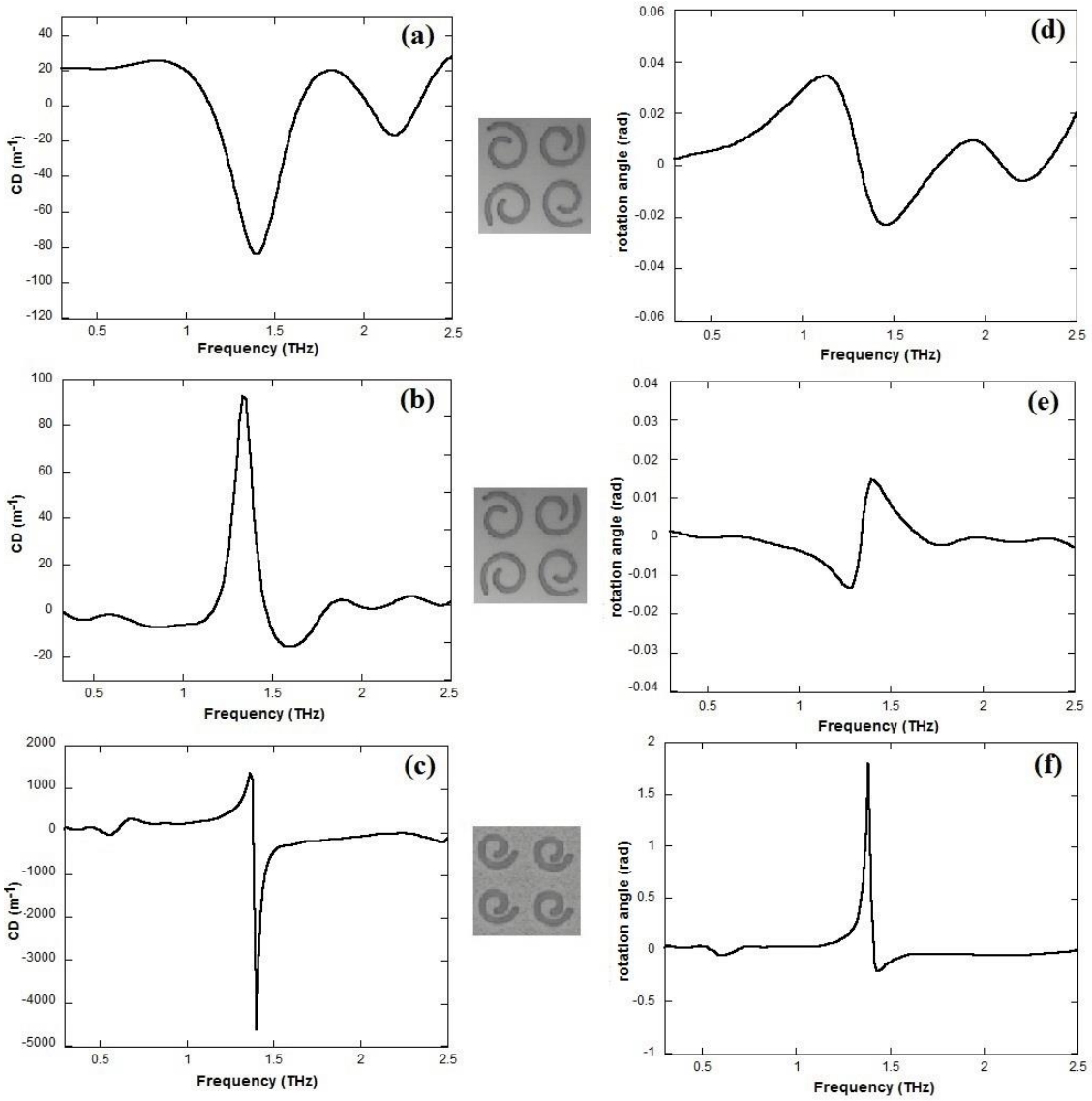

Fig 7.7: The calculated CD (left hand panels) and the rotation angle (right hand panels) spectra respectively for: (a) and (d) the 2D array of four-fold symmetry spirals with Si substrate on one side, (b) and (e) the same array with Si substrate on both sides, and (c) and (f) array of spirals lacking four-fold symmetry.

We can notice from figures 7.7 (a), (b) and (c) that the calculated CD spectra for the three samples show a pronounced resonance frequency at 1.4 THz which coincides with one of the resonances shown in the measured CD spectra in figures 7.6 (a) and (c). Figures 7.7 (d), (e) and (f) for these structures show also the same behaviour, one pronounced resonance at 1.4 THz in the spectrum of the calculated rotation angle which coincides with one of the resonances shown in the measured rotation angle spectra in figures 7.6 (b) and (d). These results confirm that the resonance at 0.6 THz shown in the experiment is probably due to the misalignment of the sample, and that the resonance frequency at 1.4 THz (1.3 THz in experiment) is probably due to the gap g between the spirals, or the radius or the length of the spirals. In order to examine these three hypotheses and determine the origin of the polarisation, we first calculated the rotation angle spectra of the transmitted electric fields for the quasi-2D array of spirals with different width gap (g = 14, 34, and 54 μm) as shown in figure 7.8.

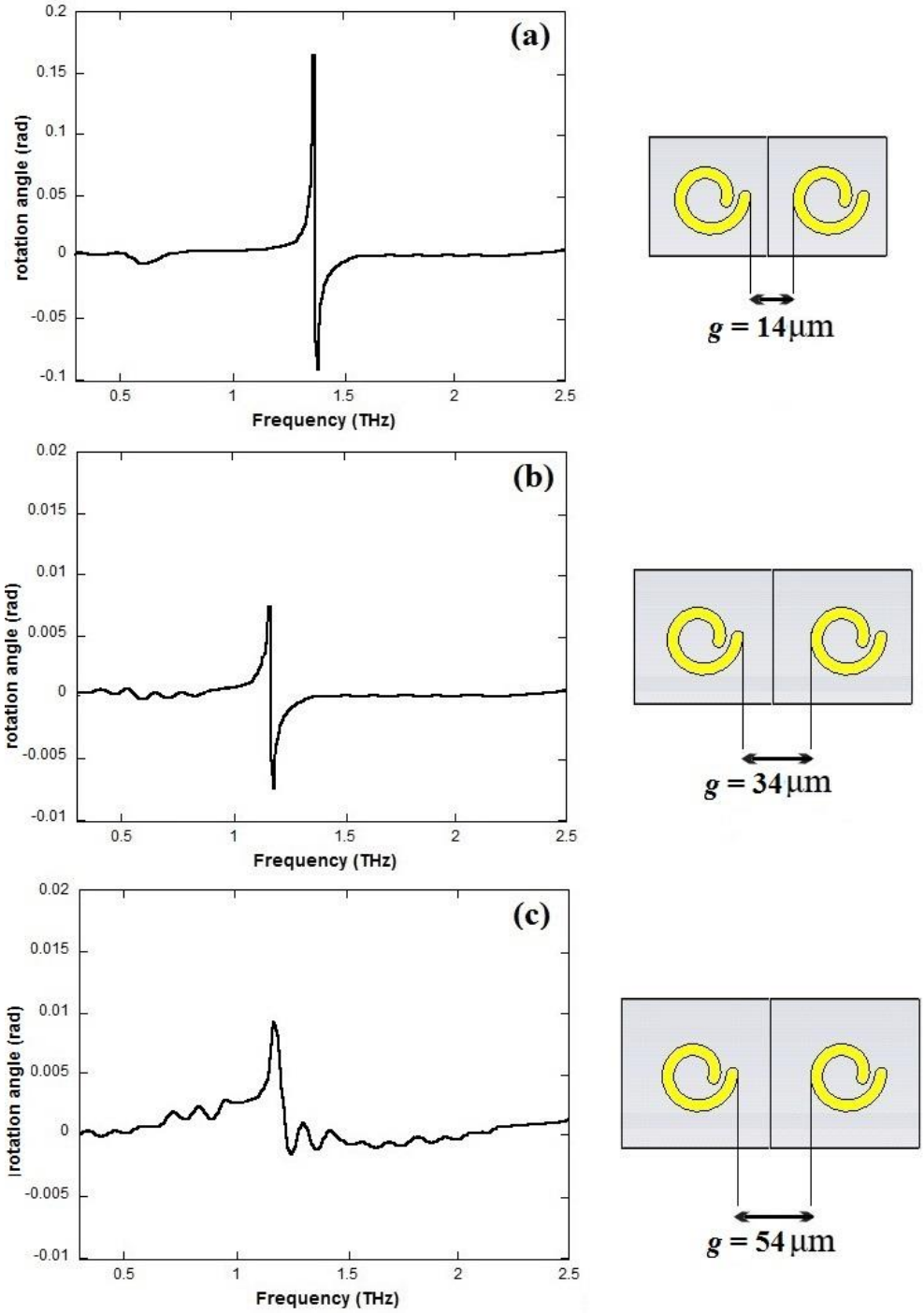

Fig 7.8: (a), (b) and (c) are respectively the rotation angle for the quasi-2D array of spirals with a gap of 14 µm, 34 µm and 54 µm. Schematics of the samples are shown on the right.

The calculated rotation angle spectra in figures 7.8 (b) and (c) shows the same characteristic frequency dependence at ~ 1.2 THz which is different from the resonance frequency in figure 7.8 (a) at 1.4 THz of the sample studied before. We also notice that this resonance increase with decreasing the width gap until a certain distance. It is clear from figure 7.8 that the strong resonance frequency depends on the gap between the spirals.

To examine the second hypothesis of the radius, we performed the same simulations of the rotation angle spectra for different r = R_o/R_{max} (defined before), r = 0.5, 0.4 and 0.3 µm as shown in figure 7.9.

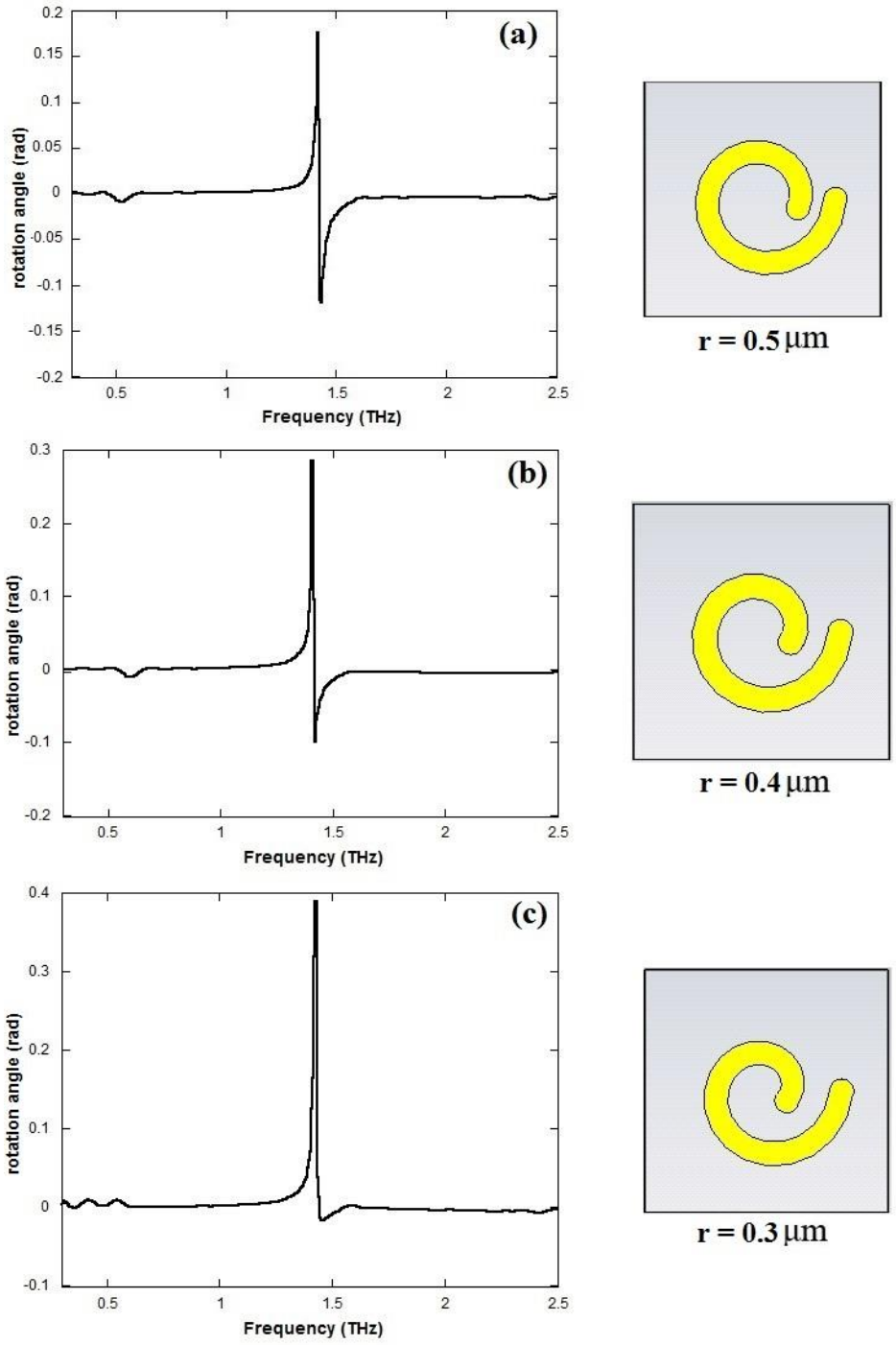

Fig 7.9: (a), (b) and (c) are respectively the rotation angle for the quasi-2D array of spirals with r = 0.5, 0.4 and 0.3. Schematics of the samples are shown on the right.

Figure 7.9 of the calculated rotation angle spectra for the quasi-2D array of spirals with different radius shows the same characteristic frequency dependence. The three samples have a strong resonance at ~ 1.4 THz which means that the frequency resonance and thus the polarisation of the transmitted THz radiation through our sample is independent of the radius of the spirals.

To examine the relationship between the optical activity and the length of the spirals in our 2D planar structure, we calculated the rotation angle spectra for three samples of n= 1.05, 1.15 and 1.25 corresponding to a spiral length of 37, 40 and 43 μm respectively, as shown in figure 7.10.

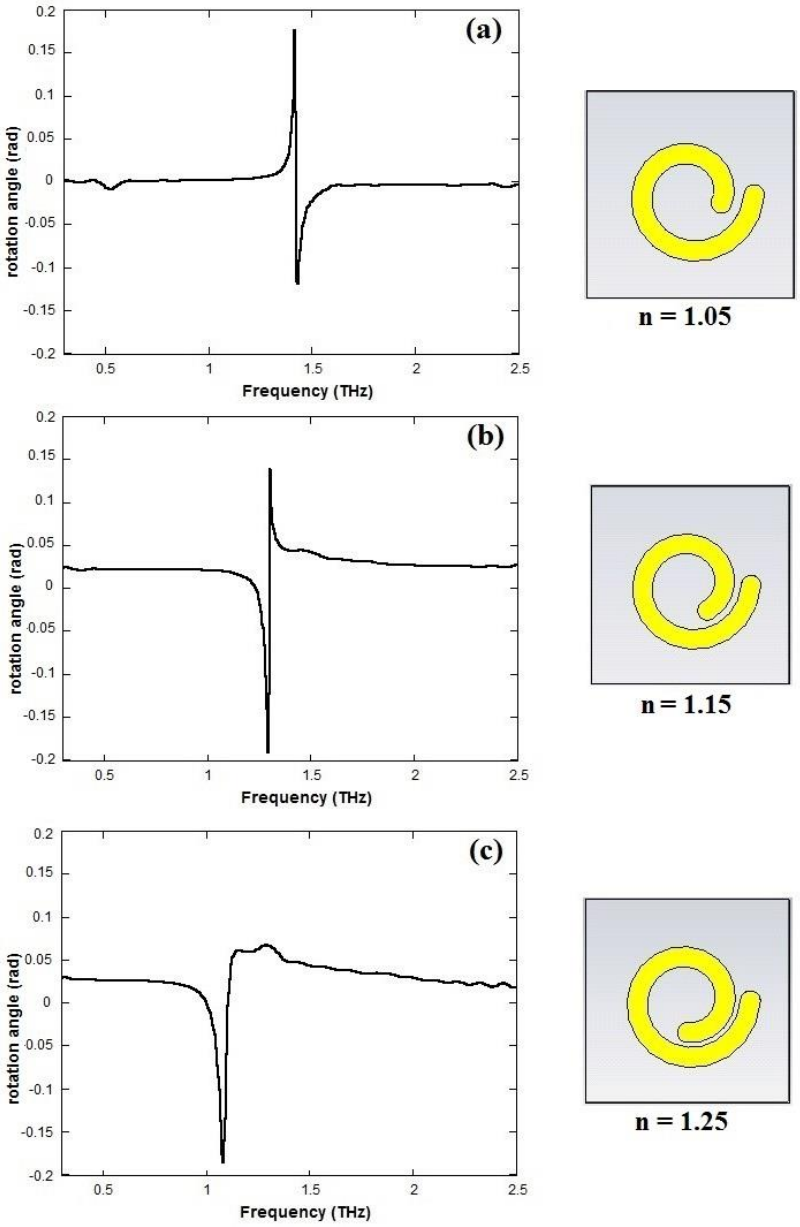

Fig 7.10: Dependence of the rotation angle on the length of the spirals. Schematics of the samples are shown on the right.

It is clear from figure 7.10 of the calculated rotation angle that the resonance frequency shifts with the variation in the length and increase with decreasing the length of the spiral. This means that the strong frequency observed in the rotation angle spectra depend also on the length of the spirals. In order to calculate the frequency resonance of the 2D array of spirals, we considered the length of the spiral as a dipole. The first resonant frequency is then given by

$$f_r = \frac{c}{2l\sigma}, \tag{3}$$

where σ is the electric conductivity of the silicon, c is the speed of light in vacuum and l is the length of the spiral. Equation (3) gives a resonance frequency of 1.3, 1.2 and 1.12 THz for 34, 40 and 43 μm length of the spiral respectively which is in a good agreement with the resonances found in the calculated rotation angle spectra in figure 7.10. From figure 7.8, 7.9 and 7.10 we can conclude that the origin of the resonant optical activity in our quasi-2D array of spirals is due to the width gap (the coupling between the spirals) and the length of the spirals.

7.3.2 Quasi-3D structure

To explore the optical activity of the three-dimensional array of spirals shown in figure (7.3), we performed similar experiments to those performed on the quasi-two-dimensional spiral array. Figure 7.11 shows the terahertz time domain waveforms for the 3D sample for both azimuthal positions 0° and 90°. The co-polarised and cross-polarised field components were detected using the two methods described in chapter 4.

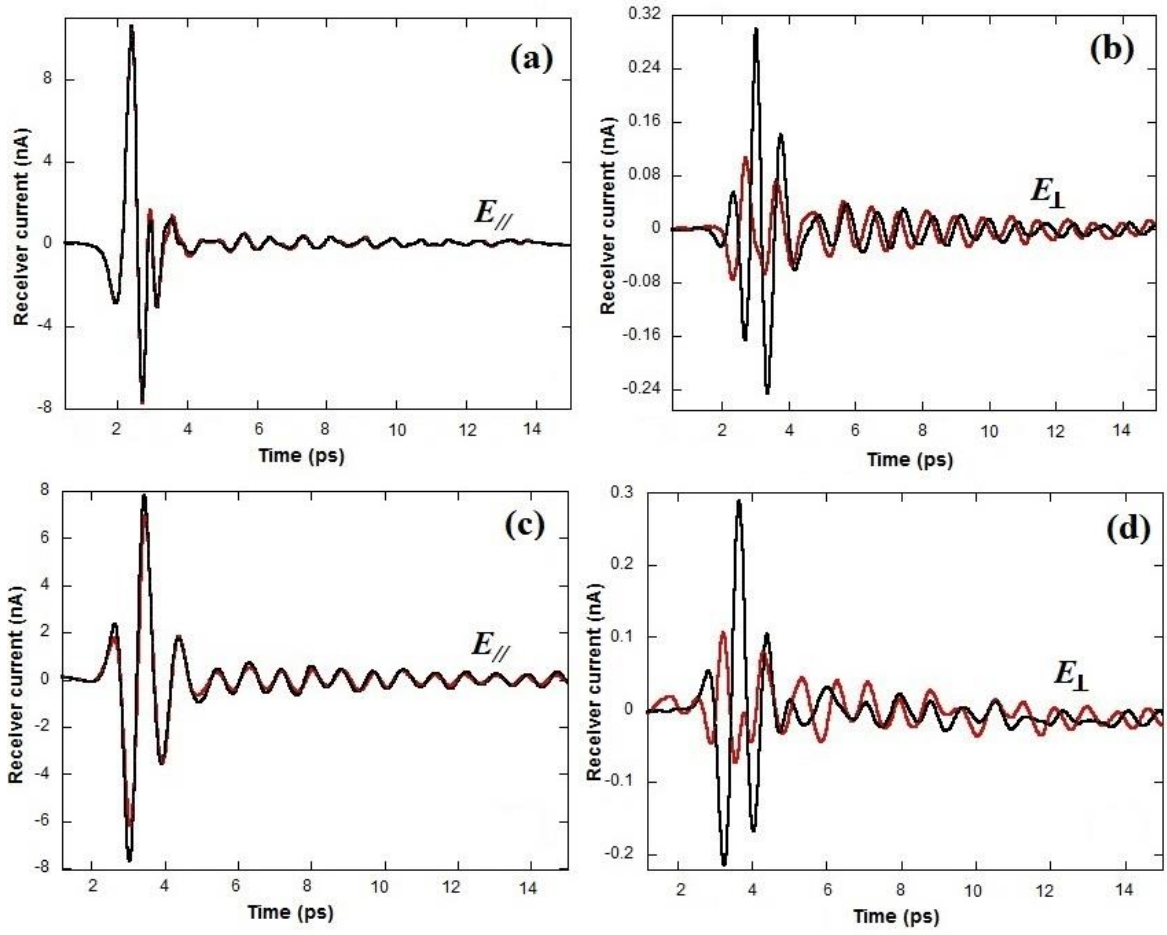

Fig 7.11: Time domain waveforms of the transmitted THz pulse through array of 3D spirals set at 0° (red) and at 90° (black): (a) and (b) are respectively the measured electric field component polarised parallel and perpendicular to the polarised radiation obtained using method 1. (c) and (d) are the measured electric field component polarised parallel and perpendicular to the polarised radiation respectively obtained using method 2.

The time domain traces in figure 7.11 (a) of the co-polarised transmitted electric field shows an overlap of the signals for the two azimuthal positions which is in a good agreement the same measurements performed using method 2 in figure 7.11 (c). We can notice from figure 7.11 (b) and (d) of the transmitted cross-polarised electric field when the sample is set at 0^{o} and 90^{o}, a difference in the magnitude of the signals an opposite sign in the beginning of the signals during 1 ps and then they overlapped. To validate the behaviour of the terahertz transmitted through our 3D array structure, we performed simulations using Microwave Studio. Figure 7.12 shows the time domain traces of the calculated co-polarised and cross-polarised electric field transmitted through the 3D material at azimuthal positions.

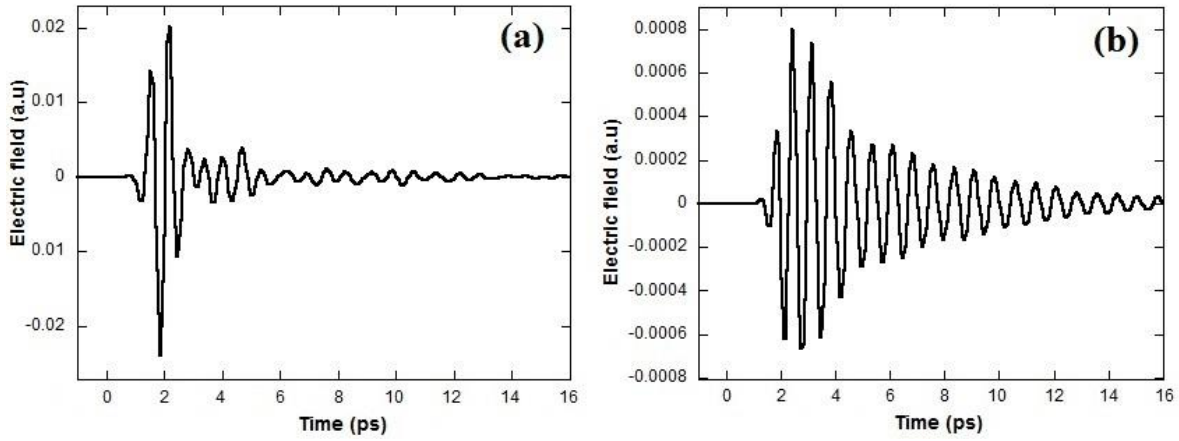

Fig 7.12: (a) and (b) are respectively the co-polarised and cross-polarised transmitted electric field through the 3D array of spirals for two azimuthal positions, 0° and 90°.

Figure 7.12 (a) of the calculated co-polarised transmitted electric field through the 3D sample, shows an overlap of the signals for both azimuthal positions which is in an agreement with the experiment in figures 7.11 (a) and (c). The cross-polarised transmitted fields in figure 7.12 (b) shows an overlap of the signal for the two azimuthal positions as expected and which is different from the experiment in figures 7.11 (b) and (d). These results show that the opposite sign in the measured cross-polarised transmitted field through the 3D sample might come from some defects of the fabrication or the size of the sample compared to the beam. The transmission matrix $T(t)$ in this case and considering the four-fold rotational symmetry can be defined as

$$T(t) = \begin{pmatrix} t_{xx} & t_{xy} \\ -t_{xy} & t_{xx} \end{pmatrix}, \tag{4}$$

this transmission matrix shows an opposite and an equal off-diagonal components respectively; $t_{xy} = -t_{yx}$ and $t_{xx} = t_{yy}$ which means that our 3D sample exhibits a circular birefringence. Figure 7.10 shows the circular dichroism and rotational angle spectra for left-hand and right-hand 3D array of spirals.

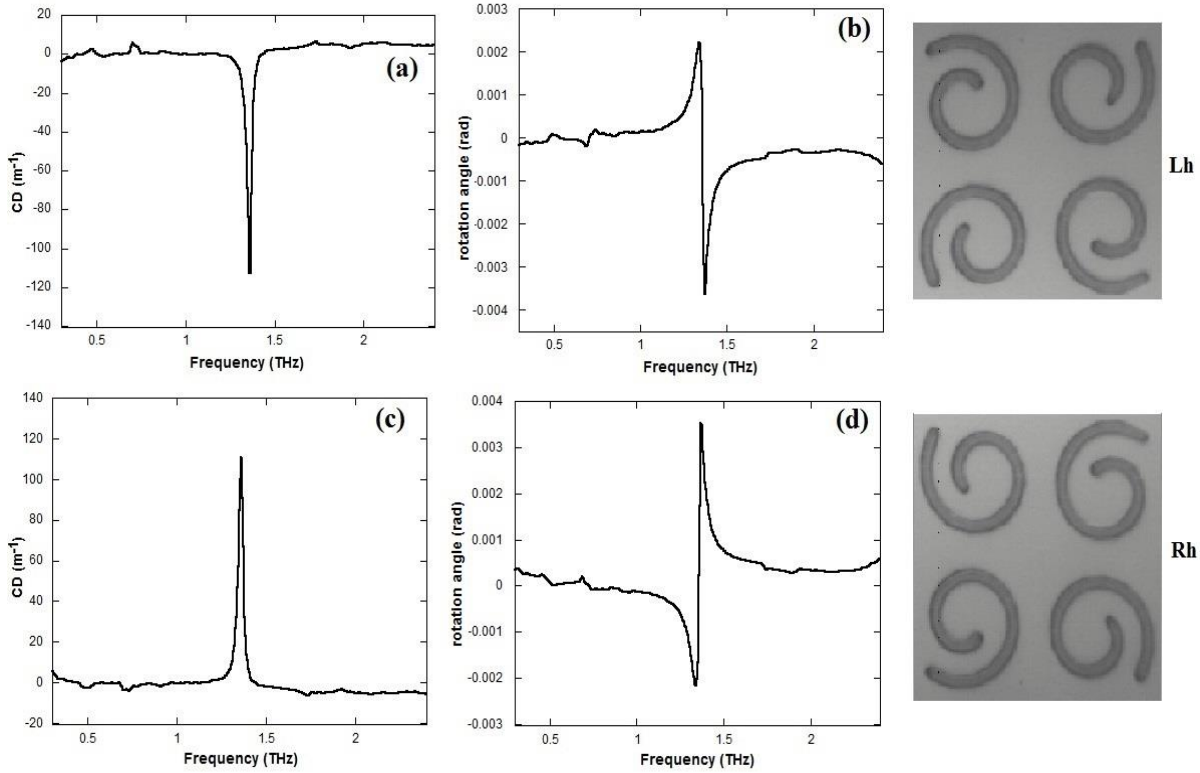

Fig 7.13: The calculated CD (left hand panels) and the rotation angle (right hand panels) spectra respectively for: (a) and (b) the left-hand 3D array of spirals, and (c) and (d) the right-hand 3D array of spirals. Microscope images of a unit cell showing the left and right hand rotation of the spirals.

As one can see from figures 7.13 (a) and (c) that the CD spectra show a strong resonance peak at frequency ~ 1.4 THz with a value of 120 m^{-1} for both left-hand and right-hand 3D structures which coincides with the strong resonance frequency found in the CD spectra of the quasi-2D array of spirals in figure 7.7 (c). The rotation angle in figures 7.13 (a) and (b) of the left and right hand 3D spirals shows the similar behaviour. These results show that the circular birefringence exhibited by our 3D array of spiral is due to the coupling between the spirals since the resonance frequency increase by decreasing the gap between the spirals as shown in figure 7.8, and the length of the spirals.

7.4 Conclusion

We have presented observations of optical activity including circular birefringence and dichroism in two different chiral metamaterials. The samples consist of a quasi-two-dimensional array of planar spirals and a quasi-three-dimensional array spirals both arranged on a high resistivity silicon substrate and have a four-fold rotational symmetry. We performed experimental and computational studies to characterise the optical activity associated with axial propagation in these two metamaterials. The results showed a strong modulation of the optical activity at a resonance frequency which is due to the width gap between the spirals and the length of the spirals.

References

1. Shelby R.A., Smith D.R., and Schultz S., *Experiment verification of negative index of refraction.* Science, 2001. **292**: p. 77-79.

2. Zhang S., Park Y.-S., Li J., Lu X., Zhang W., and Zhang X., *Negative Refractive Index in Chiral Metamaterials.* Physical Review Letters, 2009. **102**(2): p. 023901.

3. Gansel J.K., Thiel M., Rill M.S., Decker M., Bade K., Saile V., Von Freymann G., Lindlen S., and Wegener M., *Gold Helix Photonic Metamaterial as Broadband Circulat Polarizer.* Science, 2009. **325**: p. 1513-1515.

4. Plum E., Zhou J., Dong J., Fedotov V., Koschny T., Soukoulis C., and Zheludev N., *Metamaterial with negative index due to chirality.* Physical Review B, 2009. **79**(3): p. 035407.

5. Decker M., Klein M.W., Wegener M., and Linden S., *Circular dichroism of planar chiral magnetic metamaterials.* optics Letters, 2007. **32**(7): p. 856-858.

6. Mackay Tom G., and Lakhtakia A., *Negatively refracting chiral metamaterials.* SPIE Reviews, 2010. **1**: p. 018003.

7. Wang B., Zhou J., Koschny T., Kafesaki M., and Soukoulis Costas M., *Chiral metamaterials: simulations and experiments.* Journal of Optics A: Pure and Applied Optics, 2009. **11**: p. 114003.

8. Li M.-H., Yan H.-L, Tian Y., and Hou D.-Y., *Dual bands of negative refractive indexes in the planar left-handed metamaterials.* Journal of Magnetism and Magnetic Materials, 2011. **323**(5): p. 607-610.

9. Pendry J.B., Holden A.J., Robbins D.J., and Stewart W.J., *Magnetism from Conductors and Enhanced Nonlinear Phenomena.* IEEE transactions on microwave theory and techniques, 1999. **47**(11): p. 2075-2084.

10. Smith D.R., Padilla W.J., Vier D.C., Shelby D., Nemat-Nasser S.C., Kroll N., and Schultz S., *Left-Handed Metamaterials.* Phys. Rev. Lett., 2000. **84**: p. 1-21.

11. Bayindir M., Aydin K., Ozbay E., Markoš P., and Soukoulis C. M., *Transmission properties of composite metamaterials in free space.* Applied Physics Letters, 2002. **81**(1): p. 120.

12. Parazzoli C., Greegor R., Li K., Koltenbah B., and Tanielian M., *Experimental Verification and Simulation of Negative Index of Refraction Using Snell's Law.* Physical Review Letters, 2003. **90**(10): p. 107401.

13. Pendry J.B., *A Chiral Route to Negative Refraction.* Science, 2004. **306**: p. 1353-1355.

14. Tretyakov S., Nefedov N., Sihvola A., Maslovski S., and Simovski C., *Waves and Energy in Chiral Nihility.* J. Electromagn. Waves Appl., 2003. **17**: p. 695-706.

15. Monzon C., and Forester D., *Negative Refraction and Focusing of Circularly Polarized Waves in Optically Active Media.* Physical Review Letters, 2005. **95**(12): p. 123904.

16. Papakostas A., Potts A., Bagnall D., Prosvirnin S., Coles H., Zheludev N., *Optical Manifestations of Planar Chirality.* Physical Review Letters, 2003. **90**(10): p. 107404.

17. Vallius T., Jefimovs K., Turunen J., Vahimaa P., and Svirko Y., *Optical activity in subwavelength-period arrays of chiral metallic particles.* Applied Physics Letters, 2003. **83**(2): p. 234.

18. Kuwata-Gonokami M., Saito N., Ino Y., Kauranen M., Jefimovs K., Vallius T., Turunen J., and Svirko Y., *Giant Optical Activity in Quasi-Two-Dimensional Planar Nanostructures.* Physical Review Letters, 2005. **95**(22): p. 227401.

19. Bai B., Svirko Y., Turunen J., and Vallius T., *Optical activity in planar chiral metamaterials: Theoretical study.* Physical Review A, 2007. **76**(2): p. 023811.

20. Luk R. Arnaut, and Lionel E. Davis, *Dispersion Characteristics of Planar Chiral Structures.* Proceedings of the international conference on electromagnetics in advanced applications, 1995: p. 381.

21. Potts A., Papakostas A., Zheludev N.I., Coles H.J., Greef R., and Bagnall D.M., *Planar chiral meta-materials for photonic devices.* Materials Science: Materials in Electronics, 2003. **14**: p. 393-395.

22. Wang B., Zhou J., Koschny T., and Soukoulis Costas M., *Nonplanar Chiral Metamaterials with Negative Index.* Appl. Phys. Lett., 2009. **94**: p. 151112.

23. Wang B., Koschny T., and Soukoulis M. Costas, *Wide-angle and polarization-independent chiral metamaterial absorber.* Physical Review B, 2009. **80**: p. 033108.

24. Rogacheva A.V., Fedotov V.A., Schwanecke A. S., and Zheludev N. I., *Giant Gyrotropy due to Electromagnetic-Field Coupling in a Bilayered Chiral Structure.* Physical Review Letters, 2006. **97**(17): p. 177401.

25. Decker M., Ruther M., Kriegler C.E., Zhou J., Soukoulis C.M., Linden S., and Wegener M., *Strong optical activity from twisted-cross photonic metamaterials.* Optics Letters, 2009. **34**(16): p. 2501-2503.

26. Zhao R., Zhang L., Zhou J., Koschny Th., and Soukoulis C. M., *Conjugated gammadion chiral metamaterial with uniaxial optical activity and negative refractive index.* Physical Review B, 2011. **83**: p. 035105.

27. Li Z., Zhao R., Koschny T., Kafesaki M., Alici K.B., Colak E., Caglayan H., Ozbay E., and Soukoulis C. M., *Chiral metamaterials with negative refractive index based on four "U" split ring resonators.* Applied Physics Letters, 2010. **97**(8): p. 081901.

28. Xiong X., Sun W.-H., Bao Y.-J., Peng R.-W., Wang M., Sun C., Lu X., Shao J., Li Z.-F., and Ming N.-B., *Construction of Chiral Metamaterial with U-Shaped Resonator.* phys. rev. B, 2010. **81**(7): p. 075119.

29. Ordal M.A., Bell R.J., Alexander R.W. Jr, Long L.L., and Querry M.R., *Optical properties of fourteenmetals in the infrared and far infrared: Al, Co, Cu, Au, Fe, Pb, Mo, Ni, Pd, Pt, Ag, Ti, V, and W.* Applied Optics, 1985. **24**(24): p. 4493-4499.

30. He M., Han J., Tian Z., Gu J., and Xing Q., *Negative refractive index in chiral spiral metamaterials at terahertz frequencies.* Optik - International Journal for Light and Electron Optics, 2011. **122**(18): p. 1676-1679.

Chapter 8

Conclusions and suggestions for future work

In this thesis we have described the development of a polarisation resolved terahertz time domain spectrometer for the measurement of optical activity in transmission and its application to study several artificial chiral materials. The final instrument design is based on the use of a single linearly polarised photoconductive source and two photoconductive dipole receivers with dipole axes at right angles. The terahertz beam from the transmitter is linearly *p*-polarised to an estimated precision of better than 1 part in 10^{10} in intensity using a stack of ten silicon plates at Brewster's angle.

The beam transmitted by a sample is then divided into *s* and *p* polarised components using a high performance wire-grid beam splitter fabricated with the aid of nano-imprinting technique by the Japanese company Asahi Kasei E-Materials. The beam splitter has an intensity extinction of less than 10^{-4} below 2 THz when used as a polariser which is two orders of magnitude better than commercially available wire-grid polarisers. Chiral information is largely contained in the light scattered into *s*-polarisation by the sample. Using the nano-imprinted beam splitter the leakage of light from *p* into *s* polarisation is about 0.2 % in field in the absence of a sample. This is due to imperfections in the beam splitter, principally edge roughness of the metallisation and non-planarity. In future work it should be possible to replace the beam splitter, which is fabricated on a thin polymer substrate, by one made on silicon, polariser in the form of a double grating. In principle the technique might then be made background free, in which case the sensitivity to changes in polarisation would be similar to the noise limit of 1 part in 10^5 in field (0.001 %).

As part of the development process we also investigated using a single photoconductive device to measure both *s* and *p*-polarised field components simultaneously. This device consisted of a pair of crossed bow-tie antennas spanning a 50 µm square photoconductive gap. The terahertz induced photocurrents in the two arms were separately amplified and lock-in detected. Although this device proved very sensitive there was cross talk (of about 5 % in field) between orthogonal arms which we were unable to eliminate. It is thought that this is due to capacitive coupling.

Having developed a very competitive, sensitive instrument it was then applied to study three different chiral materials. The first of there was an array of M1 tapped holes in a 2mm thick aluminium plate as described in chapter 5. Strong resonant optical activity is observed and is similar to that predicted using computational modelling. The resonances appear to be only related to the screw pitch rather than also to Fabry-Perot cavity resonances as suggested in previous work.

In chapter 6 studies of planar gold gammadion arrays on Mylar substrates were described. There resonances in the circular dichroism and rotation angle are strongly influenced by capacitance coupling between adjacent elements. The weak optical activity in this example arises entirely from the asymmetry imposed by the presence of the substrate but is easily observed with the new instrument.

A second quasi-planar chiral metamaterial that was studied consisted of different varieties of Archimedean spirals arrays on silicon substrate. Arrays with and without rotational symmetry about the surface normal were investigated. Experimental and computational studies have shown that the strong resonance in the rotation angle and the circular dichroism are mainly influenced by the length of the spirals and the coupling between the adjacent elements.

The polarisation behaviours observed for these chiral metamaterials; gammadion and spirals, have shown that changes to design feature as the length and the gap between the adjacent elements, have a pronounced effect on the sense and magnitude of the polarisation response of the chiral metamaterial. It was also shown that planar geometry plays an important role in determining the optical activity of the planar chiral metamaterials. Additionally, the polarisation response of these chiral metamaterials was shown to be dependent on the thickness of the substrate in which the planar chiral were created. The gammadion structure with a substrate thickness of 36 μm a larger circular dichroism and rotation angle compared to the spirals structure with 650 μm. This is means that the polarisation changes are in a part, a consequence of multiple interference effects in the substrate. So the combination between this interference and the planar chiral structures results in a difference in the amplitudes and the phases for the electric field components polarised parallel and perpendicular to the incident radiation, and hence induced changes in ellipticity and a strong optical activity. This is believed to be a promising direction for further studies which are looking to understand the mechanisms produced by the polarisation response of planar chiral metamaterials.

One of the initial goals of this work was to try and develop an instrument capable of measuring optical activity in naturally occurring chiral media such as the classic liquid enantiomers of limonene and pharmaceutical products. Rough estimates suggest that a sensitivity of better than 1 part in 10^{10} in intensity would be required. As we have studied above, this might be achieved at terahertz frequencies but significant improvements in components such as the polarising beam splitter and in THz source power are required. Improvements in the source is a big challenge for the time domain technique and it seems likely that completely different approaches perhaps using quantum cascade lasers will be required to achieve the goal of measuring optical activity in pharmaceuticals or foodstuffs at terahertz frequencies.